UNIWERSYTET MARII CURIE-SKŁODOWSKIEJ
W LUBLINIE
Wydział Matematyki, Fizyki i Informatyki

Kierunek: **Fizyka**

Dariusz Wójcik
nr albumu: **984240**

JOANNA - dwupłynowy model numeryczny częściowo zjonizowanej atmosfery Słońca

JOANNA – two-fluid numerical model of a partially ionized solar atmosphere

Praca doktorska
napisana w Zakładzie Astrofizyki i Teorii Grawitacji
pod kierunkiem prof. dr hab. Krzysztofa Murawskiego

Lublin rok 2019

Chciałbym serdecznie podziękować mojej rodzinie oraz prof. dr hab. Krzysztofowi Murawskiemu za okazane wsparcie w trakcie powstawania tej pracy.

Spis treści

Rozdział 1

Wstęp

1.1 Motywacje i cel badań

Słońce, chociaż opisywane od wieków, wciąż jest słabo poznanym obiektem w naszym Układzie Słonecznym. Zachodząca we wnętrzu Słońca fuzja jądrowa wyzwala ogromne ilości energii, które są przekazywane do coraz bardziej odległych od jądra warstw. Intuicyjnym jest to, że wraz z oddalaniem się od źródła ciepła, temperatura spada. Inaczej jest w przypadku naszej gwiazdy, gdzie spadek temperatury obserwowany jest aż do atmosfery; z kilkunastu milionów Kelwinów w jądrze Słońca temperatura spada do 5000-6000 K w najniższych warstwach atmosfery [16]. Trochę wyżej w koronie temperatura gwałtownie rośnie i osiąga już kilka milionów Kelwinów [28, 2]. Zjawisko to zwane jest paradoksem ogrzewania korony słonecznej i pozostaje niewyjaśnione do dnia dzisiejszego.

Jako najbliższa Ziemi gwiazda, Słońce jest bardzo interesującym obiektem do badań. Znajduje się w centrum Układu Słonecznego i stanowi aż 99.86% jego masy. Jednakże z astronomicznego punktu widzenia jest ono powszechnym obiektem. Szacuje się, że w Naszej Galaktyce znajduje się ponad sto milionów podobnych do Słońca gwiazd. Fakt ten ma jednak pozytywny wydźwięk. To czego dowiadujemy się z badań Słońca, można łatwo ekstrapolować na ogromną liczbę gwiazd podobnych do Słońca. Poznanie procesów rządzących Słońcem jest zatem kluczem do zrozumienia otaczającego nas wszechświata.

Słońce składa się głównie z wodoru (73%), helu (25%), tlenu (0.77%) oraz z małej ilości innych cięższych pierwiastków takich jak węgiel, żelazo, azot, krzem, magnez czy siarka [16]. Zostało ono sklasyfikowane jako typ spektralny G2V, gdzie G2 oznacza iż temperatura efektywna jest równa 5778 K, natomiast V oznacza przynależność Słońca do ciągu głównego gwiazd oraz to, że generuje ono energię w wyniku fuzji [28].

Motywacją do badań był brak pełnej odpowiedzi na pytanie dotyczące ogrzewania korony słonecznej. Dotychczas przeprowadzane symulacje numeryczne opierały się w zasadzie na modelach hydrodynamicznych (HD) i magnetohydrodynamicznych (MHD), które są modelami jednopłynowymi. Z przeprowadzonych dotychczas symulacji i obserwacji płynie wniosek sugerujący konieczność uwzględnienia częściowej jonizacji plazmy w atmosferze Słońca. Symulacje przy użyciu kodu, w którym cząstki zjonizowane oraz neutralne są mobilne, dałyby informację o tym, czy energia wytwarzana cieplna podczas zderzenia pomiędzy cząstkami neutralnymi i zjonizowanymi jest wystarczające, aby ogrzać chłodne części atmosfery. Aby odpowiedzieć na to pytanie potrzebnym było opracowanie dwupłynowego kodu numerycznego JOANNA, który w sposób jawny traktowałby dynamikę zjonizowanej i neutralnej części plazmy. Dodatkowym celem badań było pokazanie wpływu granulacji na generację wiatru słonecznego - drugiego centralnego problemu fizyki Słońca.

Na treść niniejszej pracy składają się badania przeprowadzone za pomocą kodu numerycznego JOANNA, w których przedstawiam wyniki pokazujące potencjał rozwoju badań prowadzonych w modelu dwupłynowym. Uzyskane wyniki pokazują, że modelowanie za pomocą kodu dwupłynowego daje dobre rezultaty, które pokrywają się z danymi obserwacyjnymi.

1.2 Organizacja pracy

Praca została zorganizowana następująco: w rozdziale 1 znajduje się krótki wstęp opisujący ideę przeprowadzonych badań. Rozdział 2 zawiera opis równań użytych w opracowanym kodzie JOANNA. Rozdział 3 przedstawia opracowany numeryczny model atmosfery Słońca. W rozdziale 4 przedstawione zostały uzyskane wyniki numeryczne i wnioski z nich płynące. Rozdział 5 zawiera podsumowanie badań zawartych w tej pracy. Rozdział 6 zawiera spis opublikowanych artykułów, które dołączono w części końcowej.

Rozdział 2

Modele płynowe i ich ograniczenia

Gazy składają się z dużej liczby molekuł. Ruch każdej z nich może być śledzony indywidualnie. Taki opis nazywa się opisem cząstkowym i prowadzi on do dużej liczby zwyczajnych równań różniczkowych stanowiących drugą zasadę dynamiki Newtona

$$m_i \frac{d\overrightarrow{V}_i}{dt} = \overrightarrow{F}_i, \tag{2.1}$$

i definicję prędkości

$$\frac{d\overrightarrow{r}_i}{dt} = \overrightarrow{V}_i. \tag{2.2}$$

Powstały układ równań jest zbyt liczny, aby możliwym było znaleźć rozwiązania metodami komputerowymi. Aby poradzić sobie z taką ilością równań można skorzystać z modelu kinetycznego, w którym gaz opisuje się statystycznie za pomocą równania Boltzmana i z równań Maxwella, aby uzupełnić model o oddziaływania z polem magnetycznym i elektrycznym. Niestety model jest również zbyt skomplikowany numerycznie, aby nadawał się do praktycznych obliczeń. Zamiast opisu cząstkowego i kinetycznego stosowany jest więc opis makroskopowy. W modelu tym szczególnego znaczenia nabierają wielkości makroskopowe takie jak: gęstość masy ϱ, prędkość plazmy $\mathbf{V}$ i ciśnienie p. Wszystkie te wielkości mogą być mierzone doświadczalnie.

W modelu jednopłynowym atmosfera Słońca rozpatrywana jest za pomocą MHD. Model ten zakłada kwazineutralność ładunkową plazmy. Równania MHD stanowią połączenie równań Eulera i równań Maxwella przy założeniu, że plazma jest potraktowana jako jednolity płyn, efekty relatywistyczne są zaniedbane, większość właściwości plazmy przyjętych jest za izotropowe, prąd przesunięcia i przemieszczenia między jonami i elektronami jest zaniedbany, a cząstki posiadają jedną wspólną masę. Interesują nas również zjawiska zachodzące na dużych skalach czasowych. Model ten ma tę zaletę, że wszelkie efekty liniowe mogą zostać łatwo porównane z analitycznymi rozważaniami. O ile możliwe jest uwzględnienie obecności neutralnych

cząstek za pomocą członów takich jak dyfuzja ambipolarna [np. 9], to nadal nie daje to pełnej informacji o ewolucji neutralnych cząstek w atmosferze.

Rozwinięciem modelu jednopłynowego jest model wielopłynowy plazmy, w którym uwzględniona zostaje dynamika nie tylko jonów, ale także cząstek neutralnych i elektronów. Taki model wierniej oddaje fizykę plazmy słonecznej ze względu na efekt częściowej jonizacji [11, 2]. Model ten ma też wadę - ze względu na elektrony i powstawanie fal elektromagnetycznych (EM), pojawiają się bardzo duże ograniczenia na krok czasowy całkowania numerycznego (rzędu 10^{-9} sekundy), co powoduje, że obliczenia stają się powolne, a przez to niepraktyczne. Rozwiązaniem tego problemu jest wykorzystanie modelu dwupłynowego, gdzie występują dynamiczne cząstki neutrale i jony. Elektrony w tym modelu traktowane są jako związane z jonami. Pozwala to na znaczne przyspieszenie obliczeń numerycznych jednocześnie zachowując efekty związane z elektronami. Modele dwupłynowe, znane też jako modele jonowo-neutralne są rozwinięciem obecnie prowadzonych badań atmosfery Słońca przy użyciu MHD.

Przy badaniach opartych o model dwupłynowy ważnym jest, aby uwzględnić zderzenia pomiędzy różnymi składnikami plazmy, takimi jak jony (i), elektrony (e), czy neutralne atomy (n). Jeżeli częstość zderzeń ν_{kl} pomiędzy składnikiem k i l jest znacznie większa niż częstość badanego zjawiska, całość może być traktowana jako jeden płyn. Jednakże w wielu przypadkach, takich jak na przykład niskie warstwy atmosfery słonecznej [2], $\nu \ll \nu_{ie}$ podczas, gdy $\nu > \nu_{in}$. W takim wypadku model dwupłynowy jest sumą dwóch zestawów równań. Jeden z nich to płyn złożony z jonów i elektronów opisany równaniami MHD, podczas gdy drugi to płyn neutralny opisywany równaniami hydrodynamiki. Te dwa zestawy równań są ze sobą sprzęgnięte za pomocą członów źródłowych opisujących oddziaływanie ich ze sobą. Zanim jednak przedstawię ten model, należy wcześniej zacząć od modelu kinetycznego plazmy.

2.1 Model kinetyczny plazmy

W fizyce przestrzeni kosmicznej istnieją przypadki, w których średnia droga swobodna cząsteczek (zdefiniowana jako średnia odległość jaką przebywa cząsteczka między zderzeniami) jest porównywalna lub większa niż lokalna skala przestrzenna. W tych przypadkach plazma jest tak rozrzedzona, że równania Eulera nie stanowią już dobrego opisu i teoria kinetyczna jest niezbędna. Rozważmy plazmę, której i-składnik posiada ładunek elektryczny e_i, masę m_i, gęstość liczbową n_i, prędkość $\mathbf{v}_\mathrm{i}$ i temperaturę T_i. Procesy kinetyczne charakteryzują się skalami

czasowymi, które są związane z częstością plazmową,

$$\omega_{\mathrm{i}} = \sqrt{\frac{n_{\mathrm{i}} e_{\mathrm{i}}^2}{\varepsilon m_{\mathrm{i}}}}\,, \tag{2.3}$$

i częstością cyklotronową,

$$\Omega_{\mathrm{i}} = \frac{|e_{\mathrm{i}}| B}{m_{\mathrm{i}}}\,, \tag{2.4}$$

gdzie B jest wartością indukcji pola magnetycznego, a ϵ jest przenikalnością dielektryczną ośrodka. W celu uproszczenia indukcję pola magnetycznego będziemy nazywać polem magnetycznym. Skala długości określona jest tymi częstościami i odpowiednimi prędkościami. Skale te to:

a) długość Debye'a

$$\lambda_{Di} = \sqrt{\frac{\varepsilon k_{\mathrm{B}} T}{n_{\mathrm{i}} e_{\mathrm{i}}^2}} \tag{2.5}$$

z prędkością dźwięku

$$c_{\mathrm{i}} = \sqrt{\frac{k_{\mathrm{B}} T_{\mathrm{i}}}{m_{\mathrm{i}}}}\,. \tag{2.6}$$

Tutaj k_{B} jest stałą Boltzmanna;

b) termiczny promień żyroskopowy

$$r_{\mathrm{ti}} = \frac{c_{\mathrm{i}}}{\Omega_{\mathrm{i}}}\,; \tag{2.7}$$

c) promień żyroskopowy

$$r_{di} = \frac{v_{\mathrm{i}}}{\Omega_{\mathrm{i}}}\,; \tag{2.8}$$

d) długość inercyjna

$$\lambda_{\mathrm{i}} = \frac{c}{\omega_{\mathrm{i}}}\,. \tag{2.9}$$

Kinetyczny (płynowy) opis plazmy jest wymagany wtedy, kiedy powyższe skale są porównywalne lub większe (mniejsze od) skal zjawiska fizycznego. Istnieje też reżim pośredni np. kiedy efekty kinetyczne są istotne wzdłuż równowagowego pola magnetycznego, a są one do zaniedbania w kierunku prostopadłym. W innym przypadku różne składniki plazmy mogą być traktowane w różny sposób. W opisie hybrydowym jedne składniki są opisane równaniami kinetycznymi, a inne potraktowane są jak płyn.

Stan gazowy może być opisany z wykorzystaniem funkcji dystrybucji dla różnych składników. Dla odpowiednio rozrzedzonych gazów jedna funkcja dystrybucji $f(\mathbf{v}, \mathbf{r}, t)$ jest zwykle wystarczająca przy założeniu, że nie ma korelacji między dwiema cząstkami. Funkcja dystrybucji jest zdefiniowana jako wielkość $f(\mathbf{v}, \mathbf{r}, t) d\mathbf{v}\, d\mathbf{r}$, która równa jest ilości cząsteczek o prędkości zawartej w przedziale $< \mathbf{v}, \mathbf{v} + d\mathbf{v} >$ i znajdujących się w przestrzeni $< \mathbf{r}, \mathbf{r} + d\mathbf{r} >$ w czasie t. Dystrybucja ta zależy od siedmiu argumentów: trzech składowych prędkości, trzech składowych

wektora położenia $\mathbf{r}$ i czasu t. Zredukowanie tej liczby argumentów jest zwykle wymagane, aby uczynić problem możliwym do rozważania. Redukcję osiąga się poprzez wyrażenie dystrybucji za pomocą momentów.

Pierwszym momentem jest gęstość liczbowa

$$n(\mathbf{r},t) = \int f(\mathbf{v},\mathbf{r},t)d\mathbf{v}\,. \tag{2.10}$$

Stąd gęstość masy ϱ określona jest

$$\varrho(\mathbf{r},t) = m\,n(\mathbf{r},t)\,, \tag{2.11}$$

gdzie m jest masą cząstki. Mikroskopowy opis odnosi się do $f(\mathbf{v},\mathbf{r},t)$, podczas gdy w opisie makroskopowym używamy $\varrho(\mathbf{r},t)$.

Przy założeniu, że zderzenia między cząsteczkami są zaniedbywalne zjawiska kinetyczne opisane są równaniem Własowa [24]

$$f_{\mathrm{i},t} + \mathbf{v}\cdot\nabla f_{\mathrm{i}} + \frac{e_{\mathrm{i}}}{m_{\mathrm{i}}}[\mathbf{E} + (\mathbf{v}\times\mathbf{B})]\cdot f_{\mathrm{i},\mathbf{v}} = 0\,, \tag{2.12}$$

gdzie $f_{\mathrm{i}}(\mathbf{r},\mathbf{v})$ oznacza funkcję dystrybucji i-tego składnika plazmy. Pole elektryczne $\mathbf{E}$ i magnetyczne $\mathbf{B}$ opisane są równaniami Maxwella, które zawierają człony źródłowe powstałe z momentów wszystkich składników plazmy, *tj.*

$$\nabla\times\mathbf{E} = -\mathbf{B}_{,t}\,, \tag{2.13}$$

$$\frac{1}{\mu}\nabla\times\mathbf{B} = \sum_i e_{\mathrm{i}}\int f_{\mathrm{i}}\mathbf{v}d\mathbf{v} + \varepsilon\mathbf{E}_{,t}\,, \tag{2.14}$$

$$\nabla\cdot\mathbf{B} = 0\,, \tag{2.15}$$

$$\varepsilon\nabla\cdot\mathbf{E} = \sum_i e_{\mathrm{i}}\int f_{\mathrm{i}}d\mathbf{v}\,. \tag{2.16}$$

Aby ocenić znaczenie równań (2.13)-(2.15) należy zadecydować, który rodzaj pola elektromagnetycznego dominuje. Dla silnego pola magnetycznego możemy zaniedbać zaburzenia w polu magnetycznym w całym zakresie częstości. W tym przypadku fluktuacje gęstości ładunku elektrycznego są ważne a pole elektrostatyczne ewoluuje zgodnie z równaniem (2.16). Zarówno jony jak i elektrony są często traktowane w tym przypadku kinetycznie z odpowiednimi skalami przestrzennymi i czasowymi, równymi odpowiednio elektronowej długości Debye'a i odwrotności elektronowej częstości plazmowej. Dla częstości mniejszych niż jonowa częstość plazmowa elektrony są traktowane adiabatycznie z gęstością cząsteczkową,

$$n_e = n_{e_0}\exp\left(-\frac{|e|\phi}{k_B T_e}\right)\,. \tag{2.17}$$

Tutaj ϕ jest potencjałem elektrostatycznym takim, że

$$\mathbf{E} = -\nabla\phi \tag{2.18}$$

i n_{e0} jest równowagową gęstością elektronów. Zaburzenia, które spełniają ten warunek, nazywane są *elektrostatycznymi*. Dla skończonych wartości pola magnetycznego istnieje wiele obszarów, które możemy sklasyfikować w zależności od częstości fali w porównaniu z cyklotronową częstością elektronu Ω_e. Dla częstości o wiele większych niż Ω_e zarówno elektrostatyczne i elektromagnetyczne oscylacje są istotne w plazmie. Oscylacje te są zwykle słabo sprzężone. Do opisu elektrostatycznych oscylacji możemy zastosować przybliżenie elektrostatyczne, Jeśli interesują nas fale elektromagnetyczne, równania Maxwella muszą być rozwiązane.

Dla częstości bliskich Ω_e, dynamika elektronów musi być także uwzględniona. Jednakże dla odpowiednich skal czasowych, jony muszą być potraktowane jako niemobilny płyn. Dla $\Omega_{io} < \omega < \Omega_e$, zarówno dynamika elektronów jak i jonów oraz fale elektromagnetyczne muszą być uwzględnione. Tutaj Ω_{io} jest cyklotronową częstością jonu. W przypadku gdy $\omega < \Omega_{io}$, elektrony mogą być potraktowane jako bezmasowy płyn. Wtedy do określenia pola elektrycznego zamiast równania (2.16) zastosujemy równanie zachowania pędu elektronu.

2.2 Przybliżenie kwazicząstkowe

Równania (2.13)-(2.15) sprawiają duży kłopot przy próbie ich analitycznego rozwiązania i dlatego zwykle niezbędne jest ich numeryczne rozwiązanie, w którym f_{i} przybliżamy pewną liczbą kwazicząstek.

Kolektywne zachowanie płynu możemy otrzymać poprzez uśrednienie po kwazicząstkach, których liczba N jest zawsze mniejsza niż rzeczywista liczba cząstek w układzie. Położenie kwazicząstek możemy znaleźć w wyniku rozwiązania równań trajektorii, tj.

$$\frac{d\mathbf{r}_{\mathrm{i}}}{dt} = \mathbf{V}_{\mathrm{i}}(t), \quad i = 1, 2, \cdots, N\,. \tag{2.19}$$

Tutaj $\mathbf{V}_{\mathrm{i}}$ oznacza prędkość kwazicząstki o numerze i. Prędkość tą możemy określić z drugiej zasady dynamiki Newtona,

$$m_{\mathrm{i}}\frac{d\mathbf{V}_{\mathrm{i}}}{dt} = \mathbf{F}_{\mathrm{i}}(\{\mathbf{r}_l\}, \{\mathbf{V}_l\}, t), \quad l = 1, 2, \cdots, N, \;\; l \neq i\,, \tag{2.20}$$

gdzie siła $\mathbf{F}_{\mathrm{i}}$ działająca na i-tą kwazicząstkę zależy od położeń $\{\mathbf{r}_l\}$ i prędkości $\{\mathbf{V}_l\}$ pozostałych cząstek.

Gęstość masy ϱ możemy znaleźć w wyniku uśrednienia, na ogół przy użyciu funkcji wagowej uwzględniającej skończone rozmiary cząstek, tj.

$$\varrho(\mathbf{r}_\mathrm{i}) =< \sum_j m_j \delta(\mathbf{r}_j - \mathbf{r}_\mathrm{i}) > \ . \tag{2.21}$$

Tutaj dokonujemy sumowania po masach m_j wszystkich cząstek j, które znajdują się w pobliżu i-tej cząstki. Podobnie gęstość pędu $\varrho\mathbf{v}$ określić można w wyniku zsumowania pędów cząstek, tj.

$$\varrho\mathbf{V}(\mathbf{r}_\mathrm{i}) =< \sum_j m_j \mathbf{V}_j \delta(\mathbf{r}_j - \mathbf{r}_\mathrm{i}) > \ . \tag{2.22}$$

Przybliżenia kwazicząstkowego możemy używać do numerycznego rozwiązania równań. Jednakże przybliżenie to sprawia kłopoty jeśli chodzi o płyny nieściśliwe, dla których warunek $\nabla \cdot \mathbf{V} = 0$ jest trudnym do spełnienia. Kwazicząstki nie mogą przenikać przez siebie. Czasem błędy numeryczne związane ze skończonym krokiem czasowym mogą doprowadzić do niefizycznego przenikania cząstek. Metody numeryczne są zwykle stabilne i spełniają warunki dodatniości gęstości masy i ciśnienia oraz spełniają prawa zachowania. W konsekwencji ograniczonej mocy komputerów i skończonej liczby kwazicząstek, metody numeryczne mogą być mało dokładne i mało efektywne.

2.3 Przybliżenie magnetohydrodynamiczne

Wyprowadzenie równań opisujących dynamikę plazmy rozpoczyna się od równania Boltzmanna, które opisuje zachowanie cząstek plazmy. Obliczając momenty tego równania ze względu na prędkość, ładunek elektryczny itd. możemy otrzymać różne równania dla cząstek płynu takie jak pęd i gęstość ładunku elektrycznego, do których należy dołączyć równania Maxwella.

Równanie pędu zawiera wtedy dodatkowy człon, który pochodzi z siły Lorentza $\mathbf{j} \times \mathbf{B}$, *tj.*

$$(\varrho\mathbf{v})_{,t} + \nabla \cdot ((\varrho\mathbf{v})\,\mathbf{v}) = -\nabla p + \mathbf{j} \times \frac{\mathbf{B}}{\mu}\,, \tag{2.23}$$

gdzie $\mathbf{j} = \nabla \times \frac{\mathbf{B}}{\mu}$ z μ będącym przenikalnością magnetyczną. Pole magnetyczne zmienia równanie energii, które możemy zapisać jako [16]

$$E_{,t} + \nabla \cdot \left((E + p + \frac{\mathbf{B}^2}{2\mu})\mathbf{v} - \frac{1}{\mu}\mathbf{B}(\mathbf{v} \cdot \mathbf{B}) \right) = 0\,, \tag{2.24}$$

gdzie gęstość energii całkowitej E jest

$$E = \frac{p}{\gamma - 1} + \frac{\varrho v^2}{2} + \frac{B^2}{2\mu}\,. \tag{2.25}$$

Trzy człony opisują odpowiednio gęstość energii wewnętrznej, kinetycznej i magnetycznej.

W podsumowaniu, równania idealnej magnetohydrodynamiki (MHD) stanowi następujący układ:

$$\frac{\partial \varrho}{\partial t} + \nabla \cdot (\varrho \mathbf{V}) = 0\,, \tag{2.26}$$

$$\varrho \frac{\partial \mathbf{V}}{\partial t} + \varrho\,(\mathbf{V} \cdot \nabla)\,\mathbf{V} = -\nabla p + \frac{1}{\mu}(\nabla \times \mathbf{B}) \times \mathbf{B} + \varrho \mathbf{g}\,, \tag{2.27}$$

$$\frac{\partial \mathbf{B}}{\partial t} = \nabla \times (\mathbf{V} \times \mathbf{B})\,, \tag{2.28}$$

$$\nabla \cdot \mathbf{B} = 0\,, \tag{2.29}$$

$$\frac{\partial p}{\partial t} + \nabla \cdot (p\mathbf{V}) = (1-\gamma) p \nabla \cdot \mathbf{V}\,, \tag{2.30}$$

$$p = \frac{k_{\mathrm{B}}}{m} \varrho T\,. \tag{2.31}$$

Tutaj ϱ jest gęstością masy, $\mathbf{V} = [u, v, w]$ jest prędkością, $\mathbf{B}$ oznacza indukcję pola magnetycznego, p jest ciśnieniem, γ jest indeksem adiabatycznym (współczynnikiem adiabaty), oznaczającym iloraz ciepeł właściwych, $\mathbf{g}$ oznacza wektor przyspieszenia grawitacyjnego, T jest temperaturą, m jest masą główną cząstki, a k_{B} oznacza stałą Boltzmanna.

2.4 Równania dwupłynowe

Kompletny zestaw równań opisujących plazmę częściowo zjonizowaną i używaną w kodzie JOANNA został opisany przez wielu autorów [8, 14, 2]. Płyn złożony z neutralnych atomów opisywany jest za pomocą następującego zestawu równań

$$\frac{\partial \varrho_n}{\partial t} + \nabla \cdot (\varrho_n \mathbf{V}_n) = 0\,, \tag{2.32}$$

$$\frac{\partial (\varrho_n \mathbf{V}_n)}{\partial t} + \nabla \cdot (\varrho_n \mathbf{V}_n \otimes \mathbf{V}_n + p_n \mathbf{I}) = \varrho_n \mathbf{g}\,, \tag{2.33}$$

$$\frac{\partial E_n}{\partial t} + \nabla \cdot [(E_n + p_n)\mathbf{V}_n] = \varrho_n \mathbf{V}_n \cdot \mathbf{g}\,, \tag{2.34}$$

$$E_n = \frac{p_n}{\gamma - 1} + \frac{\varrho_n \mathbf{V}_n^2}{2}, \tag{2.35}$$

gdzie $\mathbf{I}$, ϱ_n, $\mathbf{V_n}$, p_n, E_n jest odpowiednio tensorem jednostkowym, gęstością masy, prędkością, ciśnieniem i energią cząstek neutralnych, γ jest wykładnikiem adiabaty, a $\mathbf{g}$ jest wektorem przyspieszenia grawitacyjnego.

Płyn zjonizowany opisywany jest za pomocą równań GLM-MHD

$$\frac{\partial \varrho_i}{\partial t} + \nabla \cdot (\varrho_i \mathbf{V}_i) = 0\,, \tag{2.36}$$

$$\frac{\partial (\varrho_i \mathbf{V}_i)}{\partial t} + \nabla \cdot (\varrho_i \mathbf{V}_i \otimes \mathbf{V}_i + p_i \mathbf{I}) + \mathbf{J} \times \mathbf{B} = \varrho_i \mathbf{g}\,, \tag{2.37}$$

$$\frac{\partial E_i}{\partial t} + \nabla \cdot \left[\left(E_i + p_i + \frac{\mathbf{B}^2}{2} \right) \mathbf{V}_i - \mathbf{B}(\mathbf{V} \cdot \mathbf{B}) \right] = \varrho_i \mathbf{V}_i \cdot \mathbf{g}\,, \tag{2.38}$$

$$\frac{\partial \mathbf{B}}{\partial t} - \nabla \times (\mathbf{V_i} \times \mathbf{B}) + \nabla \cdot \psi \mathbf{I} = 0\,, \tag{2.39}$$

$$\frac{\partial \psi}{\partial t} + c_h^2 \nabla \cdot \mathbf{B} = -\frac{c_h^2}{c_p^2} \psi\,, \tag{2.40}$$

$$E_i = \frac{p_{ie}}{\gamma - 1} + \frac{\varrho_i \mathbf{V}_i^2}{2} + \frac{\mathbf{B}^2}{2}. \tag{2.41}$$

Tutaj ϱ_i, $\mathbf{V_i}$, E_i, jest gęstością masy, prędkością oraz energią zjonizowanych cząstek, p_{ie} jest sumą ciśnień jonów i elektronów, $\mathbf{B}$ jest wektorem pola magnetycznego a $\mathbf{J} = \nabla \times \mathbf{B}$ jest prądem. Wielkości c_h jest maksymalna prędkością hiperboliczną, c_p parabolicznym współczynnikiem dyfuzji dla równania czyszczącego dywergencję pola magnetycznego, a ψ jest dodatkową funkcją w metodzie GLM [3]. W pojawiających równaniach B zostało zamienione przez $\mathbf{B}/\mu$, w rezultacie czego przenikalność magnetyczna μ nie występuje jawnie.

Człony źródłowe opisujące interakcje pomiędzy tymi płynami opisują rekombinację i jonizację, wymianę pędu oraz energii. Do tej pory rekombinacja i jonizacja nie była używana w badaniach, dlatego człony źródłowe zaprezentowane w tej pracy ich nie zawierają.

Oddziaływanie pomiędzy płynami

Zgodnie z obliczeniami przeprowadzonymi przez [4] i [8] należy zacząć od obliczenia członu źródłowego odpowiedzialnego za wymianę pędu pomiędzy płynami. Podobnie jak w przypadku równań wyprowadzonych przez [14] zauważyć można, że parametr s w notacji [4] w przypadku atmosfery słonecznej jest bliski zeru 0, a więc funkcje $I_1(s)$, $I_2(s)$ i $I_3(s)$ [4], gdy $s \to 0$, są równe $I_1(s) = \frac{8}{3}$, $I_2(s) = 4$ oraz $I_3(s) = 0$. To przybliżenie upraszcza skomplikowane wyrażenia w modelu dwupłynowym. Posługując się notacją [8] transfer pędu zapisać można jako

$$\mathbf{R}_\alpha^{\alpha\beta} = \nu_{\alpha\beta} m_\alpha n_\alpha (\mathbf{V}_\beta - \mathbf{V}_\alpha). \tag{2.42}$$

Człon odpowiedzialny za wymianę energii w wyniku zderzeń elastycznych cząstek α i β wygląda następująco [8]

$$Q_\alpha^{\alpha\beta} = \frac{1}{2} \mathbf{R}_\alpha^{\alpha\beta} (\mathbf{V}_\beta - \mathbf{V}_\alpha) + G_\alpha^{\alpha\beta}, \tag{2.43}$$

gdzie $G_\alpha^{\alpha\beta}$ jest członem związanym z rozpraszaniem elastycznym (równanie 3.13) [4]

$$G_\alpha^{\alpha\beta} = \frac{3k_B}{m_\alpha + m_\beta} a_{\alpha\beta}(T_\beta - T_\alpha). \tag{2.44}$$

Tutaj $a_{\alpha\beta} = \nu_{\alpha\beta}\varrho_\alpha$ jest współczynnikiem tarcia pomiędzy cząstkami α i β, a m_α jest masą cząstek α. Częstość zderzeń jest zdefiniowana jako [2]

$$\nu_{\alpha\beta} = \frac{4}{3}\frac{n_\beta m_\beta}{m_\alpha + m_\beta}\sqrt{\frac{8k_B}{\pi m_H}\left(\frac{T_\beta}{\mu_\alpha} + \frac{T_\beta}{\mu_\beta}\right)}\sigma_{\alpha\beta}. \tag{2.45}$$

Wartym zauważenia jest fakt, że $a_{\alpha\beta} = a_{\beta\alpha}$, podczas gdy $\nu_{\alpha\beta} \neq \nu_{\beta\alpha}$.

Sumarycznie, równania dwupłynowe można zapisać jako

$$\frac{\partial \varrho_n}{\partial t} + \nabla \cdot (\varrho_n \mathbf{V}_n) = 0\,, \tag{2.46}$$

$$\frac{\partial \varrho_i}{\partial t} + \nabla \cdot (\varrho_i \mathbf{V}_i) = 0\,, \tag{2.47}$$

$$\frac{\partial \varrho_n \mathbf{V}_n}{\partial t} + \nabla \cdot (\varrho_n \mathbf{V}_n \otimes \mathbf{V}_n + p_n \mathbf{I}) = \mathbf{R}_n^{ni} + \varrho_n \mathbf{g}\,, \tag{2.48}$$

$$\frac{\partial \varrho_i \mathbf{V}_i}{\partial t} + \nabla \cdot (\varrho_i \mathbf{V}_i \otimes \mathbf{V}_i + p_{ie} \mathbf{I}) + \mathbf{J} \times \mathbf{B} = \mathbf{R}_i^{in} + \varrho_i \mathbf{g}\,, \tag{2.49}$$

$$\frac{\partial E_n}{\partial t} + \nabla \cdot [(E_n + p_n)\mathbf{V}_n] = \mathbf{R}_n^{ni}\mathbf{V}_n + Q_n^{ni} + \varrho_n \mathbf{V}_n \cdot \mathbf{g}\,, \tag{2.50}$$

$$\frac{\partial E_i}{\partial t} + \nabla \cdot \left[\left(E_i + p_{ie} + \frac{\mathbf{B}^2}{2}\right)\mathbf{V}_i - \mathbf{B}(\mathbf{V} \cdot \mathbf{B})\right] = \mathbf{R}_i^{in}\mathbf{V}_i + Q_i^{in} + \varrho_i \mathbf{V}_i \cdot \mathbf{g}\,, \tag{2.51}$$

$$\frac{\partial \mathbf{B}}{\partial t} - \nabla \times (\mathbf{V_i} \times \mathbf{B}) + \nabla \cdot \psi \mathbf{I} = 0\,, \tag{2.52}$$

$$\frac{\partial \psi}{\partial t} + c_h^2 \nabla \cdot \mathbf{B} = -\frac{c_h^2}{c_p^2}\psi\,, \tag{2.53}$$

$$E_n = \frac{p_n}{\gamma - 1} + \frac{\varrho_n |\mathbf{V}_n|^2}{2}\,, \tag{2.54}$$

$$E_i = \frac{p_{ie}}{\gamma - 1} + \frac{\varrho_i |\mathbf{V}_i|^2}{2} + \frac{\mathbf{B}^2}{2}. \tag{2.55}$$

Rozdział 3

Numeryczny model atmosfery Słońca

Słońce powstało na wskutek gromadzenia się gazu molekularnego złożonego głównie z wodoru. Wraz ze wzrostem gęstości, temperatura oraz ciśnienie zaczęły wzrastać. Dzięki swojej masie, temperatura wewnątrz Słońca osiągnęła wartość wystarczającą do rozpoczęcia produkcji energii w wyniku fuzji jądrowej wewnątrz swojego jądra. Temperatura wewnątrz Słońca spada wraz z oddalaniem się od jądra. Towarzyszy jej spadek gęstości i ciśnienia. Energia we wnętrzu jest transportowana na zewnątrz w postaci promieniowania do otaczającej warstwy konwektywnej. Tam energia transportowana jest głównie w postaci konwekcji plazmy do górnych warstw. Następnie, energia przedostaje się do atmosfery i otaczającej Słońce korony słonecznej.

3.1 Budowa atmosfery Słońca

Atmosfera Słońca składa się z trzech warstw, gdzie pierwsze dwie rozciągają się na około 2100 km ponad warstwę konwektywną, co zostało przedstawione na rys. 3. Pierwszą z nich jest fotosfera, skąd większość promieniowania wydostaje się poza atmosferę Słońca. To właśnie promieniowanie z fotosfery dociera do Ziemi.

Chromosfera znajdująca się powyżej fotosfery sprawia, że intuicja dotycząca tego, że wraz z oddalaniem się od źródła ciepła temperatura spada, przestaje działać. To właśnie tutaj temperatura spada do koło 3500 K po to, aby wzrosnąć ponownie do 10^4 K tylko 2000 km nad fotosferą. Podwyższona temperatura chromosfery wskazuje, że aby dogrzać chromosferę do tak wysokiej temperatury, musi odbywać się transport energii z poniższych warstw. Spadkowi temperatury towarzyszy również wzrost ilości atomów neutralnych, których to uwzględnienie wydaje się kluczowe ze względu na to, że w szczytowym miejscu na jeden jon przypada 10^4 atomów neutralnych. Plazma w tym obszarze jest zatem tylko częściowo zjonizowana i nie oddziałuje już tak mocno na pole magnetyczne jak w warstwach niższych.

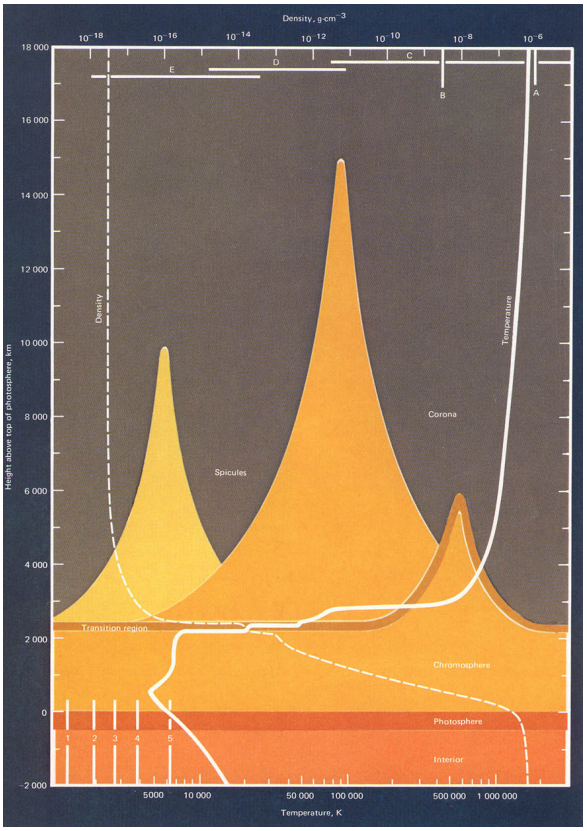

Rysunek 3.1: Przekrój atmosfery Słońca wraz z profilem temperatury oraz gęstości masy opracowany przez [5].

W obszarze przejściowym, znajdującym się nad chromosferą i mającym grubość około kilkuset km, temperatura gwałtownie wzrasta do koło 10^5 K, aby w znajdującej się powyżej koronie osiągnąć około 1-2 miliony K. Tutaj plazma jest już całkowicie zjonizowana.

Korona słoneczna rozciąga się na cały Układ Słoneczny, dając o sobie znać w postaci wiatru słonecznego, którym wypełnia przestrzeń międzyplanetarną.

3.2 Kod numeryczny JOANNA dla częściowo zjonizowanej plazmy

Opracowany przeze mnie kod numeryczny JOANNA (JOint ANalytical and Numerical Approach) pozwala na rozwiązywanie opisanych w poprzednim rozdziale równań dwupłynowych. Motywacją do napisania kodu była chęć zbadania wpływu cząstek naturalnych na atmosferę Słońca. W tym celu skupiłem się na wyspecjalizowaniu kodu tak, aby zawierał on całą niezbędną fizykę z punktu widzenia atmosfery Słońca. Obecnie dostępne kody numeryczne takie jak np. PLUTO [12] i FLASH [6] posiadają rozbudowane moduły pozwalające na obliczenia w różnych geometriach, czy też na użycie samoadaptujących się siatek numerycznych. Kody te ze względu na swoją złożoność są trudne w użytkowaniu i zaadoptowaniu do użycia dla konkretnych problemów. Złożoność kodu wpływa również negatywnie na jego ogólną stabilność i niezawodność.

Kod JOANNA został napisany w języku FORTRAN ze względu na łatwość użycia tego języka do celów naukowych. Sam kod został zorganizowany w taki sposób, aby każda cześć odpowiedzialna np. za problem Riemanna, była oddzielnym modułem zawierającym odwołania do innych modułów, które zawierają bloki odpowiedzialne za obliczenia. Tak zbudowany kod jest łatwy w zrozumieniu oraz w rozbudowie, ponieważ w celu dodania kolejnego modułu, zawierającego przydatną fizykę, wystarczy dodać nową procedurę obliczeniową bez znajomości struktury całego kodu i dopisać ją do głównego modułu odpowiedzialnego za ewolucję czasową równań.

W celu zwiększenia szybkości obliczeń ,kod został napisany przy użyciu biblioteki OPENMPI, która pozwala na łatwą implementację procedur odpowiedzialnych za działanie kodu na wielu procesorach. Kod został przetestowany standardowymi testami dla hydrodynamiki oraz magnetohydrodynamiki, które potwierdziły to, że kod rozwiązuje równania poprawnie.

Tak napisany kod, pozwala na szybkie uzyskanie wyników oraz możliwość jego łatwego rozwoju.

Rozdział 4

Wyniki badań własnych

4.1 Fale Alfvéna w jednopłynowej atmosferze Słońca

Uważa się, że fale Alfvéna są powszechne w atmosferze Słońca [20]. Jako, że fale te transportują energię wzdłuż pola magnetycznego, interesującym wdaje się sprawdzenie w jaki sposób fale Alfvéna rozchodzą się w osiowo symetrycznej tubie magnetycznej. Tego typu struktury i ich właściwości mogą przyczynić się do rozwiązania problemu ogrzewania korony słonecznej.

Model numeryczny

Do badań fal Alfvéna użyty został kod numeryczny PLUTO [12], który rozwiązuje idealne równania MHD w cylindrycznym układzie odniesienia. Jako pole magnetyczne wykorzystany został model opracowany przez [10]. Składowa θ prędkości została zaburzana okresowym oscylatorem

$$V_\theta(r,t) = \frac{r}{w}\ A_V\ \exp(-\frac{r^2}{\omega^2})\sin(\frac{2\pi}{P_d}t), \tag{4.1}$$

gdzie P_d jest okresem, A_V amplitudą i ω szerokością oscylatora umieszczonego w fotosferze. Przeprowadzony został szereg symulacji dla różnych wartości okresów oscylatora P_d.

Wyniki badań

Wyniki numeryczne pokazały, że fale Alfvéna są w stanie dotrzeć do korony słonecznej tylko jako zaburzenie składowej prędkości. W składowej magnetycznej fale te zanikają wraz z wysokością. Dla obydwu składowych wyznaczony został punkt zwrotny, powyżej którego zaburzenie przestaje mieć charakter oscylującej fali, a zaczyna wykładniczo zanikać. Fale Alfvéna o okresie zbliżonym do okresu odcięcia, czyli maksymalnego okresu, przy którym fale są w stanie się swobodnie rozchodzić, odbijają się częściowo od obszaru przejściowego i tworzą falę stojącą

w fotosferze i chromosferze. Ze względu na utratę zaburzenia w składowej magnetycznej, fale Alfvéna tracą swoją tożsamość i zachowują się inaczej w górnych warstwach atmosfery Słońca. Wyniki badań opublikowane zostały w pracy [27].

4.2 Fale Alfvéna o wysokiej częstotliwości

Fale Alfvéna o wysokiej częstotliwości (12-42 mHz) odkryto za pomocą obserwacji dokonanych szwedzkim naziemnym teleskopem słonecznym. Fale o tym zakresie częstotliwości zaobserwowano dla wielu przypadków tub magnetycznych [20]. Aby odpowiedzieć na pytanie ile energii przenoszą ze sobą fale Alfvéna o tak dużej częstości, istotnym stało się podparcie obserwacji za pomocą trójwymiarowych symulacji numerycznych.

Metodyka badań i model numeryczny

Badania obserwacyjne zostały wykonane za pomocą spektropolarymetru (CRISP), który posiada pole widzenia 60" x 60" (1"=725 km) oraz rozmiar pojedynczego piksela 0.0592". Po analizie falkowej dopplerogramów wykonanych dla długości fali H_α znaleziono fale o okresie 47 sekund. Fale o tym okresie nie zostały wcześniej zaobserwowane. W celu poparcia badań obserwacyjnych, wykonano symulacje numeryczne za pomocą kodu FLASH w trójwymiarowej geometrii. Do symulacji wykorzystano również trójwymiarowy model tuby magnetycznej, w podstawie której umieszczono oscylator w prędkości. Obliczony został strumień energii przenoszony za pomocą fal Alfvéna

$$W = \frac{1}{2}\varrho V_A V_\theta, \tag{4.2}$$

gdzie ϱ jest gęstością płynu, V_A prędkością Alfvéna a V_θ prędkością płynu.

Wyniki

Znaleziono obserwacyjne dowody na występowanie fal Alfvéna o wysokiej częstotliwości. Przeprowadzona analiza wyników numerycznych doprowadziła do konkluzji, że w tubie magnetycznej fale Alfvéna przenoszą strumień energii o wartościach 10^3 W m^{-2}. Wyliczone wartości pokazują, że fale Alfvéna są potencjalnym kandydatem do ogrzewania korony słonecznej. Niewyjaśniony pozostaje jednak sposób deponowania tej energii w koronie słonecznej, co sugeruje konieczność przeprowadzenia dalszych badań dotyczących fal Alfvéna. Wyniki badań opublikowane zostały w pracy [20].

4.3 Dwupłynowe symulacje spikul

Za pomocą nowo opracowanego kodu numerycznego JOANNA, uzyskano dwuwymiarowe symulacje numeryczne spikul. Spikule są to cienkie wyrzuty plazmy, które są dominującym zjawiskiem w dolnych warstwach korony. Mogą one powstawać w wyniku uwalniania energii w dolnych warstwach atmosfery słonecznej, np. w skutek anihilacji pola magnetycznego.

Model numeryczny

Symulacje numeryczne zostały przeprowadzone za pomocą kodu numerycznego JOANNA. Równania użyte do opisania ewolucji jonów i cząstek neutralnych opisane zostały przez Smith i [17]. Wykorzystany model tuby magnetycznej opierał się na dwuwymiarowych równaniach opracowanych przez [10].

Wyniki symulacji

Przeprowadzone symulacje numeryczne uwidoczniły odmienne zachowanie jonów i cząstek neutralnych. Średni przepływ rzędu $20 - 25$ km s^{-1} wywołany przez spikulę pasuje do danych obserwacyjnych i potwierdza dane otrzymane w wyniku symulacji MHD. Analiza temperatury i gęstości masy wewnątrz spikuli pokazuje, że otrzymane dane pasują do danych otrzymanych obserwacyjnie. Symulacje numeryczne spikul w modelu dwupłynowym pokazują, że model ten potwierdził nie tylko wyniki uzyskane w modelu MHD, ale również to, że wyniki modelu dwupłynowego pasują do danych obserwacyjnych. Rdzeń spikuli wykazuje większą gęstość cząstek neutralnych wraz z rosnącym w czasie rozrzedzeniem jonów. Wyniki opublikowane zostały w pracy [7].

4.4 Fale akustyczne: okresy odcięcia, wnęka chromosferyczna i tunelowanie fal

Przeprowadzone zostały symulacje numeryczne mające na celu zbadanie fizyki dwupłynowych fal akustycznych rozchodzących się w atmosferze Słońca. Do tego celu użyto dwupłynowego modelu atmosfery Słońca wraz z dwupłynowym kodem JOANNA. Symulacje miały na celu pokazanie zależności częstości odcięcia dla fal akustycznych od wysokości w atmosferze. Ze względu na częściowe odbicia, fale te interferują ze sobą oraz wzbudzają okresy zbliżone do lokalnego okresu odcięcia P_{ac}.

Model numeryczny

Do symulacji użyty został kod JOANNA z równaniami dwupłynowymi opisanymi w rozdziale 2. Model zakładał jednakową początkową temperaturę jonów, elektronów i cząstek neutralnych. Użyto monochromatycznego oscylatora, który generował fale o określonym okresie w fotosferze. Zaburzeniom podlegały jednocześnie cząstki zjonizowane jak i neutralne.

Wyniki symulacji

Otrzymane wyniki pokazują, że fale o okresie niższym niż okres lokalnego odcięcia, są w stanie przedostać się z fotosfery do korony. W przypadku, gdy okres fali $P > P_{ac}$, wygenerowane fale akustyczne wzbudzają okres równy P_{ac}, który następnie rozchodzi się w atmosferze i tuneluje przez obszar przejściowy do korony. W trakcie analizy gęstości mas jonów i neutrali zauważono, że zachowują się one odmiennie od siebie. Uzyskane wyniki pokazują, że model dwupłynowy daje nowe możliwości badania atmosfery Słońca, a na zachowanie się fal ma wpływ wzajemna interakcja cząstek neutralnych i zjonizowanych. Wyniki opublikowane zostały w pracy [26].

4.5 Mody entropii jako źródło energii dla aktywnych obszarów korony słonecznej

Do potrzymania wysokiej temperatury panującej w aktywnych obszarach korony słonecznej wymagany jest duży strumienia energii (około $10^3 \mathrm{Wm}^{-2}$). Wciąż nie jest jasne, w jaki sposób takie ilości energii są dostarczane. Przy użyciu danych pochodzących z IRIS (Interface Region Imaging Spectograph), udało się zaobserwować mody entropii w pętlach magnetycznych. W przeciwieństwie do zwykłych szoków, mody entropii zwane też pseudoszokami, wykazują nieciągłość tylko w gęstości masy. W ramach badań wykonano również dwupłynowe symulacje numeryczne, dzięki którym wykazano, że fale te przenoszą strumień energii rzędu $10^3 \mathrm{Wm}^{-2}$, który odpowiada stratom energii w tym obszarze.

Model numeryczny

Przy użyciu opisywanego już wcześniej hydrostatycznego dwupłynowego modelu atmosfery Słońca wykonano symulacje numeryczne, mające na celu wytworzenie modów entropii. W symulacjach użyto konfiguracji pola magnetycznego, odpowiadającego zakrzywionemu polu w pętli koronalnej. Jako zaburzenie służy zależny od czasu impulsu w ciśnieniu, który naśladował proces uwalniania energii w trakcie rekoneksji magnetycznej. Impuls umiejscowiony został w chormosferze. Jest to istotne z tego względu, że plazma w tym obszarze jest tylko częściowo zjonizowana, a powolne i szybkie fale magnetoakustyczne są ze sobą słabo sprzężone.

Wyniki symulacji

Analiza czasowa i przestrzenna wytworzonej struktury wskazuje na to, że fale magnetoakustczyne szybko opuszczają obszar symulacji. Słaby powolny szok pozostawia za sobą mod entropii. Wytworzona struktura złożona jest z gęstej części umieszczonej na końcu dżetu oraz rozrzedzonego ogona. Swoim wyglądem dżet przypomina kijankę i tak też został nazwany. Najważniejszym wnioskiem płynącym z przeprowadzonych symulacji jest to, że strumień energii skojarzony z wytworzonym modem entropii wynosi od $9 \cdot 10^3$ W m^{-2} na wysokości 2.1 Mm do $1 \cdot 10^3$ W m^{-2} na wysokości 4.5 Mm nad fotosferą. Wygenerowany przepływ w gęstości masy rzędu 10^{-5} kg m^{-2} s^{-1} przyczynia się również do uzupełniania ubytku masy w koronie związanego z wiatrem słonecznym. Wyniki symulacji oraz obserwacji zostały opublikowane w pracy [19].

4.6 Generacja wiatru słonecznego

Wiatr słoneczny jest strumieniem naładowanych cząstek składających się głównie z elektronów, protonów oraz wodoru. Wypływa on ze Słońca do układu Słonecznego [15]. W pobliżu Ziemi możliwe jest zmierzenie szybkiego wiatru słonecznego mierzącego około 750 km s^{-1} wydobywającego się z rejonów polarnych Słońca. Występuje również powolny wiatr słoneczny wydobywający się z terenów równikowych i poruszający się z o połowę mniejsza prędkością.

W czasach pomiarów o wysokiej rozdzielczości, szczególną uwagę zwrócono na źródło wypływów plazmy, które tworzą wiatr słoneczny. Modele i obserwacje pokazały, że na wysokościach od 5 Mm do 20 Mm nad fotosferą, dostrzec można wiatr o prędkości 10 km s^{-1} [22, 23]. Odnotowano również, że modele MHD mogą być odpowiedzialne za wypływająca ze Słońca plazmę [13, 21, 18]. Pomimo powyższych osiągnięć, mechanizm generujący wypływy plazmy, nie został opisany i pozostaje jednym z centralnych problemów heliofizyki. Celem pracy było pokazanie jaki wpływ na generację wiatru słonecznego mają efekty dwupłynowe.

Model numeryczny

W modelu rozważano dwupłynową atmosferę Słońca. Model rozciągał się od warstwy konwektywnej, położonej 2.56 Mm poniżej fotosfery i aż do 30 Mm nad fotosferą. Atmosfera Słońca była przeniknięta pionowym oraz transwersalnym polem magnetycznym o wypadkowej wartości 5 Gs. W modelu użyto również modelu radiacji opisanego przez [1]. Układ został zaburzony w pionowej składowej prędkości jonów oraz cząstek neutralnych, za pomocą pola stochastycznego o bardzo małej amplitudzie.

Wyniki symulacji

Symulacje przeprowadzone były do czasu, aż atmosfera osiągnęła kwazi-stacjonarny stan. Około 300 s po rozpoczęciu symulacji powstają niestabilności w fotosferze, które rozpoczynają granulację, która zostaje w pełni rozwinięta po upływie około 1500 s. Dane są analizowane po upływie 2000 s. W tym samym czasie w atmosferze zaobserwować można tworzenie się tub magnetycznych. Badany model odpowiada więc modelowi dziury koronalnej. Z uzyskanych danych wynika, że w koronie pojawiają się silne strumienie cząstek o prędkościach osiągających 100 km s^{-1}, co pokazuje, że energia uwalniana na wskutek rekoneksji magnetycznej oraz efektów dwupłynowych pozwala przyspieszać plazmę. Bezpośrednią przyczyną powstawania tak silnych wypływów plazmy jest granulacja, która jest odpowiedzialna za dynamikę zachodzącą

w atmosferze.

Podsumowując, przeprowadzone badania pokazują w jaki sposób formują się wypływy plazmy na wysokościach od 5 Mm do 10 Mm nad fotosferą. Składają się one z strumieni złożonych z cząsteczek pochodzących z niższych warstw atmosfery. Badania pokazują, że liczne dżety wytworzone przez działającą w fotosferze granulację, są w stanie wygenerować nieprzerwany wypływ plazmy, który może się przełożyć na szybki wiatr słoneczny na wyższych wysokościach w koronie słonecznej. Wyniki symulacji oraz obserwacji zostały opublikowane w pracy [25].

Rozdział 5

Wnioski

Wyniki uzyskane za pomocą kodu numerycznego JOANNA pokazują, że model dwupłynowy jest naturalnym rozwinięciem badań prowadzonych za pomocą modelu MHD. Dwupłynowe symulacje pokazały odmienne zachowanie się płynu zjonizowanego i neutralnego oraz to, że ich oddziaływanie między sobą ma bezpośredni wpływ na obserwowane wielkości.

Za pomocą kodu udało się zbadać dwupłynowe spikule wygenerowane za pomocą impulsu w ciśnieniu, imitującego rekoneksję magnetyczną. Struktura wygenerowanej spikuli dała wgląd w rozkład cząstek zjonizowanych i neutralnych wewnątrz spikuli. Uzyskane za pomocą kodu dane numeryczne, pasują do danych obserwacyjnych, co pokazuje, że model dwupłynowy jest naturalnym rozwinięciem modelu MHD atmosfery Słońca.

Badanie fal akustycznych w modelu dwupłynowym dało potencjalne wytłumaczenie obserwowanych okresów w atmosferze Słońca. Pokazano, że dwupłynowe fale akustyczne o okresach większych niż okres odcięcia generują fale o okresie równym lokalnemu okresowi odcięcia P_{ac}. Pokazano, że fale o okresach większych niż P_{ac} są w stanie przedostać się do korony słonecznej.

Dzięki współpracy z zespołem z Indii udało się zaobserwować oraz skonstruowano model numeryczny fal entropii, które przenoszą odpowiednią ilość energii, aby ogrzać aktywne obszary Słońca.

Przeprowadzono również symulacje granulacji w dwupłynowym modelu atmosfery Słońca. Z symulacji wynika, że w przypadku konfiguracji pola magnetycznego odpowiadającego dziurze koronalnej, granulacja w modelu dwupłynowym może generować wiatr słoneczny.

Kolejnym etapem badań nad atmosferą Słońca byłoby rozwinięcie obecnych dwupłynowych, 2.5 wymiarowych modeli na modele trójwymiarowe. W ten sposób możliwe byłoby zbadanie bardziej realistycznej granulacji. Modele 3D dałyby większy wgląd na ewolucję wiatru słonecznego, generację dżetów i spikul. Ciekawe też z perspektywy badań 3D byłyby badania przy

wykorzystaniu modelu arkady magnetycznej. Badania przeprowadzone w ramach tej pracy są tylko wstępem do wielu innych wymagających, ale też bardzo ciekawych projektów.

Dalsze badania przeprowadzone za pomocą opracowanego kodu JOANNA mogą w znaczący sposób przyczynić się do rozwiązania problemów fizyki Słońca i pomóc rozwiązać paradoks ogrzewania korony słonecznej. Dotychczas uzyskane wyniki dają perspektywę badań numerycznych i otwierają drzwi do niezbadanych obszarów fizyki.

Rozdział 6

Lista artykułów

Lista opublikowanych prac, które składają się na tą pracę, i w których jestem głównym autorem lub współautorem:

1. **Wójcik, D.**, Murawski K., Musielak, Z.E., Konkol, P., Mignone, A., *Numerical Simulations of Torsional Alfvén Waves in Axisymmetric Solar Flux Tubes*, 2017, Solar Physics, 292,31

2. Srivastava, A.K., Shetye, J., Murawski, K., Doyle, J.G., Stangalini, M., Scullion, E., Ray, T., **Wójcik, D.**, Dwivedi, B.N., *High-frequency torsional Alfvén waves as an energy source for coronal heating*, 2017, Scientific reports, 7, 1

3. Kuźma, B., Murawski, K., Kayshap, P., **Wójcik, D.**, Srivastava A.K., Dwivedi, B.N., *Two-fluid Numerical Simualtions of Solar Spicules*, 2017, The Astrophysical Journal, 842,2

4. **Wójcik, D.**, Murawski K., Musielak, Z.E., *Acoustic waves in two-fluid solar atmosphere model: cut-off periods, chromospheric cavity, and wave tunnelling*, 2018, Monthly Notices of the Royal Astronomical Society, 481, 262-267

5. Srivastava, A.K., Murawski, K., Kuźma, B., **Wójcik, D.**, Zaqarashvili, T.V., Stangalini, M., Musielak, Z.E., Doyle, J.G., Kayshap, P., Dwivedi, B.N., *Confined pseudo-shocks as an energy source for the active solar corona*, 2018, Nature Astronomy, 2, 12

6. **Wójcik, D.**, Kuźma, B., Murawski K., Srivastava, A.K., *Two-fluid, numerical simulations of the origin of the fast solar wind*, 2017, The Astrophysical Journal, przyjęte do druku

Solar Phys (2017) 292:31
DOI 10.1007/s11207-017-1058-7

Numerical Simulations of Torsional Alfvén Waves in Axisymmetric Solar Magnetic Flux Tubes

D. Wójcik[1] · K. Murawski[1] · Z.E. Musielak[2,3] · P. Konkol[1] · A. Mignone[4]

Received: 4 July 2016 / Accepted: 17 January 2017 / Published online: 31 January 2017

Abstract We numerically investigate Alfvén waves propagating along an axisymmetric and non-isothermal solar flux tube embedded in the solar atmosphere. The tube magnetic field is current-free and diverges with height, and the waves are excited by a periodic driver along the tube magnetic field lines. The main results are that the two wave variables, the velocity and magnetic field perturbations in the azimuthal direction, behave differently as a result of gradients of the physical parameters along the tube. To explain these differences in the wave behavior, the time evolution of the wave variables and the resulting cutoff period for each wave variable are calculated and used to determine regions in the solar chromosphere where strong wave reflection may occur.

Keywords Waves: Alfvén

1. Introduction

Observations by several recently launched spacecraft have revealed the ubiquitous presence of oscillations in the solar atmosphere, which can be interpreted as magnetohydrodynamic (MHD) waves (*e.g.* Nakariakov and Verwichte, 2005) or specifically as Alfvén waves whose signatures were observed in prominences, spicules, and X-ray jets by Okamoto *et al.* (2007), De Pontieu *et al.* (2007) and Cirtain *et al.* (2007), respectively. Moreover, observational evidence for the existence of torsional Alfvén waves in the solar atmosphere was given by Jess *et al.* (2009), see however Dwivedi and Srivastava (2010) and Okamoto and de Pontieu

D. Wójcik
dwojcik@kft.umcs.lublin.pl

1 Group of Astrophysics, Faculty of Mathematics, Physics and Informatics, UMCS, ul. Radziszewskiego, 20-031 Lublin, Poland

2 Department of Physics, University of Texas at Arlington, Arlington, TX 76019, USA

3 Kiepenheuer-Institut für Sonnenphysik, Schöneckstr. 6, 79104 Freiburg, Germany

4 Dipartimento di Fisica Generale Facoltá di Scienze M.F.N., Universitá degli Studi di Torino, 10125 Torino, Italy

(2011) who reported the presence of propagating Alfvén waves in solar spicules. Alfvén waves have been of a particular interest because they can carry energy and momentum along magnetic field lines to the solar corona, where the wave energy can heat the corona and the wave momentum may accelerate the solar wind.

There is a large body of literature devoted to Alfvén waves and their propagation in the solar atmosphere (Zhugzhda and Locans, 1982; Hollweg, Jackson, and Galloway, 1982; An *et al.*, 1989; Hollweg, 1990; Musielak, Fontenla, and Moore, 1992; Musielak and Moore, 1995; Kudoh and Shibata, 1999; Hollweg and Isenberg, 2007; Musielak, Routh, and Hammer, 2007; Murawski and Musielak, 2010; Routh, Musielak, and Hammer, 2010; Webb *et al.*, 2012; Chmielewski *et al.*, 2013; Murawski, Srivastava, and Musielak, 2014; Perera, Musielak, and Murawski, 2015). There are two main problems considered in these articles: the propagation conditions for Alfvén waves, and the dissipation of energy and momentum carried by these waves. The first problem involves the concept of the cutoff frequency, which is caused by strong gradients of the physical parameters in the solar atmosphere. The cutoff frequency has been explored for linear Alfvén waves by Murawski and Musielak (2010) and Perera, Musielak, and Murawski (2015) and for torsional Alfvén waves in thin magnetic flux tubes by Musielak, Routh, and Hammer (2007) and Routh, Musielak, and Hammer (2010). The second problem deals with coronal heating (Suzuki and Inutsuka, 2005), and it involves different mechanisms of Alfvén wave dissipation, such as phase-mixing (Ofman and Davila, 1995) or nonlinear mode coupling (Ulmschneider, Zähringer, and Musielak, 1991), and wave momentum deposition (Dwivedi and Srivastava, 2006; Chmielewski *et al.*, 2013, 2014); however, a realistic modeling of both Alfvén wave propagation and dissipation is difficult to perform (Banerjee, Hasan, and Christensen-Dalsgaard, 1998; O'Shea, Banerjee, and Doyle, 2005; Bemporad and Abbo, 2012; Chmielewski *et al.*, 2013; Jelínek *et al.*, 2015).

Murawski and Musielak (2010) considered impulsively generated Alfvén waves in a one-dimensional solar atmosphere with a smoothed step-wise temperature profile and a vertical magnetic field. Perera, Musielak, and Murawski (2015) studied analytically and numerically the case of periodically driven Alfvén waves and their propagation in an isothermal solar atmosphere. Musielak, Routh, and Hammer (2007) and Routh, Musielak, and Hammer (2010) investigated torsional Alfvén waves propagating in thin magnetic flux tubes embedded in an isothermal and non-isothermal solar atmosphere. The main aim of this article is to extend the work of Murawski and Musielak (2010) and Perera, Musielak, and Murawski (2015) to an axisymmetric solar magnetic flux tube embedded in a solar atmosphere with the realistic temperature profile of Avrett and Loeser (2008) and curved magnetic field lines (Low, 1985), to perform numerical simulations of the propagation of torsional Alfvén waves, and to compare the obtained numerical results to the analytical results obtained by Routh, Musielak, and Hammer (2010).

This article is organized as follows. The numerical model of the solar atmosphere is described in Section 2. The numerical and analytical results are presented and discussed in Sections 3 and 4, respectively. Our discussion of the analytical and numerical results is given in Section 5, and a short summary of the results and some concluding remarks are presented in Section 6.

2. Numerical Model

We consider a magnetically structured and gravitationally stratified solar atmosphere that is described by the following set of ideal MHD equations:

$$\frac{\partial \varrho}{\partial t} + \nabla \cdot (\varrho \boldsymbol{V}) = 0, \tag{1}$$

$$\varrho \frac{\partial \boldsymbol{V}}{\partial t} + \varrho(\boldsymbol{V} \cdot \nabla)\boldsymbol{V} = -\nabla p + \frac{1}{\mu}(\nabla \times \boldsymbol{B}) \times \boldsymbol{B} + \varrho \boldsymbol{g}, \tag{2}$$

$$\frac{\partial \boldsymbol{B}}{\partial t} = \nabla \times (\boldsymbol{V} \times \boldsymbol{B}), \qquad \nabla \cdot \boldsymbol{B} = 0, \tag{3}$$

$$\frac{\partial p}{\partial t} + \boldsymbol{V} \cdot \nabla p = -\gamma p \nabla \cdot \boldsymbol{V}, \quad p = \frac{k_{\mathrm{B}}}{m} \varrho T, \tag{4}$$

where ϱ is the mass density, p is the gas pressure, $\boldsymbol{V}$ is the plasma velocity, $\boldsymbol{B}$ the magnetic field, and $\boldsymbol{g} = (0, -g, 0)$ is the gravitational acceleration of magnitude 274 m s^{-2}. The symbol T denotes temperature, m is the particle mass, specified by a mean molecular weight of 1.24, k_{B} is the Boltzmann constant, $\gamma = 1.4$ is the adiabatic index, and μ the magnetic permeability of plasma.

We consider the axisymmetric case in which all plasma variables are invariant in the azimuthal direction θ, but the θ-components of the perturbed magnetic field B_θ and velocity V_θ are not identically zero. We assume that the equilibrium magnetic field is current-free, $\nabla \times \boldsymbol{B} = \boldsymbol{0}$, and its components along the radial (r), azimuthal (θ), and vertical (y), directions are specified by the following expressions:

$$B_{\mathrm{e}r} = \frac{3Sr(y-a)}{(r^2 + (y-a)^2)^{\frac{5}{2}}}, \tag{5}$$

$$B_{\mathrm{e}\theta} = 0, \tag{6}$$

$$B_{\mathrm{e}y} = \frac{S(r^2 - 2(y-a)^2)}{(r^2 + (y-a)^2)^{\frac{5}{2}}} + B_{\mathrm{e}_0}, \tag{7}$$

where a and S are free parameters that denote the vertical location of the magnetic moment and the vertical magnetic field strength, respectively. Equations (5)–(7) comprise a special (potential and axisymmetric) case of the three-dimensional model that was developed by Low (1985). We set $a = -0.75$ Mm, choose S such that at $r = 0$ Mm and $y_{\mathrm{r}} = 6.0$ Mm the magnetic field is $B_{\mathrm{e}} = B_{\mathrm{e}y} = 9.5$ Gs. Here, $y = y_{\mathrm{r}}$ denotes the reference level. The magnetic field vectors resulting from these equations are drawn in Figure 1. The magnetic field lines are curved and the curvature decays with height y and grows with the radial distance r, and the magnitude of $\boldsymbol{B}_{\mathrm{e}}$ decays with y and r.

As the equilibrium magnetic field, specified by Equations (5)–(7), is current-free, the equilibrium gas pressure and mass density are hydrostatic, and they are given as (*e.g.* Murawski *et al.*, 2015a)

$$p_{\mathrm{h}}(y) = p_0 \exp\left[-\int_{y_{\mathrm{r}}}^{y} \frac{\mathrm{d}y'}{\Lambda(y')}\right], \qquad \varrho_{\mathrm{h}}(y) = -\frac{1}{g}\frac{\partial p_{\mathrm{h}}}{\partial y}, \tag{8}$$

where $p_0 = 0.01$ Pa is the gas pressure evaluated at $y = y_{\mathrm{r}}$,

$$\Lambda(y) = \frac{k_{\mathrm{B}} T_{\mathrm{h}}(y)}{mg} \tag{9}$$

is the pressure scale-height, and the symbol $T_{\mathrm{h}}(y)$ denotes the hydrostatic temperature profile specified in the model of Avrett and Loeser (2008).

In the model, the solar photosphere occupies the region $0 < y < 0.5$ Mm, the chromosphere resides in 0.5 Mm $< y <$ 2.1 Mm, and the solar corona is represented by higher atmospheric layers, which start from the transition region that is located at $y \approx 2.1$ Mm.

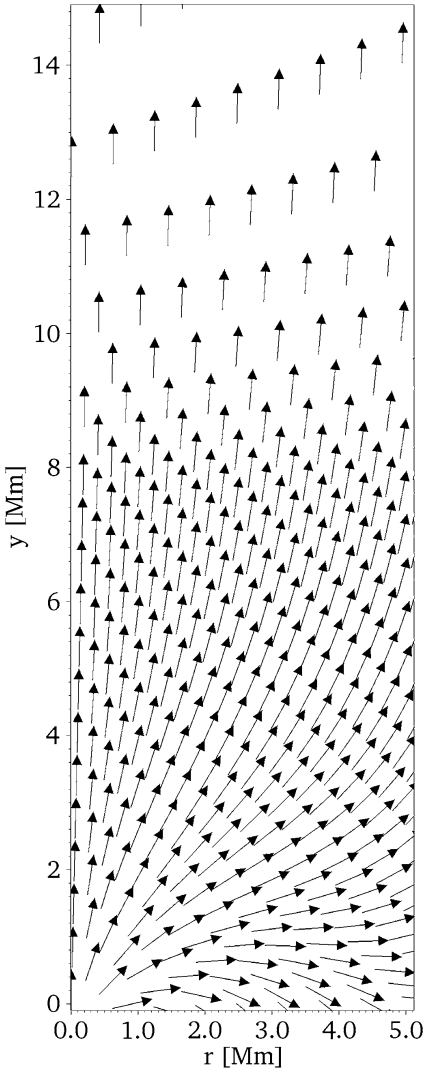

Figure 1 Magnetic field vectors.

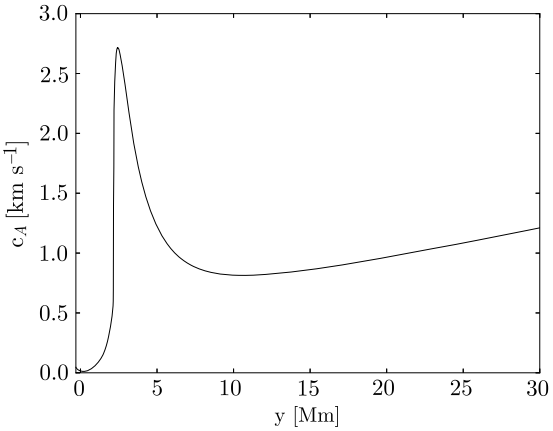

Figure 2 Vertical profile of Alfvén speed c_A for $r = 0$ Mm at the equilibrium conditions of Equations (5) – (8).

Note that the gas pressure and mass density do not vary with the radial distance r, in equilibrium, while they fall off with the height y (not shown).

Figure 2 shows the vertical profile of the Alfvén speed $c_\mathrm{A} = B_\mathrm{e}/\sqrt{\mu\varrho_\mathrm{h}}$ along the central axis, $r = 0$ Mm, with $c_\mathrm{A} = 12$ km s^{-1} at $y = 0$ Mm. Higher up, c_A grows with y, reaching a maximal value of 2715 km s^{-1} at $y = 2.44$ Mm, and then c_A falls off with height. This characteristic shape of the Alfvén velocity profile will have a prominent effect on the wave behavior in our model, as shown and discussed in Section 3.

3. Numerical Results

Numerical simulations are performed using the PLUTO code, which is based on a finite-volume and finite-difference method (Mignone *et al.*, 2007, 2012), designed to solve a system of conservation laws on structured meshes. For all considered cases we set the simulation box as 0 to 5.12 Mm in the r direction and -0.1 Mm to 30 Mm in the y direction. We impose the boundary conditions by fixing all plasma quantities to their equilibrium values at the top and bottom of the simulation region, while at the right boundary, outflow boundary conditions are implemented. These outflow boundary conditions do no lead to any incoming signal reflection as we use the background magnetic field splitting (Mignone *et al.*, 2007). At $r = 0$ Mm axisymmetrical boundaries are implemented. Along the r-direction this simulation box is divided into 1024 cells, along the y-direction it is divided into 1536 cells for $-0.1 < y < 7.58$ Mm, and it is divided into 512 cells in the range of $7.58 < y < 30$ Mm.

For our problem, the Courant–Friedrichs–Lewy number is set to 0.3 and the Harten–Lax–van Leer discontinuities (HLLD) approximate Riemann solver (Miyoshi and Kusano, 2005) is adopted. At the bottom boundary the periodic driver is additionally set as

$$V_\theta(r,t) = \frac{r}{w} A_V \exp\left(-\frac{r^2}{w^2}\right) \sin\left(\frac{2\pi}{P_\mathrm{d}} t\right), \tag{10}$$

where P_d is the period of the driver, A_V is the amplitude of the driver, and w is its spatial width. We set and hold fixed $w = 100$ km and $A_V = 5\ \mathrm{km\,s^{-1}}$ while allowing P_d to vary.

Figure 4 illustrates the r–y spatial profiles of V_θ (left) and B_θ (right) for $P_\mathrm{d} = 35$ s, which corresponds to an effective amplitude of the driver of about $0.2\ \mathrm{km\,s^{-1}}$. It is seen in $V_\theta(r, y)$ that this driver excites Alfvén waves that penetrate the chromosphere, and at $t \approx 70$ s reach the transition region and the solar corona. As a result of the Alfvén speed profile, displayed in Figure 2, the Alfvén waves accelerate up to the altitude where c_A attains its maximal value, and higher up, the Alfvén waves decelerate.

Note that as a consequence of the divergence of the magnetic field with height (Figure 1), the wave front spreads with height and magnetic shells develop in time (Murawski *et al.*, 2015b) and a standing wave pattern is present in the low photosphere, below $y \approx 0.5$ Mm. A qualitatively similar scenario can be seen in the low atmospheric layers in profiles of $B_\theta(r, y)$ (Figure 4, right). However, the perturbations in B_θ decay with altitude, remaining largest in low atmospheric regions. This conclusion confirms the former findings of Murawski and Musielak (2010). The patterns of standing waves and magnetic shells are easily seen below the transition region.

Figure 3 displays the vertical profiles of V_θ (left) and B_θ (right) at $r = 0.1$ Mm. The penetration of Alfvén waves into the solar corona is seen in the V_θ profiles (left). These results clearly show that the wave variables behave differently, namely the gradients in physical parameters have stronger effects on B_θ than on V_θ because the former decays rapidly with height, while the latter reaches the solar corona; the fact that the Alfvén wave variables behave differently is a well-known phenomenon (*e.g.* Hollweg, Jackson, and Galloway, 1982; Musielak, Fontenla, and Moore, 1992; Musielak and Moore, 1995; Musielak, Routh, and Hammer, 2007; Murawski and Musielak, 2010; Routh, Musielak, and Hammer, 2010; Perera, Musielak, and Murawski, 2015). The gradients are the main physical reason for this different behavior of V_θ and B_θ, and they also lead to wave reflection, which occurs below $y \approx 1.75$ Mm and decays with time; the waves that undergo reflection become trapped, and this trapping dominates in the upper parts of the solar chromosphere. Similar to $V_\theta(r = 0.1\ \mathrm{Mm}, y, t)$, the profiles of B_θ reveal the transient phase, which occurs for $t \lesssim 150$ s, but later on, the oscillations in B_θ reach a quasi-stationary stage (bottom).

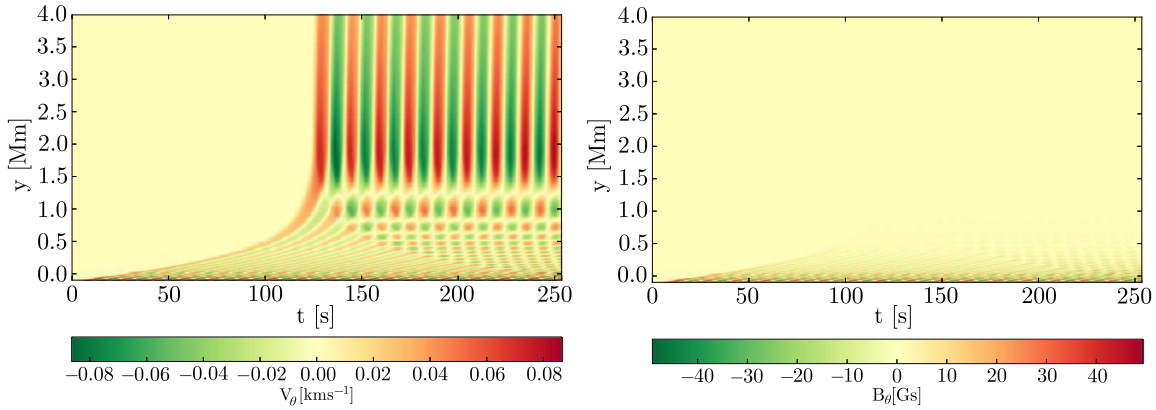

Figure 3 Vertical profiles of V_θ (left) and B_θ (right) for $r = 0.1$ Mm *vs.* time for $P_{\rm d} = 35$ s.

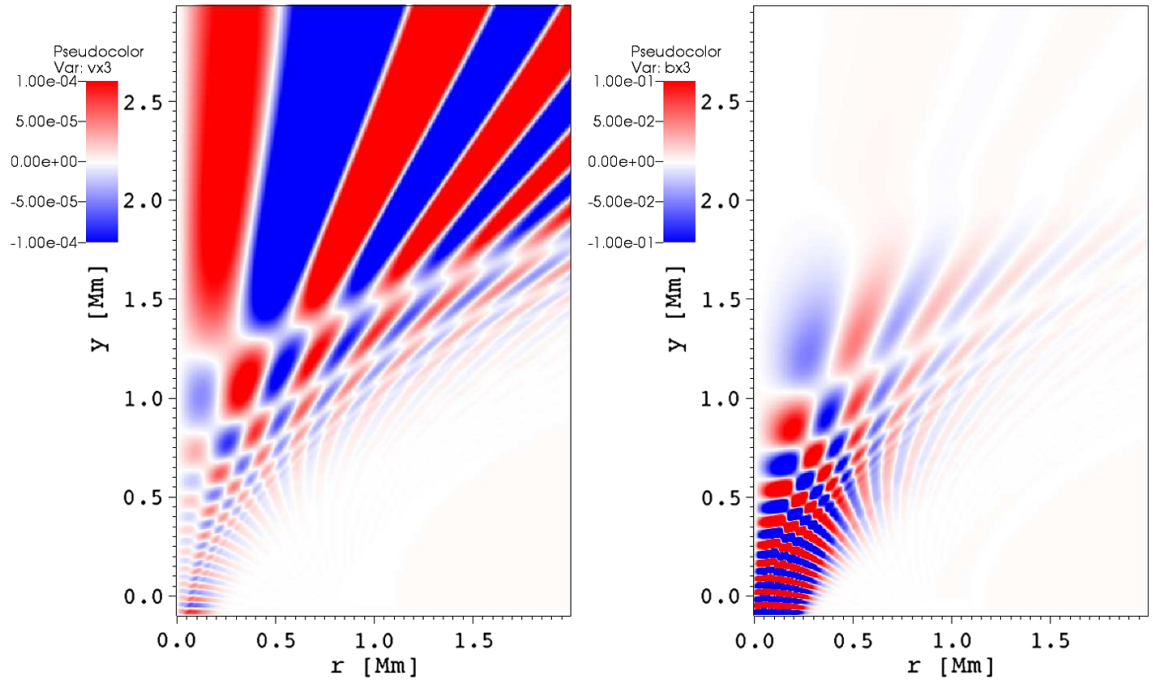

Figure 4 Spatial profile of V_θ (left) and B_θ (right) for $P_{\rm d} = 35$ s at $t = 340$ s.

These numerical results have important physical implications: they show that Alfvén waves do lose their characteristics because their wave velocity and magnetic field variables behave differently. Since the wave velocity variable reaches the corona and the wave magnetic field variable cannot, the Alfvén wave in the solar corona no longer obeys equipartition of energy between the two wave variables. This means that the physical nature of the Alfvén wave in the solar corona is different than in the solar chromosphere. The problem is beyond the scope of this article, but it does require future studies.

4. Cutoff Periods for Torsional Waves in Thin Flux Tubes

To compare the results of our numerical simulations to the analytically determined conditions for the propagation of torsional Alfvén waves in a solar magnetic flux tube, we follow Musielak, Routh, and Hammer (2007) and Routh, Musielak, and Hammer (2010). With

the wave variables $\boldsymbol{v} = v_\theta(r, y, t)\hat{\boldsymbol{\theta}}$ and $\boldsymbol{b} = b_\theta(r, y, t)\hat{\boldsymbol{\theta}}$, we follow Musielak, Routh, and Hammer (2007) and write the θ-components of the linearized equations of motion and of induction as

$$\frac{\partial(v_\theta/r)}{\partial t} - \frac{1}{\mu\rho_{\rm h}r^2}\left[B_{\rm er}(r, y)\frac{\partial}{\partial r} + B_{\rm ey}(r, y)\frac{\partial}{\partial y}\right](rb_\theta) = 0, \tag{11}$$

and

$$\frac{\partial(rb_\theta)}{\partial t} - r^2\left[B_{\rm er}(r, y)\frac{\partial}{\partial r} + B_{\rm ey}(r, y)\frac{\partial}{\partial y}\right](v_\theta/r) = 0. \tag{12}$$

According to Musielak, Routh, and Hammer (2007), the thin flux tube approximation gives the following relationship:

$$B_{\rm er}(r, y) = -\frac{r}{2}\frac{{\rm d}B_{\rm ey}}{{\rm d}y}, \tag{13}$$

which allows writing Equations (11) and (12) as

$$\frac{\partial v_\theta}{\partial t} + \frac{1}{2\rho_{\rm h}}\left(r\frac{\partial b_\theta}{\partial r} + b_\theta\right)\frac{{\rm d}B_{\rm ey}}{{\rm d}y} - \frac{B_{\rm ey}}{\rho_{\rm h}}\frac{\partial b_\theta}{\partial y} = 0, \tag{14}$$

and

$$\frac{\partial b_\theta}{\partial t} + \frac{1}{2}\left(r\frac{\partial v_\theta}{\partial r} - v_\theta\right)\frac{{\rm d}B_{\rm ey}}{{\rm d}y} - B_{\rm ey}\frac{\partial v_\theta}{\partial y} = 0. \tag{15}$$

Assuming the tube is in temperature equilibrium with its surroundings, Routh, Musielak, and Hammer (2010) used horizontal pressure balance and obtained the following wave equations for torsional Alfvén waves:

$$\frac{\partial^2 v_\theta}{\partial t^2} - c_A^2\frac{\partial^2 v_\theta}{\partial y^2} + \frac{c_A^2}{2H}\frac{\partial v_\theta}{\partial y} - \frac{c_A^2}{4H^2}\left(\frac{1}{4} + \frac{{\rm d}H}{{\rm d}y}\right)v_\theta = 0, \tag{16}$$

and

$$\frac{\partial^2 b_\theta}{\partial t^2} - c_A^2\frac{\partial^2 b_\theta}{\partial y^2} - \frac{c_A^2}{2H}\left(1 + \frac{4H}{c_{\rm A}}\frac{{\rm d}c_{\rm A}}{{\rm d}y}\right)\frac{\partial b_\theta}{\partial y} - \frac{c_A^2}{4H^2}\left(\frac{1}{4} + \frac{2H}{c_{\rm A}}\frac{{\rm d}c_{\rm A}}{{\rm d}y} - \frac{{\rm d}H}{{\rm d}y}\right)b_\theta = 0, \tag{17}$$

where $H(y) = c_{\rm s}^2(y)/\gamma g$ is the pressure scale height, with $c_{\rm s}(y)$ being the sound speed, and $c_{\rm A}(y) = B_{\rm ey}(y)/\sqrt{\mu_0\rho_{\rm h}(y)}$ is the Alfvén velocity.

As demonstrated by Routh, Musielak, and Hammer (2010), the critical frequencies are given by

$$\Omega_{{\rm cr},v}^2(y) = \frac{1}{2}\left[\frac{1}{2}\left(\frac{{\rm d}c_{\rm A}}{{\rm d}y}\right)^2 - c_{\rm A}\left(\frac{{\rm d}^2c_{\rm A}}{{\rm d}y^2}\right)\right], \tag{18}$$

and

$$\Omega_{{\rm cr},b}^2(y) = \frac{1}{2}\left[\frac{1}{2}\left(\frac{{\rm d}c_{\rm A}}{{\rm d}y}\right)^2 + c_{\rm A}\left(\frac{{\rm d}^2c_{\rm A}}{{\rm d}y^2}\right)\right], \tag{19}$$

and the resulting turning-point frequencies become

$$\Omega_{{\rm tp},v}^2(y) = \Omega_{{\rm cr},v}^2(y) + \frac{1}{4t_{\rm ac}^2(y)}, \tag{20}$$

and

$$\Omega^2_{\mathrm{t}p,b}(y) = \Omega^2_{\mathrm{cr},b}(y) + \frac{1}{4t^2_{\mathrm{ac}}(y)}, \tag{21}$$

where t_{ac} is actual wave travel time expressed by

$$t_{\mathrm{ac}} = \int_{y_b}^{y} \frac{\mathrm{d}\widetilde{y}}{c_{\mathrm{A}}(\widetilde{y})}, \tag{22}$$

with y_b being an atmospheric height at which the wave is initially generated. Finally, the cut-off frequency for torsional Alfvén waves propagating in a thin and non-isothermal magnetic flux tube embedded in the solar atmosphere is

$$\Omega_{\mathrm{cut},\tau}(y) = \max\left[\Omega_{\mathrm{tp},\tau,v}(y), \Omega_{\mathrm{tp},\tau,b}(y)\right]. \tag{23}$$

After obtaining the turning-point frequencies and the cutoff frequency, we may define the turning-point periods as

$$P_{\mathrm{tp},v} = \frac{2\pi}{\Omega_{\mathrm{tp},v}}, \qquad P_{\mathrm{tp},b} = \frac{2\pi}{\Omega_{\mathrm{tp},b}}, \tag{24}$$

and the cutoff period is

$$P_{\mathrm{cut}} = \frac{2\pi}{\Omega_{\mathrm{cut}}}. \tag{25}$$

5. Discussion of Analytical and Numerical Results

Figure 5 displays the cutoff period, P_{cut}, *vs.* height y. At $y = 0$, which is the bottom of the photosphere, $P_{\mathrm{cut}} = 10$ s. It grows higher up, reaching its maximum value of about 300 s at $y \approx 0.2$ Mm, and subsequently it falls off with height to its global minimum of about 0.03 s, which occurs at the solar transition region. In the solar corona P_{cut} increases again with y, but its values are lower than 1 s. This general trend of $P_{\mathrm{cut}}(y)$ is consistent with that found by Murawski and Musielak (2010), but the exact values of $P_{\mathrm{cut}}(y)$ are different in the two cases. In particular, Murawski and Musielak (2010) found that for the straight vertical equilibrium the magnetic field P_{cut} was higher than 40 s, while Figure 5 reveals that the corresponding values are a fraction of 1 s. This clearly shows how strongly the cutoff depends on the geometry and strength of the background magnetic field.

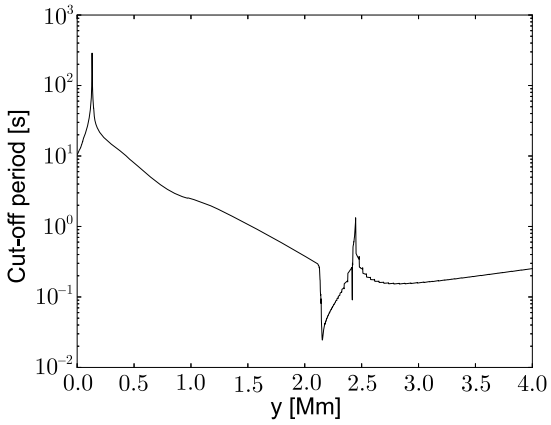

Figure 5 Cutoff period for Alfvén waves *vs.* height y calculated from Equations (23) and (25).

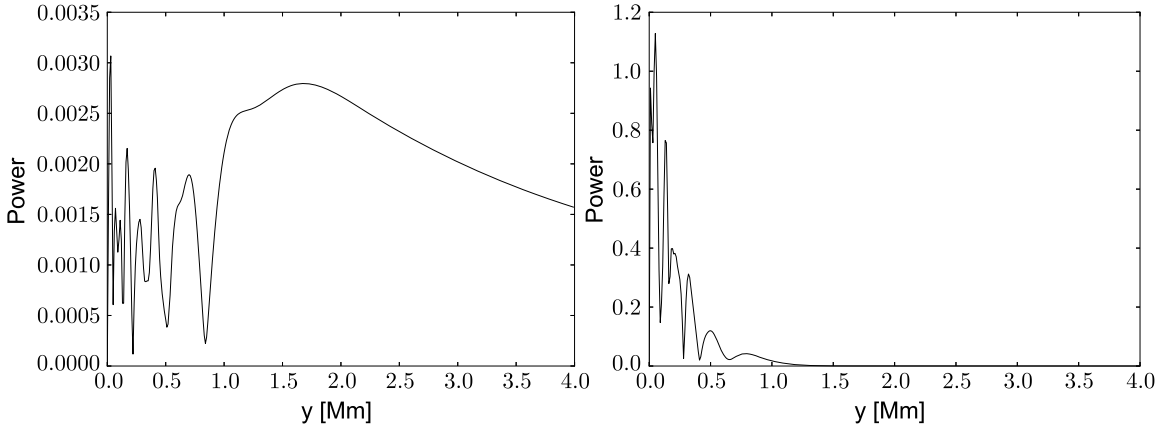

Figure 6 Spectral power (in arbitrary units) of Alfvén waves for wave period $P = 35$ s obtained from the time signatures of Figure 3 for $r = 0.1$ Mm and $t = 250$ s; for V_θ (left) and B_θ (right).

Our numerical results show that Alfvén waves – or at least their wave velocity perturbation – penetrate the transition region, whereas the magnetic field perturbation does not, as shown in Figures 3 and 4. The analytical results imply the same as they also show that the two wave variables behave differently. However, there are some discrepancies between the analytical and numerical results because the thin flux tube approximation, which is the basis for obtaining the cutoff frequency, does not apply to our model of the solar corona because the tube becomes thick and the condition given by Equation (13) is not satisfied any longer. The agreement between the analytical theory and our numerical model is better in the solar chromosphere where the tube remains thin.

Because of the different behavior of the two wave variables, we may look directly at the values of the turning-point frequencies given by Equations (20) and (21) for each wave variable. Since in the photosphere for 0.2 Mm $< y <$ 2.5 Mm, $P_{\mathrm{tp},b} = 0$, a signal in magnetic field is not able to penetrate this region, which explains why B_θ is absent in the solar corona (Figure 3, right). This is an important result that clearly shows the connections between the turning-point frequencies and the different behavior of the two wave variables. However, a signal can be seen in this region in V_θ (Figure 3, left). Indeed, for $P_{\mathrm{d}} = 35$ s the condition of $P < P_{\mathrm{tp},v}$ is satisfied only up to $y \approx 0.3$ Mm, while for $y \approx 0.1$ Mm $P < P_{\mathrm{tp},b}$. For higher values of y, we have $P > P_{\mathrm{tp},bv}$, and the Alfvén waves become evanescent.

Figure 6 illustrates the spectral power corresponding to $P_{\mathrm{d}} = 35$ s for V_θ (left) and B_θ (right). A sudden fall-off of power at $y \approx 0.2$ Mm corresponds to energy being spent on excitation of a non-zero signal in B_θ. Thus the energy moves from V_θ, in which it was originally generated, into B_θ. We point out that for linear Alfvén waves propagating in homogeneous media, there is a perfect equipartition of the wave kinetic energy associated with V_θ and the wave magnetic energy associated with B_θ; our results show that this perfect equipartition of wave energy is strongly violated in inhomogeneous media (see our comments at the end of Section 3).

In the solar corona the value of the P_{d} is higher then a local value of $P_{\mathrm{tp},v}$ and $P_{\mathrm{tp},b}$, therefore the waves are evanescent in this region. However, our numerical results show a tunneling of V_θ (left) to the solar corona with the signal in B_θ (right) falling off more strongly with height, with B_θ being practically zero above $y = 1.5$ Mm.

Figure 7 shows the vertical profiles of $V_\theta(r = 0.1$ Mm, $y)$ for several values of P_{d}. The location of the last zero of V_θ is assumed as the y-position of a turning point. Similar profiles are drawn for $B_\theta(r = 0.1$ Mm, $y)$ (see Figure 8). Note that oscillations take place until the zero of V_θ, and V_θ becomes evanescent higher up as it falls off with altitude above its local

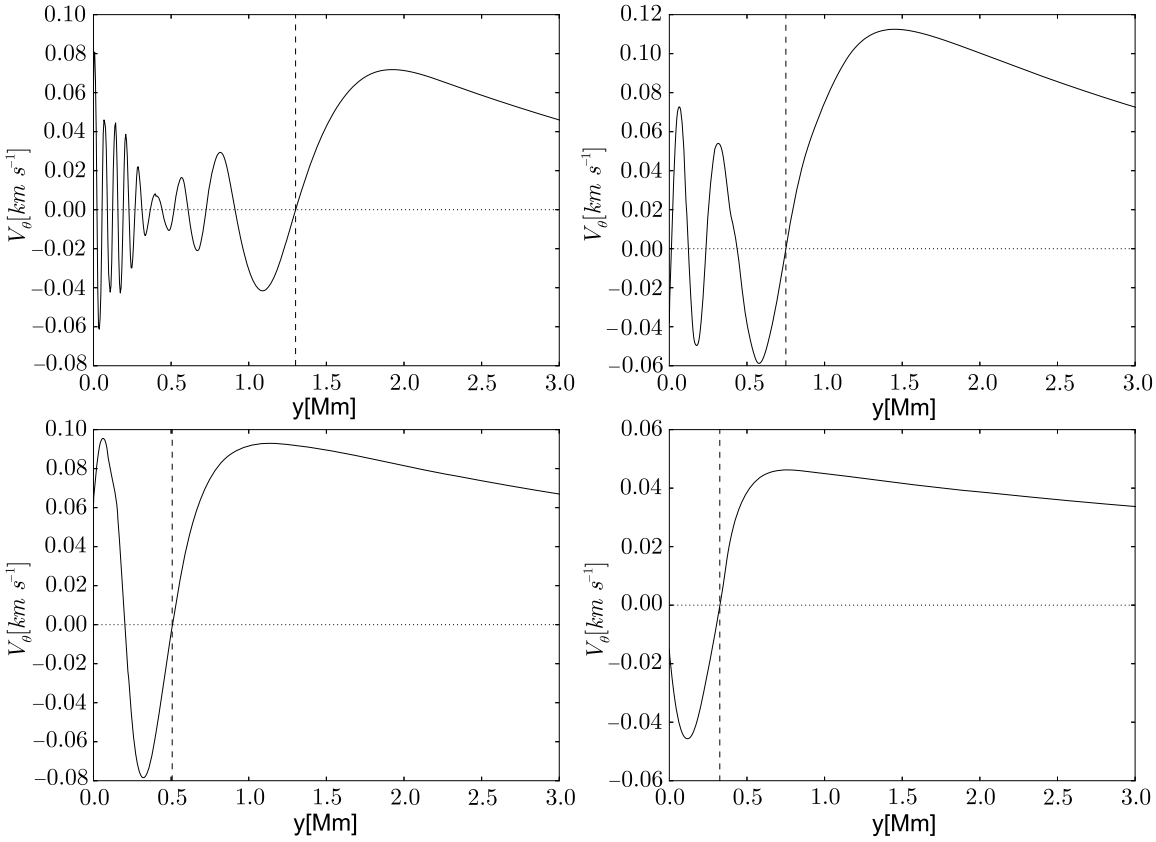

Figure 7 Plots of $V_\theta(r = 0.1$ Mm, $y)$ *vs.* the atmospheric height y with the locations of the turning point depicted by vertical dashed lines for $P_\mathrm{d} = 35$ s (top left), $P_\mathrm{d} = 50$ s (top right), $P_\mathrm{d} = 100$ s (bottom left), and $P_\mathrm{d} = 200$ s (bottom right).

maximum. The oscillatory behavior of B_θ until the last zero and its subsequent strong fall-off are clearly visible.

The turning points for V_θ and B_θ, which separate the oscillatory behavior of the wave variables from non-oscillatory behavior, are illustrated in Figure 9. Note that the turning points are located at lower heights for higher values of P_d with the falling-off trend confirming the numerical findings of Perera, Musielak, and Murawski (2015), and that the turning points for B_θ are located at lower altitudes (see Figure 9). There is strong consistency between our conclusions based on the cutoff and on the concept of turning points, and the reason is that these two concepts are related to each other (*e.g.* Musielak, Musielak, and Mobashi, 2006).

6. Summary and Concluding Remarks

In this article, we numerically simulate Alfvén waves that are driven by a periodic driver operating in the solar photosphere 100 km below the solar surface. Our findings can be summarized as follows.

a) A periodic driver located in the solar photosphere excites torsional Alfvén waves that propagate along an axisymmetric magnetic flux tube embedded in the solar chromosphere and corona.
b) We show that the azimuthal component of velocity V_θ and the azimuthal component of B_θ behave very differently in the solar atmosphere. V_θ propagates in the solar corona, while B_θ exhibits a strong fall-off trend with height.

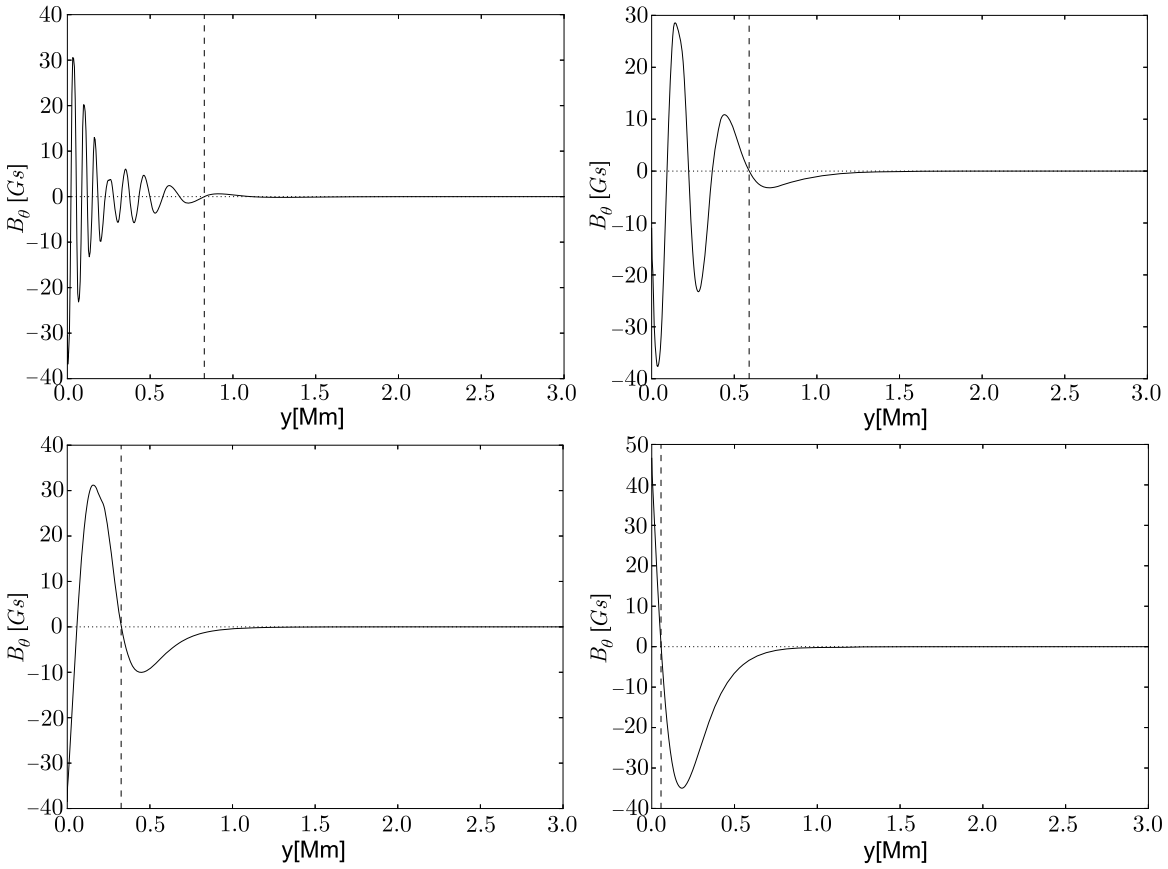

Figure 8 Plots of $B_\theta(r = 0.1$ Mm, $y)$ *vs.* the atmospheric height y with the locations of the turning point depicted by vertical dashed lines for $P_\mathrm{d} = 35$ s (top left), $P_\mathrm{d} = 50$ s (top right), $P_\mathrm{d} = 100$ s (bottom left) and $P_\mathrm{d} = 200$ s (bottom right).

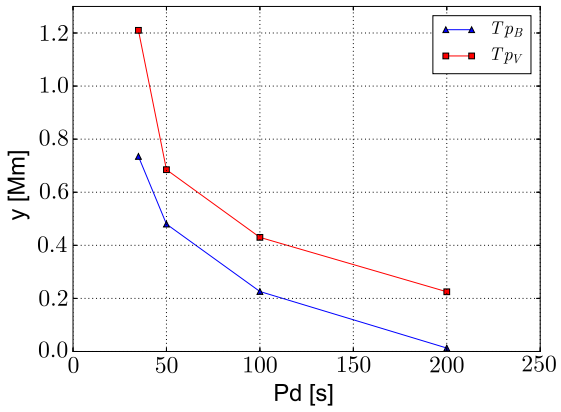

Figure 9 The vertical location of the turning point for B_θ (triangles) and V_θ (squares) *vs.* driving period P_d.

c) This different behavior of the two wave variables can be explained by the fact that the variables for Alfvén waves have different turning-point frequencies, and that these frequencies are used to define the cutoff frequency (or period), which sets up the conditions for the wave propagation in the solar atmosphere.
d) The cutoff for Alfvén waves implies that the waves with periods close to the cutoff are being reflected and that interaction between incoming and reflected waves leads to the formation of standing wave patterns.
e) Our numerical and analytical results demonstrate that the Alfvén wave loses its characteristics while traveling in the solar atmosphere because the wave velocity perturbation reaches the solar corona but the wave magnetic field perturbation does not; as a result,

the wave variables do not satisfy equipartition of energy, and thus the Alfvén wave has a different nature in the upper atmospheric layers.

The obtained results extend the previous work of Murawski and Musielak (2010) and Perera, Musielak, and Murawski (2015) to describe torsional Alfvén waves propagating along solar magnetic flux tubes. From a mathematical point of view, the previous and current work is different; our study is mathematically more complex. However, from a physical point of view, there are some differences and similarities between Alfvén waves studied in the previous work and the torsional Alfvén waves investigated here. In particular, the previous work by Musielak, Routh, and Hammer (2007) and Routh, Musielak, and Hammer (2010) was used to obtain the cutoff frequency for torsional Alfvén waves propagating along a thin and non-isothermal solar magnetic flux tube. The approach formally takes into account both $B_{\mathrm{e}r}(r, y)$ and $B_{\mathrm{e}y}(r, y)$, but only within the thin flux tube approximation. Our analytical results in Section 4 show that the turning-point frequencies are the same as those obtained by Murawski and Musielak (2010), who considered regular Alfvén waves propagating along a uniform background magnetic field, but the cutoff wave periods are different. The results presented here clearly show that the wave variables behave differently and that the atmospheric inhomogeneities have stronger effects on the wave magnetic variable than on the wave velocity variable. Again, this result is consistent with the results obtained previously by Murawski and Musielak (2010) and Perera, Musielak, and Murawski (2015). Moreover, we demonstrated that one of the best ways to account for these differences is to use the turning-point frequencies because their values uniquely determine the behavior of each wave variable in the solar atmosphere, and because they are used to define the cutoff frequency (or period) for Alfvén waves. It is also important to emphasize that the different behavior of the Alfvén wave variables in inhomogeneous media leads to violation of the equipartition of the wave kinetic and magnetic energies in Alfvén waves and that this fact clearly distinguishes Alfvén waves propagating in homogeneous and inhomogeneous media.

Acknowledgements The authors would like to express their thanks to the referee for the comments and suggestions that allowed us to significantly improve the original manuscript. This work was supported by the project from Polish National Science Foundation under the grant No. 2014/15/B/ST9/00106 (D. Wójcik, K. Murawski, Z.E. Musielak and P. Konkol), by NSF under the grant AGS 1246074 (Z.E. Musielak and K. Murawski), and by the Alexander von Humboldt Foundation (Z.E. Musielak). Numerical studies have been performed on the LUNAR cluster at Institute of Mathematics of University of M. Curie-Sklodowska in Lublin, Poland.

Disclosure of Potential Conflicts of Interest The authors declare that they have no conflicts of interest.

References

An, C.H., Musielak, Z.E., Moore, R.L., Suess, S.T.: 1989, *Astrophys. J.* **345**, 597. ADS. DOI.

Avrett, E.H., Loeser, R.: 2008, *Astrophys. J. Suppl.*, **175**, 1. ADS. DOI.

Banerjee, D., Hasan, S.S., Christensen-Dalsgaard, J.: 1998, *New Eyes to See Inside the Sun and Stars* **185**, 423. ADS.

Bemporad, A., Abbo, L.: 2012, *Astrophys. J.* **751**, 2. ADS. DOI.

Chmielewski, P., Srivastava, A.K., Murawski, K., Musielak, Z.E.: 2013, *Mon. Not. Roy. Astron. Soc.* **428**, 40. ADS. DOI.
Chmielewski, P., Srivastava, A.K., Murawski, K., Musielak, Z.E.: 2014, *Acta Phys. Pol. A* **125**, 1. ADS.
Cirtain, J.W., *et al.*: 2007, *Science* **318**, 1580. ADS. DOI.
De Pontieu, B., *et al.*: 2007, *Science* **318**, 1574. ADS. DOI.
Dwivedi, B.N., Srivastava, A.K.: 2006, *Solar Phys.* **237**, 1. ADS. DOI.
Dwivedi, B.N., Srivastava, A.K.: 2010, *Curr. Sci.* **98**, 295. ADS.
Hollweg, J.V.: 1990, *MHD Waves on Solar Magnetic Flux Tubes – Tutorial Review*, *Geoph. Monograph Series* **23**, Am. Geophys. Union, Washington. ADS. DOI.
Hollweg, J.V., Isenberg, P.A.: 2007, *J. Geophys. Res.* **112**, A08102. ADS. DOI.
Hollweg, J.V., Jackson, S., Galloway, D.: 1982, *Solar Phys.* **75**, 35. ADS. DOI.
Jelínek, P., Srivastava, A.K., Murawski, K., Kayshap, P., Dwivedi, B.N.: 2015, *Astron. Astrophys.* **581**, A131. ADS. DOI.
Jess, D.B., Mathioudakis, M., Erdélyi, R., Crokett, P.J., Keenan, F.P., Christian, D.J.: 2009, *Science* **323**, 1582. ADS. DOI.
Kudoh, T., Shibata, K.: 1999, *Astrophys. J.* **514**, 493. ADS. DOI.
Low, B.C.: 1985, *Astrophys. J.* **293**, 31. ADS. DOI.
Mignone, A., Bodo, G., Massaglia, S., Matsakos, T., Tesileanu, O., Zanni, C., Ferrari, A.: 2007, *Astrophys. J. Suppl.* **170**, 1. ADS. DOI.
Mignone, A., Zanni, C., Tzeferacos, P., van Straalen, B., Colella, P., Bodo, G.: 2012, *Astrophys. J. Suppl.* **198**, 1. ADS. DOI.
Miyoshi, T., Kusano, K.: 2005, *J. Comput. Phys.* **208**(1), 315. DOI.
Murawski, K., Musielak, Z.E.: 2010, *Astron. Astrophys.* **581**, A37. ADS. DOI.
Murawski, K., Srivastava, A.K., Musielak, Z.E.: 2014, *Astrophys. J.* **788**, 8. ADS. DOI.
Murawski, K., Solov'ev, A., Kraśkiewicz, J., Srivastava, A.K.: 2015a, *Astron. Astrophys.* **576**, A22. ADS. DOI.
Murawski, K., Srivastava, A.K., Musielak, Z.E., Dwivedi, B.N.: 2015b, *Astrophys. J.* **808**, 1. ADS. DOI.
Musielak, Z.E., Moore, R.J.: 1995, *Astrophys. J.* **452**, 434. ADS. DOI.
Musielak, Z.E., Fontenla, J.M., Moore, R.L.: 1992, *Phys. Fluids* **4**, 13. ADS. DOI.
Musielak, Z.E., Musielak, D.E., Mobashi, H.: 2006, *Phys. Rev. E* **73**, 036612.
Musielak, Z.E., Routh, S., Hammer, R.: 2007, *Astrophys. J.* **659**, 650. ADS. DOI.
Nakariakov, V.M., Verwichte, E.: 2005, *Living Rev. Solar Phys.* **2**, 3. ADS. DOI.
Ofman, L., Davila, J.M.: 1995, *J. Geophys. Res.* **100**, A12. ADS. DOI.
Okamoto, T.J., de Pontieu, B.: 2011, *Astrophys. J.* **736**, L24. ADS. DOI.
Okamoto, T.J., *et al.*: 2007, *Science* **318**, 1577. ADS. DOI.
O'Shea, E., Banerjee, D., Doyle, J.G.: 2005, *Astron. Astrophys.* **436**, 2. ADS. DOI.
Perera, H.K., Musielak, Z.E., Murawski, K.: 2015, *Mon. Not. Roy. Astron. Soc.* **450**, 3. ADS. DOI.
Routh, S., Musielak, Z.E., Hammer, R.: 2010, *Astrophys. J.* **709**, 1297. ADS. DOI.
Suzuki, T.K., Inutsuka, S.: 2005, *Astrophys. J. Lett.* **632**, 1. ADS. DOI.
Ulmschneider, P., Zähringer, K., Musielak, Z.E.: 1991, *Astron. Astrophys.* **241**, 625. ADS.
Webb, G.M., McKenzie, J.F., Hu, Q., Zank, G.P.: 2012, *J. Geophys. Res.* **117**, 5229. ADS. DOI.
Zhugzhda, I.D., Locans, V.: 1982, *Solar Phys.* **76**, 77. ADS. DOI.

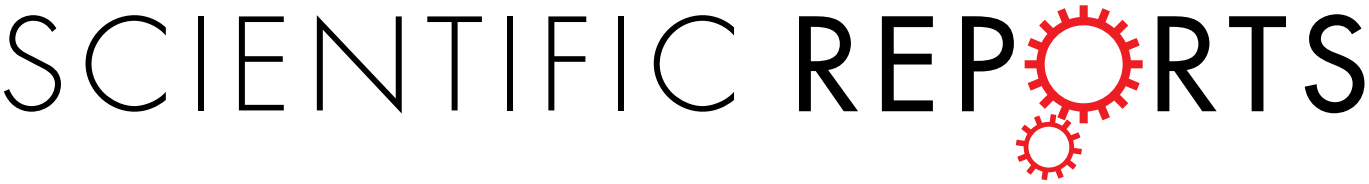

OPEN

High-frequency torsional Alfvén waves as an energy source for coronal heating

Received: 06 September 2016
Accepted: 17 January 2017
Published: 03 March 2017

Abhishek Kumar Srivastava[1], Juie Shetye[2], Krzysztof Murawski[3], John Gerard Doyle[2], Marco Stangalini[4], Eamon Scullion[5], Tom Ray[6], Dariusz Patryk Wójcik[3] & Bhola N. Dwivedi[1]

The existence of the Sun's hot atmosphere and the solar wind acceleration continues to be an outstanding problem in solar-astrophysics. Although magnetohydrodynamic (MHD) modes and dissipation of magnetic energy contribute to heating and the mass cycle of the solar atmosphere, yet direct evidence of such processes often generates debate. Ground-based 1-m Swedish Solar Telescope (SST)/CRISP, Hα 6562.8 Å observations reveal, for the first time, the ubiquitous presence of high frequency (~12–42 mHz) torsional motions in thin spicular-type structures in the chromosphere. We detect numerous oscillating flux tubes on 10 June 2014 between 07:17 UT to 08:08 UT in a quiet-Sun field-of-view of 60″ × 60″ (1″ = 725 km). Stringent numerical model shows that these observations resemble torsional Alfvén waves associated with high frequency drivers which contain a huge amount of energy (~10^5 W m^{-2}) in the chromosphere. Even after partial reflection from the transition region, a significant amount of energy (~10^3 W m^{-2}) is transferred onto the overlying corona. We find that oscillating tubes serve as substantial sources of Alfvén wave generation that provide sufficient Poynting flux not only to heat the corona but also to originate the supersonic solar wind.

Continuous generation of radiation and supersonic wind from the Sun's chromosphere and corona requires a large input of energy (~10^2–10^4 W m^{-2}) to balance these losses[1]. The role of magnetohydrodynamic (MHD) waves and small-scale magnetic reconnection causing nano-flare heating have been explored as primary candidates to energize the solar atmosphere. However, direct evidence of energy sources and their dissipation are not yet fully understood[2–4]. In the era of high resolution space and ground-based observations, it is now revealed that energy and mass transport in the quiescent solar atmosphere are associated with localized static and flowing flux tubes (e.g., network & inter-network magnetic fields, spicules, vortices etc) possessing various plasma and wave processes[5–8]. Here, we observe directly, for the first time, the ubiquitous presence of high frequency (~12–42 mHz) torsional oscillations at apparent surfaces composed of thin spicular-type structures rooted in the quiet-Sun magnetic network. These observations are described by torsional Alfvén waves associated with high frequency drivers transferring ~10^3 W m^{-2} energy into the overlying corona. These oscillating tubes serve as substantial sources of Alfvén wave generation providing sufficient Poynting flux to heat the solar corona and in originating the nascent solar wind.

Quiet-sun magnetic networks are the locations where field lines fan out into the outer atmosphere supporting waves and exotic plasma dynamics[9,10]. The magnetic skeleton of the bundle of fine structured small-scale flux tubes becomes visible when remnants of plasma flows (e.g., spicules, jets, surges) are confined within their boundaries. Various other similar structures are prevalent in the solar chromosphere and well resolved with modern day instruments, e.g., on-disk counterparts of type-II spicules, chromospheric counterparts of the transition region network jets, etc.[11,12]. A tube with its fine structures, each 120–215 km wide, is observed using CRISP on the Swedish Solar Telescope (see yellow and green expanding cylinders in Fig. 1A.1,A.2, respectively). In an integrated view, the tube's projected height and width at the top are respectively ~4 Mm and ~1.5 Mm. Using visualization software, we measure the structure's length, while the width is an average of the values measured at

[1]Department of Physics, Indian Institute of Technology (BHU), Varanasi-221005, India. [2]Armagh Observatory, College Hill, Armagh, BT61 9DG, N. Ireland. [3]Group of Astrophysics, Institute of Physics, UMCS, Lublin, Poland. [4]INAF-OAR National Institute for Astrophysics, 00040, Monte Porzio Catone, RM, Italy. [5]Department of Mathematics & Information Sciences, Northumbria University, Newcastle Upon Tyne, NE1 8ST, UK. [6]Dublin Institute for Advanced Studies, 31 Fitzwilliam Place, Dublin 2, Ireland. Correspondence and requests for materials should be addressed to A.K.S. (email: asrivastava.app@iitbhu.ac.in)

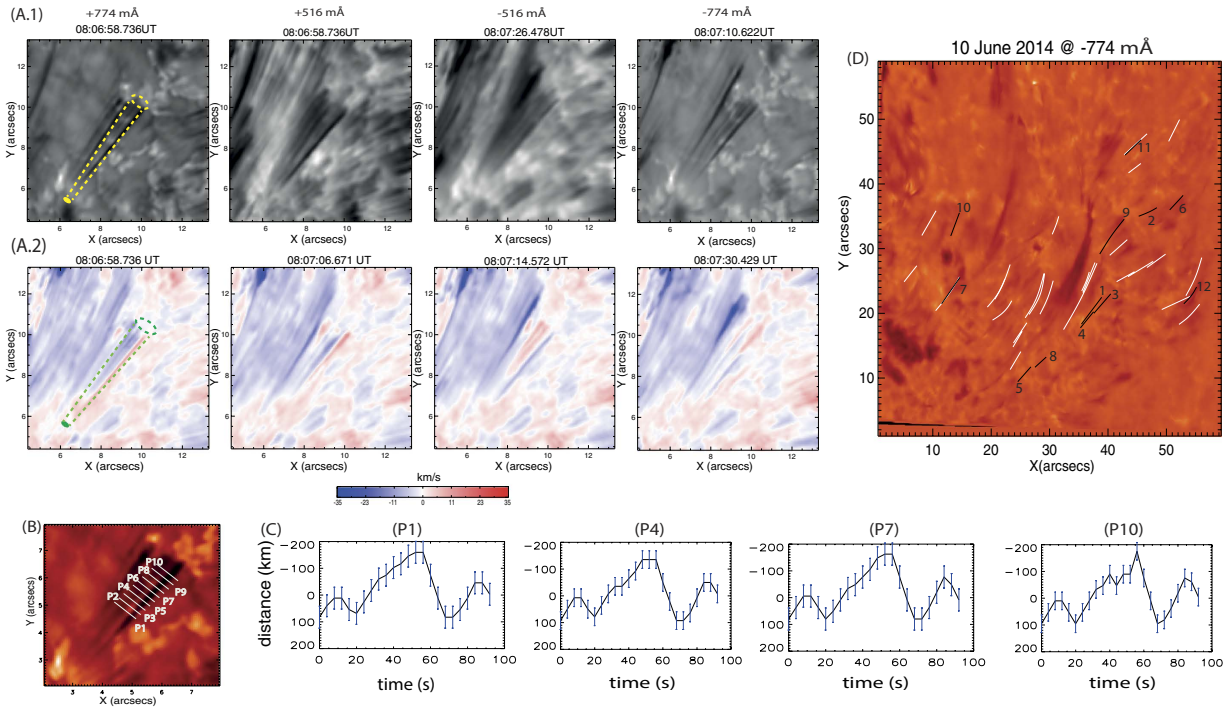

Figure 1. First observations of fine-structured solar magnetic flux tube showing high frequency torsional oscillations (<50 sec). The observations are made using the Crisp Imaging Spectropolarimeter (CRISP) on the ground-based Swedish 1-m Solar Telescope (cadence: 3.9 s with nine line positions across the Hα 6562.8 Å spectral line; image scale is 0.0592" per pixel corresponding to a spatial resolution of roughly 100 km) on 10 June 2014 between 07:17 UT to 08:08 UT. **A.1** (intensity) & **A.2** (Doppler) image sequence show a flux tube made by small-scale spicular-type fine structures anchored in the magnetic network and showing collective torsional motions on an apparent surface (see yellow & green expanding cylinders). (**B**) Displays the slits chosen across one such fine structure on the tube to measure the transverse motions in the projected 2-D plane as shown by fitted profiles in (**C**). (**D**) Displays a context image of SST/CRISP with all such observed flux tubes associated with clear torsional oscillations (black threads). The representative case presented in this figure is indicated by number '1' in the context image.

three locations along its length. The fine structures show collective motions and behave as part of an integrated self-contained magnetic flux tube. This is evident on two clearly visible fine structures showing periodic reversal of velocity sign, i.e., blue on top & red on bottom to red on top & blue on bottom. Thereafter, the previous original condition of velocity signs is restored, i.e., blue on top & red on bottom (Fig. 1A.2). It should be noted that blue and red are the signs of line-of-sight (LOS) components of respectively outward and downward motions, which are tangled with each other. This is the observational signature of torsional oscillations of the fine structured tube over an apparent surface.

RBEs/RREs have three instantaneous chromospheric motions, i.e., up-flows, swaying, and torsional motion[13]. The present observations differ from RBEs /RREs in two aspects: (i) an absence of flows along their length, and (ii) simultaneous red and blue-shifted emission. The adjacent red-blue shift pattern in the chromospheric line was also observed in newly discovered small-scale twisted flux tubes, although the time evolution of the Doppler shift pattern could not be revealed[14].

The method for the solar chromospheric observations and their analyses

As mentioned above this paper invokes solar chromospheric observational data to infer the presence of high-frequency Alfvén waves in the solar atmosphere. The observations are obtained with Crisp Imaging Spectropolarimeter (CRISP) on the ground-based Swedish 1-m Solar Telescope[15,16]. CRISP has a field-of-view of 60" × 60" (1" = 725 km) and a pixel scale of 0.0592". The data is obtained with the cadence of 3.9 s on 10 June 2014 between 07:17 UT to 08:08 UT. The FOV of these observations was centered at (Xc, Yc) = (403", −211"). It contains a pore and quiet-Sun region in the southward side of NOAA AR 12080. The adaptive optics (AO) system was running on SST and used the pore as a tracking point during the acquisition of the data. Nine Hα line positions are sampled in sequence, with eight images being collected at each of −1032, −774, −516, −258, 0 +258, +516, +774, +1032 mÅ w.r.t. the line core at 6562.8 Å before 36 frames were collected at each of −774 mÅ and the line core. After multi-object & multi-frame blind deconvolution (MOMFBD) reconstruction[17], the desired data is obtained with resolution of 0.14". All the observational data (cases) and their details are outlined in Supplementary Table 1 (see in Supplementary Material Information).

The average line profile is defined by taking the average of the FOV and then the line profile is calculated using the pixels along the length of the event. Doppler shifts (Fig. 1A.2) are estimated w.r.t. the line center at

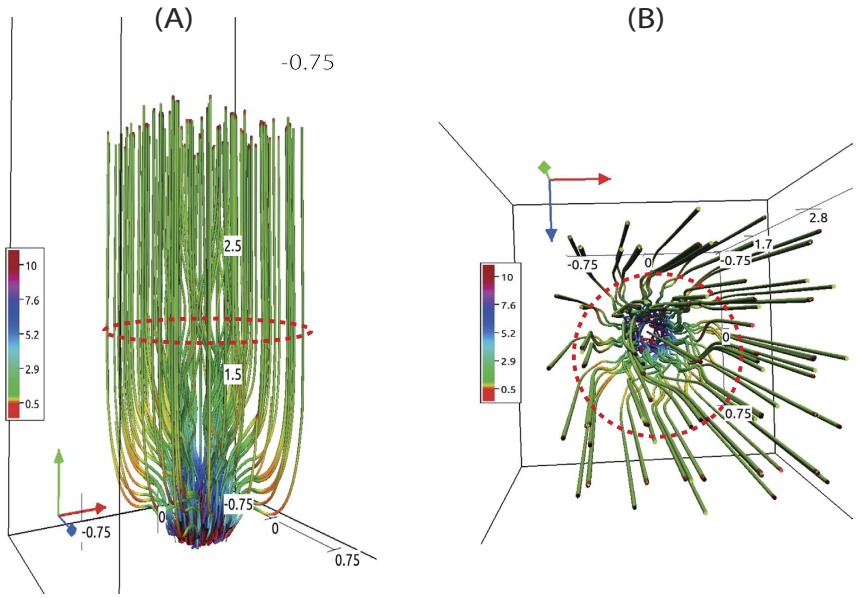

Figure 2. Transverse ('**A**') and Top-down ('**B**') views of a magnetic flux tube with representative magnetic field lines showing torsional motions. The height of the flux tube is 4 Mm, therefore, its upper boundary opens into the inner corona. The solar transition region is located at 2.1 Mm. The magnetic field at the foot-point is 121 Gauss (typical average strength of the quiet-Sun[22]). The tube is fanning out, and the dotted-red shell shows a schematic of an arbitrary apparent surface on which fine-structures may be subject to collective torsional motions.

Hα 6562.8 Å. Therefore, the velocities are estimated from a simple Doppler formula. We do not measure the full-width-at-half-maximum (FWHM) of the spectral-line as our event is observed in the Hα wings, which is sensitive to the temperature, opacity and velocity gradients, in addition to mass motions[18]. Moreover, we limit the spectral resolution by defining the line-positions to gain the required temporal resolution to observe high-frequency oscillations in the observed fast evolving chromospheric features.

First direct observational detection of high-frequency Alfvén waves in the solar chromosphere

The transverse motion of one of these fine-structures on the tube is presented by choosing slits P_1, P_2, ..P_{10} at various spatial positions (Fig. 1'B'). In a 2-D projected plane, it exhibits lateral transversal motions at various heights. In the time-distance plot at various locations (Fig. 1'C'), the position of this dark structure and its displacement in time is estimated by locating the minimum intensity at each temporal step. The spatial position of the minimum intensity at each time step is estimated with sub-pixel accuracy using an FFT cross-correlation technique to disentangle the lateral fluctuations and the bulk motion of the fine structure, and fitting linearly its true transverse motions. Careful investigation shows almost negligible time-lag between the major peak and valley of the transverse motions of this structure at P_1 and P_{10} (Fig. 1'C'). A wavelet analysis of the transverse oscillations shows the presence of significant power associated with ~47 sec period (~21 mHz)[19] (see Supplemental Material Information). Overall, this indicates the direct presence of long-wavelength high-frequency torsional waves that already moved to the top of the tube[20]. The periodic Doppler motions of the flux tube clearly show the torsional oscillations as pronounced on an apparent surface, which is the first direct observation of high-frequency (<50 sec) torsional Alfvén waves in the chromosphere. It should be noted that the first evidence of long-period (126–700 s) torsional Alfvén waves in terms of the oscillation of full-width-at-half-maximum (FWHM) of Hα spectral line had previously been reported above magnetic bright points[6]. The present observations reveal the first evidence of high-frequency torsional waves in numerous fine structured chromospheric flux-tubes (see Supplementary Table 1 in Supplementary Material Information) at larger scales along with more complete energy estimates using a stringent numerical model.

Direct observations of such high frequency torsional oscillations of the fine structured flux tubes in the chromosphere are difficult due to opacity, ongoing heating and cooling processes, and shallowness of the atmosphere[21]. Moreover, this requires high spatial and temporal resolution observations, which were made in the present case by SST/CRISP[16,17] at various line positions around Hα 6562.8 Å. We observe twelve such cases of high frequency torsional oscillations on fine structured tubes. Their details and properties are given in Supplementary Table 1.

The method for the stringent 3-D numerical simulation of high-frequency Alfvén waves

A physical model of such localized solar structures, subject to the torsional oscillations (Fig. 1), is made by a simple but realistic magnetic flux tube using the FLASH code (Fig. 2). The model is an axis-symmetric tube rooted

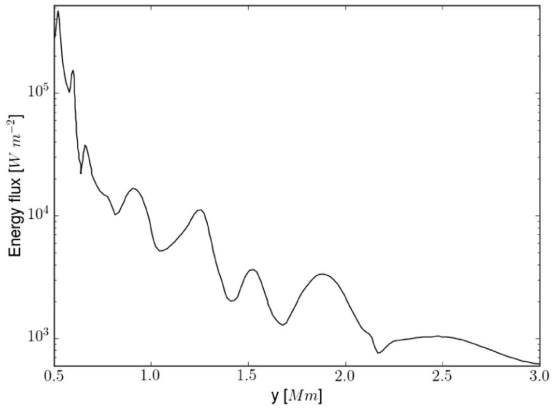

Figure 3. The energy flux of high-frequency torsional Alfvén waves along the tube. The wave has adequate energy of ~10^4 W m^{-2} to heat the solar chromosphere, which is partially transported into the corona (~10^3 W m^{-2}). The energy flux is estimated by averaging it over an area of the tube (-0.3 Mm $<$ x $<$ $+0.3$ Mm) around its central axis at each height.

at the solar photosphere ($B_o = 121$ G)[22], gravitationally stratified, and determined by realistic temperature distribution[23]. For the sake of simplicity, we model only the dynamics of a single enveloping tube similar in size to the observed fine structured flux tube. A concise description of 3-D magnetohydrodynamic (MHD) equations, initial conditions of the plasma and realistic magnetic field as well as their equilibrium in a gravitationally stratified tube, and numerical method and setup, are outlined in the literature[23–26].

The flux tube, where magnetic and gas pressure are initially balanced keeping it in non-force free equilibrium, is then subjected to a perturbation in the azimuthal component of velocity by a periodic high-frequency driver. The form of velocity perturbation is given as,

$$V_\theta = A_V \frac{r}{w} \exp\left[-\frac{r^2 + (y - y_0)^2}{w^2}\right] \sin\left(\frac{2\pi}{P_d} t\right) \quad (1)$$

where A_v is the amplitude of the pulse, $y_0 = 500$ km its vertical position, and $w = 300$ km its width. A_v is set to 150 km s^{-1}, which results in an effective maximum velocity of about 2.4 km s^{-1}. The period of the driver (P_d) is taken as 50 s with wave perturbations generated at the top of the photosphere.

In order to solve the 3-D MHD equations of the model[23] numerically, we use the FLASH code[25,26] with the third-order un-split Roe Riemann solver and the minmod slope limiter, as well as adaptive mesh refinement (AMR). We set the simulation box as (1.5, 1.5, 18) Mm^3, and fix in time all plasma quantities to their equilibrium values at all six boundary surfaces. We use a static, non-uniform grid with a minimum (maximum) level of refinement set to 2 (5). Numerical results are displayed in Figs 2 and 3.

Evolution of high-frequency Alfvén waves carrying substantial energy

The horizontal convective motions present in the quiet-Sun photosphere can generate Alfvén waves carrying significant amount of energy to heat the corona[27,28]. Such motions at the photosphere and chromosphere correlate well at the spatial scales of super-granular cells, therefore, indicating the transfer of energy seen as velocity fluctuations even up to the chromosphere[29]. Exclusively observed oscillating chromospheric flux tubes are visible even in the blue-wing (-774 mÅ) of Hα 6562.8 Å, which may form at least 200 km above the photosphere[30]. This indicates that the origin of transverse perturbations is somewhere at the top of the photosphere either by the transfer of gigantic velocity fluctuations or by impulsive magnetic reconnection[31–33]. Such impulses result in an azimuthal velocity perturbations (Equation 1) to excite the torsional Alfvén waves in the fine structured flux tubes.

Energy flux ($W = 0.5\,\rho\, V_A\, V_\theta^2$ in W m^{-2}) is calculated using the estimated density (ρ), wave velocity amplitude (V_θ), and local Alfvén velocity (V_A) with height averaged over the horizontal spatial scales in the modeled flux-tube (-0.3 Mm $<$ x $<$ $+0.3$ Mm) by considering the tube as a whole. Therefore, the resultant velocity amplitude and thus derived energy flux at each height signify the net contribution of Alfvén waves excited in the tube. Energy flux oscillations result from the periodic driver which varies in time with the period, and its spatial averaging also contributes to the oscillations. As the energy flux is determined by V_θ^2, its averaging does not lead to a zero in the energy flux. The flux tube at its equilibrium is radially inhomogeneous. Therefore, Alfvén waves and their energy estimates weakly depend on a magnitude of equilibrium magnetic field. For a stronger magnetic field, the Alfvén speed may attain a larger value but it has little effect on the energy flux which depends on the equilibrium mass density and V_θ^2. The high-frequency Alfvén waves carry ~10^4 W m^{-2} energy in the chromosphere, and fulfill the huge requirement of energy there[34]. After partial reflection from the solar transition region, it still contains enough energy (~10^3 W m^{-2}) to compensate the inner coronal energy losses[1] (Fig. 3). This very basic analysis shows that the observed high-frequency torsional Alfvén waves can act as a substantial source to channel sufficient energy to heat the corona. Velocity fluctuations related to these Alfvén waves penetrate into the corona carrying associated energy (Fig. 3), while magnetic field perturbations are mostly concentrated up to the

upper transition region and inner corona (Fig. 2). These structures are ubiquitous in the quiet-Sun chromosphere (Fig. 1). For the stronger magnetic field at the tube's foot-point, the nature of the wave is the same. However, it may pump slightly more energy to the overlying atmosphere[20].

The structuring of the plasma and magnetic field along the observed flux tube may lead to an amplitude variation as is evident in the standard-deviation (SDEV) measurement of the time-distance profile of transverse motions at its different locations (see Supplementary Material Information). This amplitude variation may further introduce a variation in energy flux. This is in qualitative agreement with the calculation of energy flux at different heights of the modeled flux tube (Fig. 3).

During MHD wave evolution in realistic model flux tube coupling the solar photosphere to the corona, various other important physical processes are evident. There is a generation of vertical plasma flows due to pondermotive forces under non-linear conditions. However, these up and down flows of the plasma are mostly trapped in the solar atmosphere and do not launch the solar wind unless the escape velocity is achieved. Another effect is the evolution of multiple concentric magnetic shells within the tube where Alfvén perturbations are pronounced with time creating complex velocity fields. Essentially, the velocity perturbations over different magnetic shells (or surfaces) are not in phase, which is a fundamental property of Alfvén waves in stratified inhomogeneous tubes.

The frequency range of the observed torsional Alfvén waves in various magnetic flux tubes lies between 12–42 mHz (Supplementary Table 1). Eight of these observed structures, associated with strong amplitudes, exhibit one full period of the traversal oscillations, while three show the half-period of the oscillations and disappear quickly (Fig. 1 and Supplementary Table 1). Our theoretical model depicts the wave propagation in Eulerian formalism and shows a clear evolution of the torsional oscillations. The observed chromospheric structures are the fast evolving features carrying similar high-frequency oscillations, but they fade away quickly. The major event presented in the paper (Fig. 1) exhibits almost two cycles of the oscillations vis-à-vis matching with the model. However, many of these incompressible waves, having large-amplitude, may undergo mode-conversion to compressible waves in a non-linear regime in the presence of a pondermotive force due to total magnetic pressure variations and may dissipate their energy quickly[35]. The fading of the oscillatory tubes may also be due to the strong velocity gradient at their edges and thereafter evolution of the Kelvin-Helmholtz instability[36]. It should be noted that these fast waves also seem to be associated with long wavelengths compared to the length of the tube itself. This is the reason why every tube shows torsional motion almost as a whole. These high-frequency torsional Alfvén waves are detected directly in such localized small-scale flux tubes.

Strongly homogeneous tubes in the chromosphere may be subject to coupling of the kink modes to the surface Alfvén waves. However, this may take a longer time compared to the dynamics of the observed structures here, while a discontinuity layer in the tube's boundary is established with sufficient thickness[37,38]. Keeping in view the complexity (e.g., twist) in flux tube, the axis-symmetric sausage mode signature may also contribute to the Doppler velocity variations[39]. But, there is no evidence of an initial twist in the observed fine-structured tubes. Therefore, we rule out these possibilities in the present context. In conclusion, the SST/CRISP field-of-view of 60" × 60" (1" = 725 km) detects at least 40 oscillating flux tubes in the chromosphere. They seem to be ubiquitous in various regions of the Sun's chromosphere[40] indicating the presence of substantial energy sources beneath the corona. Torsional waves through many of these flux tubes ('12') carry sufficient energy up to the TR/inner corona, which may be potentially used in heating the localized atmosphere and energizing the supersonic wind by its dissipation due to energy cascade at smaller spatial scales[41]. These oscillating chromospheric structures will likely be detected in abundant measure with ultra high resolution observations with the next generation solar telescopes, e.g., 2-m National Large Indian Telescope (NLST), 4-m DKIST, European Solar Telescope (EST), 8-m Chinese Giant Telescope etc, and new information will further enlighten our understanding on their dynamics and potential role in the solar atmosphere[42–44].

References

1. Withbroe, G. L. & Noyes, R. W. Mass and energy flow in the solar chromosphere and corona. *Ann. Rev. Astron. Astrophys*. **15,** 363–387 (1977).
2. McIntosh, S. *et al.* Alfvénic waves with sufficient energy to power the quiet solar corona and fast solar wind. *Nature*. **475,** 477–480 (2011).
3. Cirtain, J. *et al.* Evidence for Alfvén waves in solar X-ray jets. *Science*. **318,** 1580–1582 (2007).
4. Parker, E. Nanoflares and the solar X-ray corona. *Astrophys. J*. **330,** 474–479 (1988).
5. Wedemeyer-Bohm, S. *et al.* Magnetic tornadoes as energy channels into the solar corona. *Nature*. **486,** 505–508 (2012).
6. Jess, D. *et al.* Alfvén waves in the lower solar atmosphere. *Science*. **323,** 1582–1585 (2009).
7. De Pontieu, B. *et al.* Chromospheric Alfvénic waves strong enough to power the solar wind. *Science*. **318,** 1574–1577 (2007).
8. De Pontieu, B., Erdélyi, R. & James, S. P. Solar chromospheric spicules from the leakage of photospheric oscillations and flows. *Nature*. **430,** 536–539 (2004).
9. Hasan, S. S. & Kalkofen, W. Dynamics of the solar magnetic network. II. Heating the magnetized chromosphere. *Astrophys. J.* **680,** 1542–1552 (2008).
10. De Pontieu, B. *et al.* The origins of hot plasma in the solar corona. *Science*. **331,** 55–58 (2011).
11. Rouppe van der Voort, L., Leenaarts, J., de Pontieu, B., Carlsson, M. & Vissers, G. On-disk counterparts of type II spicules in the Ca II 854.2 nm and Hα lines. *Astrophys. J.* **705,** 272–284 (2009).
12. Tian, H. *et al.* Prevalence of small-scale jets from the networks of the solar transition region and chromosphere. *Science*. **346(6207),** id. 1255711, doi: 10.1126/science.1255711 (2014).
13. Sekse, D. H., Rouppe Van der Voort, L., De Pontieu, B. D. & Scullion, E. Interplay of three kinds of motion in the disk counterpart of type II spicules: Upflows, tranvsersal and torsional motions. *Astrophys. J*. **769,** article id. 44, 11 pp. doi: 10.1088/0004-637X/769/1/44 (2013).
14. De Pontieu, B. *et al.* On the prevalence of small-scale twist in the solar chromosphere and transition region. *Science*. **346(6207),** id. 1255732, doi: 10.1126/science.1255732 (2014).
15. Scharmer, G. B., Bjelksjo, K., Korhonen, T. K., Lindberg, B. & Petterson, B. The 1-meter Swedish solar telescope. *SPIE*. **4853,** 341–350 (2003).

16. Scharmer, G. B. *et al.* CRISP spectropolarimetric imaging of penumbral fine structure. *Astrophys. J.* **689,** article id. L69, doi: 10.1086/595744 (2008).
17. van Noort, Michiel, Rouppe van der Voort, Luc, Löfdahl & Mats, G. Solar image restoration by use of Multi-frame Blind Deconvolution with multiple objects and phase diversity. *Sol. Phys.* **228,** 191–215 (2005).
18. Leenaarts, J., Carlsson, M. & Rouppe van der Voort, L. The formation of the Hα line in the solar chromosphere. *Astrophys. J.* **749,** article id.136, 14 pp, doi: 10.1088/0004-637X/749/2/136 (2012).
19. Torrence, C. & Compo, G. P. A practical guide to wavelet analysis. *Bull. American Met. Soc.* **79,** 61–78 (1998).
20. Zaqarashvili, T. V. & Erdélyi, R. Oscillations and waves in solar spicules. *Space Sci. Rev.* **149,** 355–388 (2009).
21. Carlsson, M. & Leenaarts, J. Approximations for radiative cooling and heating in the solar chromosphere. *Astron. Astrophys.* **539,** article id. A39, 10 pp, doi: 10.1051/0004-6361/201118366 (2012).
22. Domínguez Cerdeña, I., Sánchez Almeida, J. & Kneer, F. The distribution of quiet Sun magnetic field strengths from 0 to 1800 G. *Astrophys. J.* **636,** 496–509 (2006).
23. Murawski, K., Solov'ev, A., Musielak, Z. E., Srivastava, A. K. & Kraśkiewicz, J. Torsional Alfvén waves in solar magnetic flux tubes of axial symmetry. *Astron Astrophys.* **577,** article id A126, 11 pp, doi: 10.1051/0004-6361/201424545 (2015).
24. Lee, D. J. A solution accurate, efficient and stable unsplit staggered mesh scheme for three dimensional magnetohydrodynamics. *Comp. Phys.* **243,** 269–292 (2013).
25. Fryxell, B. *et al.* FLASH: An adaptive mesh hydrodynamics code for modeling astrophysical thermonuclear flashes. *Astrophys J.* **131** (suppl.), 273–334 (2000).
26. Lee, D. & Deane, A. E. An unsplit staggered mesh scheme for multidimensional magnetohydrodynamics. *J. Comp. Phys.* **228,** 952–975 (2009).
27. Uchida, Y. & Kaburaki, O. Excess heating of corona and chromosphere above magnetic regions by non-linear Alfvén Waves. *Sol. Phys.* **35,** 451–466 (1974).
28. Matsumoto, T. & Shibata, K. Nonlinear propagation of Alfvén waves driven by observed photospheric motions: Application to the coronal heating and spicule formation. *Astrophys. J.* **710,** 1857–1867 (2010).
29. Tian, H., Potts, H. E., Marsch, E., Attie, R. & He, J.-S. Horizontal supergranule-scale motions inferred from TRACE ultraviolet observations of the chromosphere. *Astron. Astrophys.* **519,** article id A58, 10 pp, doi: 10.1051/0004-6361/200913254 (2010).
30. Vernazza, J. E., Avrett, E. H. & Loeser, R. Structure of the solar chromosphere. III - Models of the EUV brightness components of the quiet-sun. *Astrophys. J.* **45** (suppl.), 635–725 (1981).
31. Morton, R. J., Verth, G., Fedun, V., Shelyag, S. & Erdélyi, R. Evidence for the photospheric excitation of incompressible chromospheric waves. *Astrophys. J.* **768,** article id. 17, 11 pp, doi: 10.1088/0004-637X/768/1/17 (2013).
32. Murawski, K., Srivastava, A. K., Musielak, Z. E. & Dwivedi, B. N. Multi-shell magnetic twisters as a new mechanism for coronal heating and solar wind acceleration. *Astrophys. J.* **808,** article id. 5, 9 pp, doi: 10.1088/0004-637X/808/1/5 (2015).
33. Mathioudakis, M., Jess, D. B. & Erdélyi, R. Alfvén Waves in the solar atmosphere. From theory to observations. *Space Sci. Rev.* **175,** 1–27 (2013).
34. Grant, S. D. T. *et al.* Wave damping observed in upwardly propagating sausage-mode oscillations contained within a magnetic pore. *Astrophys. J.* **806,** article id. 132, 14 pp, doi: 10.1088/0004-637X/806/1/132 (2015).
35. Antolin, P. & Shibata, K. The role of torsional Alfvén waves in coronal heating. *Astrophys. J.* **712,** 494–510 (2010).
36. Kuridze, D. *et al.* The dynamics of rapid redshifted and blueshifted excursions in the solar Hα line. *Astrophys. J.* **802,** article id. 26, 8 pp, doi: 10.1088/0004-637X/802/1/26 (2015).
37. Goossens, M. *et al.* Surface Alfvén waves in solar flux tubes. *Astrophys. J.* **753,** article id. 111, 12 pp, doi: 10.1088/0004-637X/753/2/111 (2012).
38. Srivastava, A. K. & Goossens, M. X6.9-class flare-induced vertical kink oscillations in a large-scale plasma curtain as observed by the Solar Dynamics Observatory/Atmospheric Imaging Assembly. *Astrophys. J.* **777,** article id. 17, 9 pp, doi: 10.1088/0004-637X/777/1/17 (2013).
39. Giagkiozis, I., Fedun, V., Erdélyi, R. & Verth, G. Axissymmetric modes in magnetic fluxtubes with internal and external magnetic twists. *Astrophys. J.* **810,** article id. 53, 12 pp, doi: 10.1088/0004-637X/810/1/53 (2015).
40. Shetye, J. *et al.* High-cadence observations of spicular-type events on the Sun. *Astron. Astrophys.* **589,** article id A3, 15 pp, doi: 10.1051/0004-6361/201527505 (2016).
41. Cranmer, S., van Ballegooijen, A. & Edgar, R. Self-consistent coronal heating and solar wind acceleration from anisotropic magnetohydrodynamic turbulence. *Astrophys. J.* **171** (suppl.), 520–551 (2007).
42. Hasan, S. S. The Indian national large solar telescope (NLST). *IAU.* **264,** 499–504 (2009).
43. Rimmele, T., McMullin, J., Warner, M. *et al.* Daniel K. Inouye Solar Telescope: Overview and status. *IAU General Assembly Meeting.* **29,** id.2255176 (2015).
44. Deng, Y. Y. Introduction to the Chinese Giant Solar Telescope. *ASI Conference Series.* **2,** 31–36 (2011).

Acknowledgements

A.K.S. & B.N.D. acknowledge the RESPOND-ISRO (DOS/PAOGIA205-16/130/602) project. A.K.S. acknowledges the SERB-DST project (YSS/2015/000621) grant, the Advanced Solar Computational & Analyses Laboratory (ASCAL), and infrastructural facilities at the Department of Physics, IIT (BHU) to pursue this research. Armagh Observatory is grant-aided by the N.Ireland Department for Communities. The authors acknowledge the DJEI/DES/SFI/HEA Irish Centre for High-End Computing (ICHEC) for the provision of computing facilities and support. We also like to thank STFC for a studentship and PATT T&S and the Solarnet project which is supported by the European Commission's FP7 Capacities Programme under Grant Agreement number 312495 for T&S. J.S. is funded by the Leverhulme Trust. M.S. aknowledges support by the "Progetti di ricerca INAF di Rilevante Interesse Nazionale" (PRIN-INAF 2014) and PRIN MIUR 2012 (prot. 2012P2HRCR) entitled "Il sole attivoed i suoi effetti sul clima dello spazio e della terra" grants, funded by the Italian National Institute for Astrophysics (INAF) and Ministry of Education, Universities and Research (MIUR), respectively. KM's and DW's work was done in the frame-work of the project from the National Science Centre, Poland Grant No: 2014/15/B/ST9/00106. The Swedish 1-m Solar Telescope is operated on the island of La Palma by the Institute for Solar Physics of Stockholm University in the Spanish Observatorio del Roque de los Muchachos of the Instituto de Astrofsica de Canarias.

Author Contributions

A.K.S. leads the project by defining the novel science case and writing the paper. J.S. has prepared the observational data, while K.M. & D.W. provided the numerical runs based on science case. J.G.D. and M.S. have contributed on SST data and its most plausible connection with the numerical model. E.S. & T.R. have provided the SST/CRISP observations. J.G.D. & B.N.D. have an overview on the write-up and consistency on presenting the scientific results.

Additional Information

Supplementary information accompanies this paper at http://www.nature.com/srep

Competing financial interests: The authors declare no competing financial interests.

How to cite this article: Srivastava, A. K. *et al.* High-frequency torsional Alfvén waves as an energy source for coronal heating. *Sci. Rep.* **7**, 43147; doi: 10.1038/srep43147 (2017).

Publisher's note: Springer Nature remains neutral with regard to jurisdictional claims in published maps and institutional affiliations.

The Astrophysical Journal, 849:78 (9pp), 2017 November 10 https://doi.org/10.3847/1538-4357/aa8ea1

Two-fluid Numerical Simulations of Solar Spicules

Błażej Kuźma[1], Kris Murawski[1], Pradeep Kayshap[1], Darek Wójcik[1], Abhishek Kumar Srivastava[2], and Bhola N. Dwivedi[2]
[1] Group of Astrophysics, University of Maria Curie-Skłodowska, ul. Radziszewskiego 10, 20-031 Lublin, Poland; blazejkuzma1@gmail.com
[2] Department of Physics, Indian Institute of Technology (BHU), Varanasi-221005, India
Received 2017 May 15; revised 2017 September 18; accepted 2017 September 19; published 2017 November 3

Abstract

We aim to study the formation and evolution of solar spicules by means of numerical simulations of the solar atmosphere. With the use of newly developed JOANNA code, we numerically solve two-fluid (for ions + electrons and neutrals) equations in 2D Cartesian geometry. We follow the evolution of a spicule triggered by the time-dependent signal in ion and neutral components of gas pressure launched in the upper chromosphere. We use the potential magnetic field, which evolves self-consistently, but mainly plays a passive role in the dynamics. Our numerical results reveal that the signal is steepened into a shock that propagates upward into the corona. The chromospheric cold and dense plasma lags behind this shock and rises into the corona with a mean speed of 20–25 km s^{-1}. The formed spicule exhibits the upflow/downfall of plasma during its total lifetime of around 3–4 minutes, and it follows the typical characteristics of a classical spicule, which is modeled by magnetohydrodynamics. The simulated spicule consists of a dense and cold core that is dominated by neutrals. The general dynamics of ion and neutral spicules are very similar to each other. Minor differences in those dynamics result in different widths of both spicules with increasing rarefaction of the ion spicule in time.

Key words: magnetohydrodynamics (MHD) – methods: numerical – Sun: activity – Sun: corona – Sun: transition region

1. Introduction

Spicules are thin jet-like structures, which dominate in the lower layers of the solar corona. They are best seen at the solar limb in strong chromospheric and transition-region (TR) spectral lines such as Hα, Ca II H & K, Mg II H & K, C II, and Si IV lines (e.g., Roberts 1945; Matsuno & Hirayama 1988; Nishikawa 1988; Suematsu et al. 1995; De Pontieu et al. 2007b; Suematsu et al. 2008; Sterling et al. 2010; Madjarska et al. 2011; Pereira et al. 2012, 2014, 2016; Tsiropoula et al. 2012; Skogsrud et al. 2014, 2015; Rouppe van der Voort et al. 2015; Beck et al. 2016). Spicule observations have been carried out for about 130 years since they were first reported in 1877 (Secchi 1887). Therefore, a huge amount of observational literature about spicules is available, which is dedicated to understanding their basic properties (mass density, temperature, velocity, and magnetic field), initiation mechanisms, waves, and oscillations. These crucial aspects are very well documented in various review papers, i.e., basic properties by Beckers (1968, 1972) and Suematsu (1998), initiation mechanisms by Sterling (2000), and oscillations and waves by Zaqarashvili & Erdélyi (2009).

High-resolution observational data leads to continuous improvement of our knowledge about the spicules. Based on their properties, De Pontieu et al. (2007b) classified the spicules into two different categories (i.e., Types I and II). Type I spicules exhibit a slower velocity (15–40 km s^{-1}) and longer lifetime (3–10 minutes) compared to the velocity (30–110 km s^{-1}) and lifetime (50–150 s) of Type II spicules. Type I spicules reveal the rise and fall of plasma during its total life, while type II spicules fade from the view and the downfall of plasma is not visible (e.g., De Pontieu et al. 2007b; Pereira et al. 2012). Sterling & Hollweg (1984) have proposed that the heating rate is sufficient to heat the spicules to temperatures at which the hydrogen is fully ionized. Therefore, H-α spicules (cool temperature) may evolve into EUV spicules (hot temperature). Later, this thermal evolution (i.e., fading of the spicules from cool filters and appears in the hot filters) of the spicules was investigated in various other works as well (e.g., De Pontieu et al. 2009; McIntosh & De Pontieu 2009; McIntosh et al. 2010; Tian et al. 2011). Recently, Pereira et al. (2014) have reported the traces of spicules in the hot temperature filter after fading from the cool temperature filter.

The origin and excitation mechanisms of spicules are one of the most crucial issues of solar physics, which has been continuously investigated using observations as well as numerical simulations. Pulses in velocity or gas pressure, Alfvén waves, and p-modes are the three broad categories of drivers that may be responsible for the formation of spicules. Main physical process within the velocity/gas pressure pulse model is the formation of a shock front, which results in a generation of the spicule in the lower corona. Such a rebound shock model was developed by Hollweg (1982) who used a gas pressure pulse in one-dimensional (1D) MHD equations for the formation of a spicule. In another approach, Suematsu et al. (1982) performed a numerical experiment using a velocity pulse instead of a gas pressure pulse. Later, this rebound shock model was improved by including radiation and heat conduction in the model (e.g., Sterling & Mariska 1990; Cheng 1992; Sterling et al. 1993; Heggland et al. 2007; Kuźma et al. 2017). Recently, Sterling & Moore (2016) have reported that the microfilament-eruptions can be a potential candidate for the generation of spicules. Murawski & Zaqarashvili (2010) performed 2D numerical simulations with a velocity pulse to produce the spicule. Multistructural, bidirectional flows and 3–5 minute periodicity in the occurrence of spicules were successfully reproduced in that numerical experiment. This model was extended into its 2D counterpart with the inclusion of the nonadiabatic effects (Kuźma et al. 2017). A general conclusion drawn from the performed simulations was that the shocks play an important role in the dynamics and thermodynamics of impulsively generated spicules and the other

nonadiabatic terms (i.e., thermal conduction and radiative cooling terms) produce minor effects on the dynamics/thermodynamics of the spicule.

In the second category, it was proposed that the nonlinear coupling between Alfvén waves and slow magnetoacoustic shocks can lift up the TR, which produces the spicule (Hollweg et al. 1982). This idea for the generation of spicules was further investigated by Cranmer & Woolsey (2015, 2016). They have found that the magnetohydrodynamic turbulence is a potential driver for spicules. It was also reported that the random nonlinear Alfvén pulses may reproduce the spicules (Kudoh & Shibata 1999). More interestingly, the damping of Alfvén waves due to ion-neutral collisions can be an efficient mechanism for the formation of spicules in the solar atmosphere (Haerendel 1992; James et al. 2003).

In the third category, De Pontieu et al. (2004) showed that p-modes are the potential candidates for triggering spicules in the solar atmosphere, which was further investigated in various other works (e.g., Hansteen et al. 2006; De Pontieu et al. 2007a).

The above mentioned main three categories (i.e., gas pressure or velocity pulse, Alfvén waves and p-modes) are not the only mechanisms for the formation of spicules. Indeed, there are various other numerous proposed physical processes responsible for the formation of spicules. Among others, the compression of the plasma sheet by the magnetic field (Hollweg 1972), Joule heating in the current sheet (Hirayama 1992), thermal conduction from the corona (Kopp & Kuperus 1968; Moore & Fung 1972), and buffeting of anchored magnetic flux by granulation can lead to spicules (Roberts 1979). These and various other mechanisms are discussed by Sterling (2000).

Although spicules were discovered a long time ago (Secchi 1887), they are still not fully understood. Therefore, they remain the subject of further investigation. Advanced numerical simulations are an important means to reveal the nature of spicules. However, it is always difficult to implement the real solar conditions in the numerical experiment. Because low layers of the solar atmosphere contain large fraction of neutrals (e.g., Zaqarashvili et al. 2011), two-fluid plasma (i.e., ionized and neutral fluids) approach in the numerical experiment is more suitable than magnetohydrodynamics (MHD) to study the evolution of spicules in the solar atmosphere. This approach is used for the first time in the present numerical simulations of solar spicules. Specifically, we perform 2D numerical simulations of two-fluid equations to produce the spicule using pulses launched initially in vertical components of ion and neutral velocities. The adopted potential magnetic field configuration plays essentially a passive role in the present simulations. The paper is organized as follows. In Section 2, we describe the physical model of the solar atmosphere. Numerical simulations are presented in Section 3. Summary and conclusions are outlined in the last section.

2. Physical Model of the Solar Atmosphere

2.1. Two-fluid Equations

We consider a gravitationally stratified and magnetically confined plasma that consists of two components: ionized fluid (ions + electrons) and neutral fluid (neutrals). This model is governed by the following set of equations (Smith & Sakai 2008):

$$\frac{\partial \varrho_i}{\partial t} + \nabla \cdot (\varrho_i \boldsymbol{V}_i) = -\varrho_i(\alpha_r \varrho_i - \alpha_i \varrho_n), \tag{1}$$

$$\frac{\partial \varrho_n}{\partial t} + \nabla \cdot (\varrho_n \boldsymbol{V}_n) = \varrho_i(\alpha_r \varrho_i - \alpha_i \varrho_n), \tag{2}$$

$$\begin{aligned}\varrho_i\left(\frac{\partial \boldsymbol{V}_i}{\partial t} + (\boldsymbol{V}_i \cdot \nabla)\boldsymbol{V}_i\right) = &-\nabla p_i + \frac{1}{\mu}(\nabla \times \boldsymbol{B}) \times \boldsymbol{B} + \varrho_i \boldsymbol{g} \\ &- \alpha_c \varrho_i \varrho_n (\boldsymbol{V}_i - \boldsymbol{V}_n) \\ &- \varrho_i(\alpha_r \varrho_i \boldsymbol{V}_i - \alpha_i \varrho_n \boldsymbol{V}_n),\end{aligned} \tag{3}$$

$$\begin{aligned}\varrho_n\left(\frac{\partial \boldsymbol{V}_n}{\partial t} + (\boldsymbol{V}_n \cdot \nabla)\boldsymbol{V}_i\right) = &-\nabla p_n + \varrho_n \boldsymbol{g} \\ &+ \alpha_c \varrho_i \varrho_n (\boldsymbol{V}_i - \boldsymbol{V}_n) \\ &+ \varrho_i(\alpha_r \varrho_i \boldsymbol{V}_i - \alpha_i \varrho_n \boldsymbol{V}_n),\end{aligned} \tag{4}$$

$$\begin{aligned}&\frac{\partial p_i}{\partial t} + \boldsymbol{V}_i \cdot \nabla p_i + \gamma p_i \nabla \cdot \boldsymbol{V}_i \\ &\quad = (\gamma - 1)\alpha_c \varrho_i \varrho_n (\boldsymbol{V}_i - \boldsymbol{V}_n) \cdot \boldsymbol{V}_i,\end{aligned} \tag{5}$$

$$\begin{aligned}&\frac{\partial p_n}{\partial t} + \boldsymbol{V}_n \cdot \nabla p_n + \gamma p_n \nabla \cdot \boldsymbol{V}_n \\ &\quad = (\gamma - 1)\alpha_c \varrho_i \varrho_n (\boldsymbol{V}_i - \boldsymbol{V}_n) \cdot \boldsymbol{V}_n,\end{aligned} \tag{6}$$

$$\frac{\partial \boldsymbol{B}}{\partial t} = \nabla \times (\boldsymbol{V} \times \boldsymbol{B}), \nabla \cdot \boldsymbol{B} = 0, \tag{7}$$

where $\varrho_{i,n}$ is the mass density, $p_{i,n}$ the gas pressure, $\boldsymbol{V}_{i,n}$ represents the plasma velocity, $\boldsymbol{B}$ is the magnetic field, α_i is a coefficient of ionization, α_r coefficient of recombination, and α_c coefficient of collisions between particles, subscripts i and n correspond, respectively, to ions and neutrals, $\gamma = 5/3$ is the adiabatic index, and $\boldsymbol{g} = (0, -g, 0)$ is the gravitational acceleration. The value of g is equal to 274 m s^{-2}. For the sake of simplicity, all electron-components are neglected due to the small mass of electrons in relation to ions and neutrals.

2.2. Equilibrium Solar Atmosphere

In a static solar atmosphere, all plasma quantities are time-invariant, which means that $\partial f/\partial t = 0$, where f denotes an equilibrium plasma quantity. Then, from Equations (1)–(7), it follows that for still ions ($\boldsymbol{V}_i = 0$) and neutrals ($\boldsymbol{V}_n = 0$) the Lorentz force (if appropriate) must be balanced by the gravity force and the gas pressure gradient,

$$\frac{1}{\mu}(\nabla \times \boldsymbol{B}) \times \boldsymbol{B} - \nabla p_{i,n} + \varrho_{i,n} \boldsymbol{g} = 0. \tag{8}$$

2.2.1. Current-Free Magnetic Field and the Hydrostatic Atmosphere

A hydrostatic atmosphere for ions corresponds to the force-free ($(\nabla \times \boldsymbol{B}) \times \boldsymbol{B} = 0$) magnetic field with the solenoidal condition ($\nabla \cdot \boldsymbol{B} = 0$) being satisfied. We additionally assume a current-free ($\nabla \times \boldsymbol{B} = 0$) magnetic field whose horizontal B_x, vertical B_y, and transversal B_z components are given as

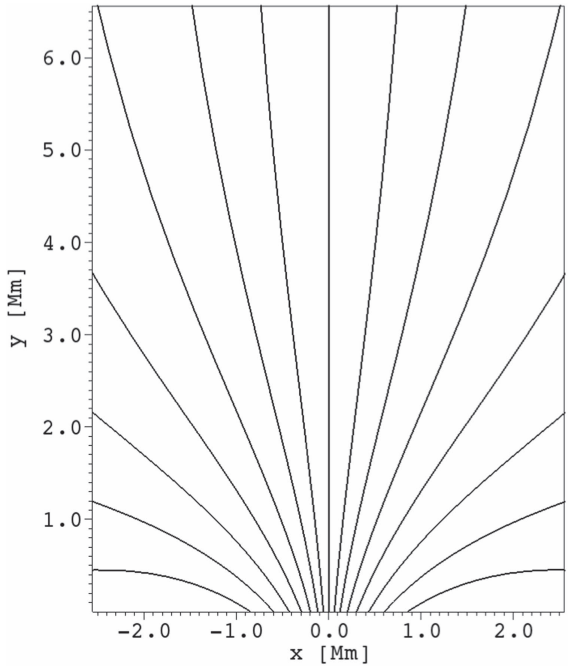

Figure 1. Magnetic field lines at the plasma equilibrium.

(Konkol et al. 2012)

$$B_x(x, y) = \frac{-2Sx(y-a)}{(x^2+(y-a)^2)^2},$$
$$B_y(x, y) = \frac{S(x^2-(y-a)^2)}{(x^2+(y-a)^2)^2} + B_v, \quad B_z(x, y) = 0, \qquad (9)$$

where B_v is a straight vertical magnetic field component, a and S are free parameters corresponding to the vertical location of the singularity in the magnetic field and the magnetic field strength, respectively. We set $B_v = 6$ Gs, $a = -1.5$ Mm and S in such a way that at the reference point ($x_r = 0$, $y_r = 10$) Mm the magnitude of magnetic field $B = 8$ Gs. The corresponding magnetic field lines are displayed in Figure 1. We note that the magnetic field lines become less divergent with height.

For a force-free magnetic field it follows from Equation (8) that at the equilibrium the gas pressure gradients have to be balanced by the gravity force,

$$\nabla p_{i,n} = \varrho_{i,n}\boldsymbol{g}. \qquad (10)$$

With the use of the ideal gas law and the vertical, y-component of Equation (10), we express the hydrostatic gas pressures and mass densities of ions and neutrals as

$$p_{i,n}(y) = p_{0\,i,n}\exp\left(-\int_{y_r}^{y}\frac{dy'}{\Lambda_{i,n}(y')}\right),$$
$$\varrho_{i,n}(y) = \frac{p_{i,n}(y)}{g\Lambda_{i,n}(y)}, \qquad (11)$$

where

$$\Lambda_{i,n}(y) = \frac{k_B T_{i,n}(y)}{mg} \qquad (12)$$

are the pressure scale heights of ions (Λ_i) and neutrals (Λ_n), and $p_{0\,i,n}$ denotes the gas pressure of ions and neutrals at the reference level, $y = y_r = 10$ Mm. In Equation (12), $T_i(y)$ and $T_n(y)$ stand for temperatures of ions and neutrals, respectively. These temperatures are taken from the model of Avrett & Loeser (2008; see Figure 2). Note that for $y > 0.2$ Mm the temperature of ions is higher than the temperature of the neutrals. In the photosphere, which is localized at $0 \leqslant y \leqslant 0.5$ Mm, $T_i(y)$ increases with y until close to the bottom of the chromosphere, specifically for $y \approx 0.7$ Mm, $T_i(y)$ reaches its local maximum of about $1.5 \cdot 10^5$ K. Higher up $T_i(y)$ decreases with height until at the TR it rises abruptly to the coronal value of about 1 MK. The neutral temperature attains its value of about 5 kK within the region of $0 \leqslant y \leqslant 1.75$ Mm. It decreases suddenly right below the TR attaining its minimum of about 150 K and higher up it increases with y reaching its coronal magnitude of about 0.8 MK at $y = 10$ Mm.

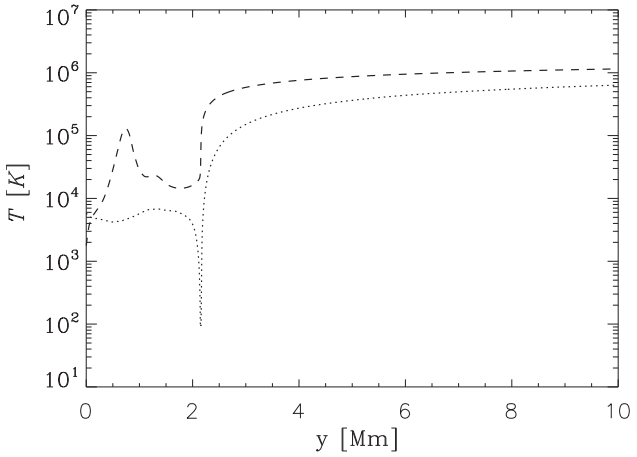

Figure 2. Vertical profiles of hydrostatic temperature of ions (dashed line) and neutrals (dotted line) vs. height y.

As a result of the adopted temperature profiles, the mass densities of ions and neutrals decline with height. The left panel of Figure 3 shows the ratio of the mass density of ions to the mass density of neutrals, $\varrho_i(x, y)/\varrho_n(x, y)$, which result from Equation (11). Note that below the level of $y = 2.1$ Mm the plasma is dominated by neutrals with a minimum of $\varrho_i/\varrho_n \approx 10^{-4}$, while the corona consists of essentially fully ionized plasma; we added a small amount of neutrals in the solar corona due to numerical reasons. We specify the plasma β as the ratio of ion plus neutral gas pressures to magnetic pressure,

$$\beta(y) = \frac{p_i(y) + p_n(y)}{B^2(y)/2\mu}. \qquad (13)$$

The spatial profile of plasma β is illustrated in the right panel of Figure 3. Note that within the displayed region for the coronal plasma, for $y > 2.1$ Mm, and along the entire $x = 0$ line β is smaller than 1.

2.2.2. Perturbations

Initially, at $t = 0$ s, we perturb the model equilibrium by launching, at the bottom boundary, simultaneously time-dependent signals in the ion and neutral gas pressures, which

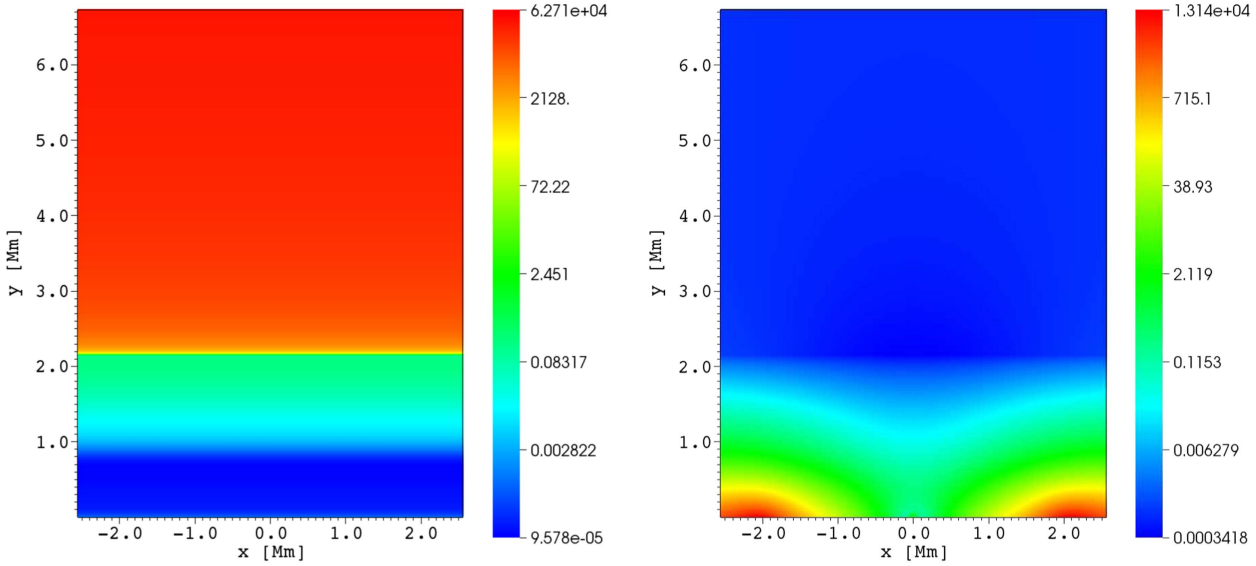

Figure 3. Ratio of the mass density of ions to the mass density of neutrals (left) and plasma beta (right) at the plasma equilibrium.

are expressed as follows:

$$p_{[i,n]}(x, y, t = 0) = p_0\left(1 + A_{p\,[i,n]} \exp\left(-\frac{x^2 + (y - y_0)^2}{w^2}\right) f(t)\right),$$
$$f(t) = \begin{cases} 1 - \exp(-t/\tau), & t \leqslant \tau_{\max} \\ \exp(-(t - \tau_{\max})/\tau), & t > \tau_{\max} \end{cases}. \quad (14)$$

Here y_0 is the vertical position of the signals, w is their width and $A_{p\,i}$, $A_{p\,n}$ their amplitudes. Function $f(t)$ denotes the temporal profile of the gas pressure signal, with τ being its characteristic growth/decay time and $\tau_{\max}$ time at which $f(t)$ reaches its maximum. We set and hold fixed $w = 0.1$ Mm, $\tau = 50$ s, and $\tau_{\max} = 30$ s, while allowing other parameters to vary. For our studies, the signal position, y_0, varies between 1.65 and 1.85 Mm and the amplitude A_p between 6 and 10. This signal position corresponds to a region of $\beta < 1$ (Figure 3, right). As a result of that, slow and fast magnetoacoustic waves are weakly coupled there and the initial pulse triggers slow waves, which propagate essentially along magnetic field lines (e.g., Nakariakov & Verwichte 2005). Unless otherwise stated, the further analysis focuses on the case for $A_p = 8$ and $y_0 = 1.75$ Mm, which corresponds to plasma heated to maximum temperature of 60 kK 1.75 Mm above the photosphere. We have verified that only such strong pulses launched at the top of the chromosphere result in spicules. Lower amplitude pulses excite smaller jets and pulses launched from the lower chromospheric layers lead to horizontally spread jets. The time-dependent signal launched at $y_0 = 1.75$ Mm may mimic a post-reconnection event.

3. Numerical Simulations of Two-fluid Equations

To solve two-fluid equations numerically, we use the JOANNA code (D. Wójcik et al. 2017, in preparation). In our problem, we set the Courant–Friedrichs–Lewy number (Courant et al. 1928) equal to 0.3 and specify the simulation box in (x, y) as $(-1.28, 1.28)$ Mm $\times$ $(1.75, 50.0)$ Mm, where $y = 0$ denotes the bottom of the photosphere. In the numerical simulations we adopt the uniform grid within the region $(-1.28 \leqslant x \leqslant 1.28)$ Mm $\times$ $(1.75 \leqslant y \leqslant 6.87)$ Mm, which is covered by 256×512 grid points. This grid leads to a resolution of 10 km in the main region of the simulation box that is below $y = 6.12$ Mm. Above this region, namely within the rectangle $(-1.28 \leqslant x \leqslant 1.28)$ Mm $\times$ $(6.87 \leqslant y \leqslant 50.0)$ Mm, we implement a stretched grid along the y-direction; this box is divided into 128 cells whose size grows with y. Such a stretched grid plays the role of a sponge as it absorbs incoming signal and minimizes reflections from the top boundary. We impose open boundary conditions for outflowing signal at the side boundaries, while at the top and bottom we fixed all plasma quantities to their equilibrium values.

We launch the gas pressure signals in the chromosphere varying their initial position, y_0, and amplitudes, $A_{p\,i}$ and $A_{p\,n}$, as described in Section 2.2.2. The basic mechanism behind the simulations is that the signals, while launched from the region of $\beta < 1$, essentially split into two, counter-propagating along the equilibrium magnetic field lines' slow magnetoacoustic (slow henceforth) waves; downwardly propagating slow waves decay in time (not shown in the framework of these simulations), while upwardly moving slow waves grow in their amplitudes. The latter convert into a slow shock at higher altitudes due to the decrease of mass density with height. The chromospheric plasma lags behind the shock front to form a contact wave consisting of a spicule. The simple waves structure associated with this phenomenon is described by Kuźma et al. (2017). Note that the signal in $A_{p\,i}$ excites fast magnetoacoustic waves too but they are of low amplitudes as they spread quasi-isotropically in space. The pulse in $A_{p\,n}$ generates neutral acoustic waves (Zaqarashvili et al. 2011).

The top row of Figure 4 shows the spatial profiles of log $(\varrho_i(x, y))$ at three instants of time, which are $t = 70$ s (top left), $t = 210$ s (top middle), and $t = 320$ s (top-right). The gas pressure drivers of Equation (14) operate at the point of $(x = 0, y = y_0 = 1.75)$ Mm, which is located in the chromosphere around 0.35 Mm below the TR, and they reach their maximum at $t = 30$ s. At $t = 70$ s, it is found that the ion shock front is followed by hot plasma, which results from the drivers,

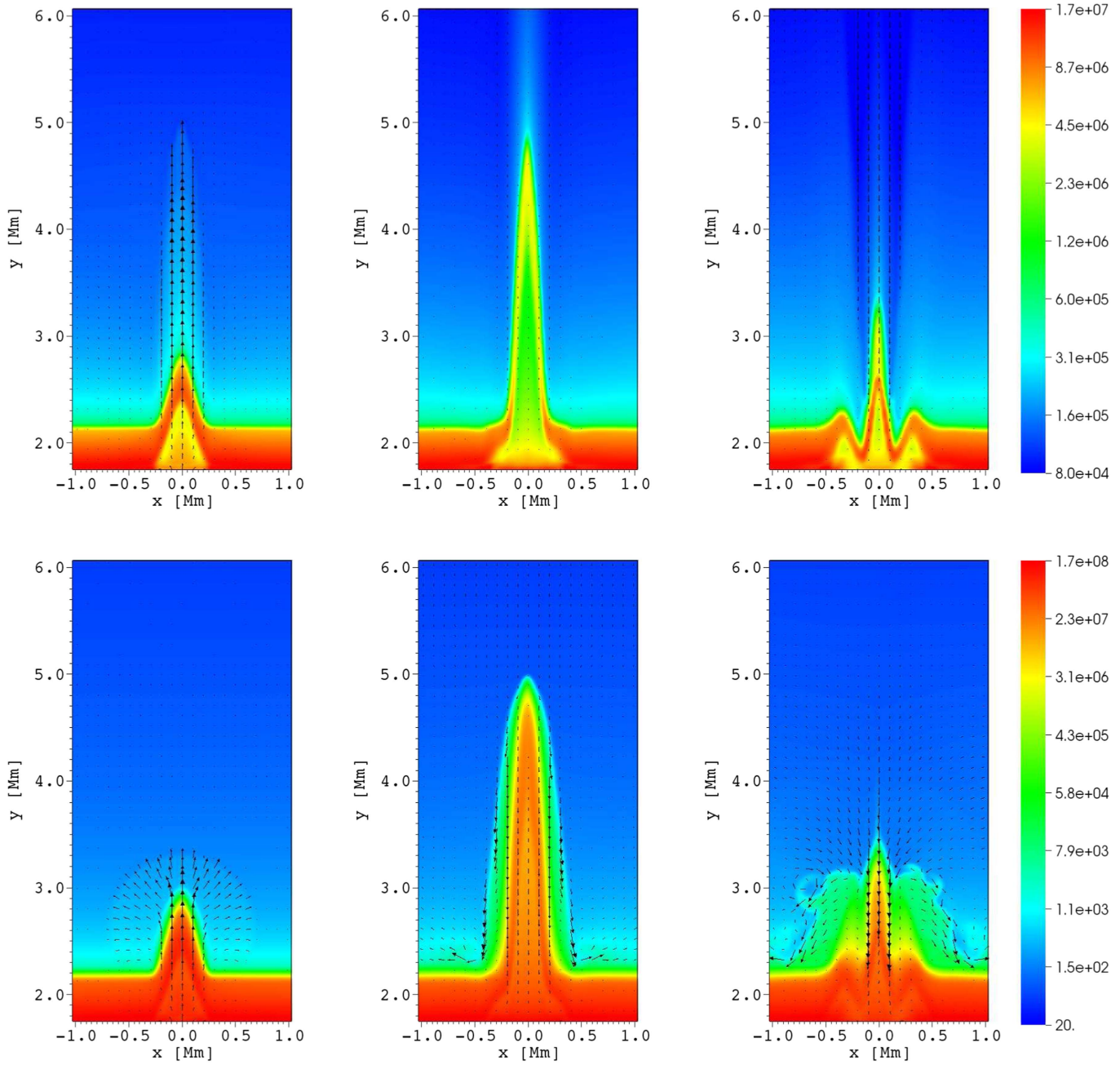

Figure 4. Temporal evolution of $\log(\varrho_i(x, y))$ at $t = 70$ s, $t = 210$ s, and $t = 320$ s (from top left to top right), and $\log(\varrho_n(x, y))$ (from bottom left to bottom right). Arrows represent ion and neutral velocity vectors in the $x-y$ plane. Hot coronal plasma is blue, cold chromospheric plasma is orange-red, and intermediate transition region plasma/interface between them is green on the colormap.

and it reaches a level of $y \approx 5.0$ Mm. It is followed by a second, stronger shock, which results at maximum of $f(t)$. However, the chromospheric (cold) ion plasma is located at $y \approx 2.8$ Mm at this time (see Figure 4, the top-left panel). The shock fronts move continuously upward, which attain the level of more than $y = 25$ Mm (not drawn here) and the chromospheric plasma reaches its maximum height of $y \approx 4.9$ Mm at $t = 210$ s (Figure 4, the top-middle panel). The head of the spicule remains denser (yellow color on the colormap), while its interior rarefies in time (green color on the colormap) due to rarefaction wave propagating upwards. Above the apex of the ion spicule, we can see a constant stream of ions injected into higher layers of the solar corona. In addition, the down-falling of the ion spicule plasma also starts as the time progresses. The reverse velocity arrows in the central region and sides of the ion spicule justifies downfall of the cold chromospheric plasma. This downfall is stronger during the decay phase (see reverse velocity arrows in the top-middle and top-right panels), which creates the V-shaped structure as the down-falling velocity is nonuniform along the horizontal direction (see the top-right panel).

We have implemented the two-fluid approach in our numerical experiment to understand the behavior of ions and neutrals in the spicule dynamics. It may be possible that the ions and neutrals may exhibit the different dynamics. Therefore, we show the corresponding profiles of $\log(\varrho_n(x, y))$ in the bottom panels of Figure 4. The overall dynamics of the neutrals

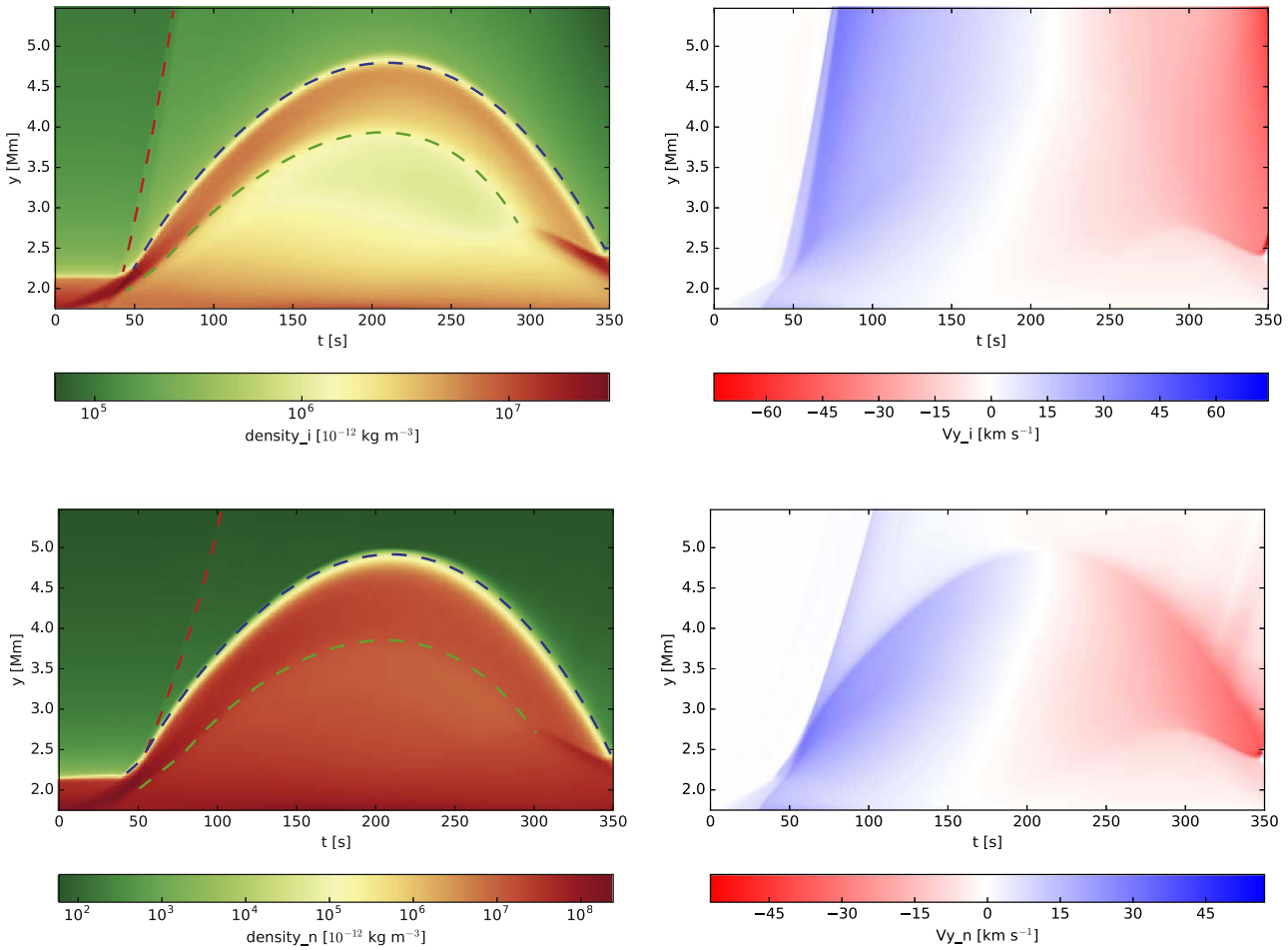

Figure 5. Temporal evolution of $\log(\varrho_{i,n}(x = 0, y))$ (left) and $V_{i,n\,y}(x = 0, y)$ (right) for the ions (top) and neutrals (bottom). The red, blue, and green dashed lines indicate slow shock, contact wave, and rarefaction wave, respectively. Transition from the red to the green area shows the contact waves.

(i.e., formation of a shock front and lagging off chromospheric plasma) are qualitatively similar to the dynamics of ions in this numerical experiment. However, the slow neutral shock does not propagate along magnetic field lines, forming a circle-like front (the bottom-left panel). There is also no upward stream consisting of neutrals above the apex of the ion spicule (the bottom-middle panel). The spicule is surrounded by the neutral cloud in which we can spot vortices of Rayleigh–Taylor instabilities during the decay phase. The down-falling of neutral gas is very weak during the maximum phase (the middle-right panel), which is mostly dominated toward the edges of the neutral spicule. However, the strong downflow of neutral gas occurs during the decay phase. The neutral spicule resembles a V-shaped structure in the decay phase (the bottom-right panel) but not as prominent as it occurs in the ion spicule. Because neutrals are not guided by the magnetic field, the neutral gas experiences more horizontal spread compared to the ions. So, the neutral spicule does not exhibit a very sharp V-shaped structure due to the dominance of the horizontal spreading of neutrals.

In addition, the top of the ion (neutral) spicule is suppressed until the height of $y = 3.4$ Mm ($y = 3.5$ Mm) due to the dominance of down-falling in the decay phase. This down-falling is strongest on sides of the ion/neutral spicule and decrease outward, which creates the V-shape structure at the bottom of ion/neutral spicules. Most of the chromospheric plasma, which was injected into the corona falls toward the chromosphere/TR.

We estimate now the width of the spicule in neutrals and ions at $y = 3.0$ Mm during the maximum phase of the spicule. By looking at horizontal mass density profiles and assuming that the mass density above (below) 1.2 times of the background mass density (i.e., mass density in the absence of any spicule; at $x = -1.0$ Mm) are considered as the starting (end) points of the spicules. We find that the neutral spicule is wider ($\sim$600 km) than the ion spicule than the spicule consisting of ions ($\sim$400 km).

We discuss now temporal evolution of mass densities and vertical velocities of ions and neutrals. Figure 5 displays time signatures of $\varrho_{i,n}(x = 0, y, t)$ (the left panels) and $V_{i,n\,y}(x = 0, y, t)$ (the right panels) for ions (the top panels) and neutrals (the bottom panels). The rise time of the chromospheric ions to their maximum height is about 210 s (see Figure 5, top-left). In the temporal evolution profile of the ions, we spot three major waves above the TR (the top-left panel): the leading wave is a slow shock wave (red line) that is followed by the contact wave (blue line) and the rarefaction wave (green line). The contact wave does not appear in the top-right panel since there is no jump in velocity of ions across a contact surface with normal almost perpendicular to $\boldsymbol{B}$. See also Kuźma et al. (2017) for a similar discussion in the MHD case. The light-green area between slow shock and contact

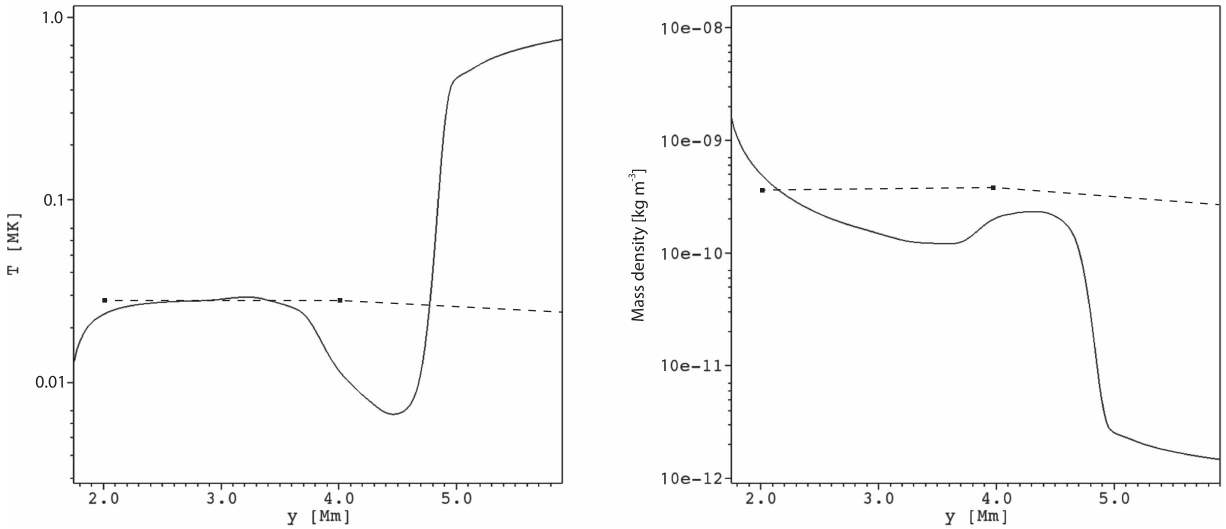

Figure 6. Vertical profiles of average temperature (the left panel) and mass density (the right panel) of the spicule in the simulation evaluated along $x = 0$ Mm, at $t = 210$ s (the solid lines) and observational data of Beckers (1968; the dashed lines).

wave reveals that a significant amount of ions are constantly injected above the spicule apex during its lifetime. This phenomenon is absent in the case of neutrals (the bottom-left panel). The ion slow shock travels with higher speed ($\sim$150 km s^{-1}) than neutral slow shock ($\sim$90 km s^{-1}; see the right panels). Both ions and neutrals injected into the corona above the spicule apex accelerate with height. The light-green area below the apex of the ion spicule reveals that the rarefaction wave exerts a greater impact on the already rarefied ion spicule. The boundary between chromospheric and coronal neutrals is also sharper than between chromospheric and coronal ions. This is a result of merging between the top of the ion spicule and highly ionized corona. From the temporal evolution profile of the neutrals, we infer that both shock and rarefaction waves are of low amplitudes, to the point, when the rarefaction wave is almost unnoticeable (green line, the bottom-left panel). At a later time, the chromospheric plasma, which was earlier injected into the corona, begins to fall toward the TR.

The spicule consists mostly of dense and cold neutrals. The ionization level at all stages of the spicule evolution remains at about 10%. Figure 6 (left) shows the vertical profile of the average temperature of the simulated spicule (solid line) along with the widely used observed values (dashed line; Beckers 1968). The average temperature of the spicule (solid line) is 100 times lower than the coronal plasma, which shows a constant value of temperature up to a height of $\sim$2.8 Mm. The spicule plasma exhibits its lowest temperature of 9000 K in the upper part of the spicule, $\sim$4500 km above the TR. Higher up, the temperature experiences an abrupt jump at the contact wave, reaching temperatures of up to 800,000 K and matching the local coronal temperature. Figure 6 (left) shows the vertical profile of mass density of the spicule (solid line). The cold head of the spicule is about twice denser than its core, which is resembled by the weak bump around $y = 4.2$ Mm. Above the apex of the spicule, mass density decreases to its coronal values. The temperature as well as mass density of the simulated spicule are compared with the classical results of the spicule (dashed line in both-panels of Figure 6; Beckers 1968). Observationally, it is reported that mass density and temperature are almost constant over the whole length of the spicule, which vary by about 10 % over the whole length of the spicule (Beckers 1968). However, the simulated spicule exhibits significant variations in the temperature and mass density along its length. It should be noted that the temperature of the spicule matches the observed values over a height range of 2.0 Mm $< y <$ 3.7 Mm.

We now discuss gradients of gas pressures of neutrals and ions. The corresponding vertical profiles are displayed in Figure 7. The dotted line shows the gas pressure gradient of neutrals, while the solid line illustrates the gas pressure gradient of ions along the y-direction.

The left (right) panel illustrates the vertical distribution of the gas pressure gradient at $t = 60$ s ($t = 70$ s). It is clear that the neutral gas pressure gradient (the dotted line) is very high in comparison to the ion gas pressure gradient (the solid line) at these instants of time. The difference between neutrals and ions pressure gradients is higher at about $y = 1.75$ Mm at which the driver in gas pressures operates. The gradients approach each other far away from the driver. The significant gas pressure gradient difference between the ions and neutrals is an important result, which clearly leads to a different dynamics of ions and neutrals.

4. Discussions and Conclusions

We have performed numerical simulations of a spicule by setting in the upper chromosphere localized time-dependent signals in ion and neutral gas pressures. The initial magnetic field configuration was current-free, and the atmosphere was stratified hydrostatically. The whole physical system was described by a set of two-fluid equations. Our numerical findings revealed that, as a result of the rapid decrease of the mass density with height, an upwardly propagating signal quickly steepens into a shock. This shock propagates along the magnetic field lines, reaching the low solar corona, and is followed by the chromospheric plasma, which consists of the cold and dense jet (spicule). This jet exhibits properties of a contact wave (Kuźma et al. 2017) and reaches upto a certain height (typically 4–6 Mm) and then returns to the chromosphere. The mean upflow speed was 20–25 km s^{-1}. The comparison between the numerical and observational data

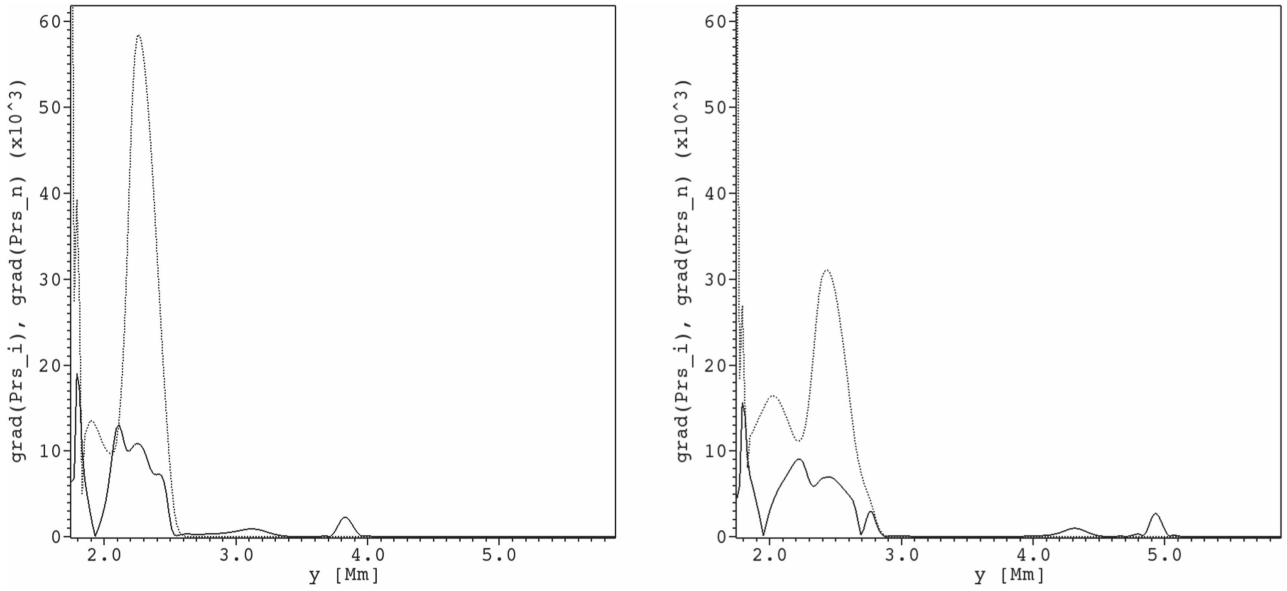

Figure 7. Vertical profiles of the gas pressure gradient of neutrals (the dotted line) and ions (the solid line) evaluated along $x = 0$ Mm, at $t = 60$ s (the left panel) and $t = 70$ s (the right panel).

always enlightens the path to go further. Therefore, we tried to compare the observed properties of the simulated spicule with the various spicule observations. Beckers (1968, 1972) reported that the average height of spicules can vary from 6500 km to 9500 km. Similarly, Lippincott (1957) reported the spicule height range from 7000 to 13,000 km and Pasachoff et al. (2009) inferred these numbers from 4200 to 12,200 km. Observed upward velocity of spicules exhibits variations within the range of 20.0–150.0 km s^{-1} (De Pontieu et al. 2007b) and 3.0–75.0 km s^{-1} (Pasachoff et al. 2009). The numerically obtained value of spicule height (∼4.9 Mm) and upward velocity (∼20–25 km s^{-1}) of the simulated spicule lies in the observed range of height and velocity (Beckers 1968, 1972; De Pontieu et al. 2007b; Pasachoff et al. 2009). It should also be noted that the numerical values of the spicule match those obtained for MHD (Kuźma et al. 2017).

Novelty of our numerical simulations lies in the usage of the two-fluid model, which was not investigated so far. The two-fluid simulations invoke real physical conditions of the lower solar atmosphere and plasma processes within various localized jets. It is noteworthy that a significant role of neutrals associated with confined pseudo-shocks in carrying substantial energy and mass into the overlying solar atmosphere was discovered by Srivastava et al. (2017). The key findings of our simulations can be summarized as follows. (a) The spicule dynamics is slightly different in ions and neutrals; (b) the core of the spicule is dominated by cold neutrals; (c) the neutral spicule is wider compared to the ion spicule; (d) the ionization remains essentially still with height and horizontal distance within the spicule, only the top of the spicule is significantly ionized; and (e) in later moments of time of the spicule evolution higher amplitude of the slow rarefaction wave for the ion spicule results in a different structure than for the neutral spicule. The general scenario of the rise and the downfall of the spicule is the same for ions and neutrals and it is close to that for MHD (Kuźma et al. 2017). The dispatches in gas pressure gradients between ions and neutrals is a key factor to understand the minor differences in the dynamics of ions and neutral spicules. Obviously, the magnetic field does not have any direct influence on the dynamics of neutrals, while the motion of ions is affected by the magnetic field directly. The direct influence of the magnetic field on the ions controls the width of the ion spicule. Therefore, the ion spicule is a very well collimated column of ions with its small width. In the absence of the influence of magnetic field, the neutrals get extra freedom to propagate in the horizontal direction; a constraint on them results from ion-neutral collisions. As a result, the neutral spicule is wider compared to the ion spicule. The V-shaped structure near the base of the ion/neutral spicule is an interesting phenomenon of these simulations, which results from down-falling gas. As ions are affected by magnetic field, the well collimated down-falling ion gas results in, which exerts the gas pressure force producing in the decay phase the sharp V-shaped structure near the base of the ion spicule.

Most of observations reveal that temperature and mass density of a spicule remain essentially constant along its height (Beckers 1968, 1972; see also review article by Sterling 2000). However, our simulated spicule shows a significant variations in its temperature as well as mass density. The temperature of the spicule is constant upto the height of $y = 3.5$ Mm, while higher up the temperature falls off abruptly. The constant phase of temperature matches the obervational findings. However, there is a sharp increase in the temperature above $y = 4.5$ Mm, which may suggest that the thermal evolution of the cold chromospheric plasma can be important as proposed by Pereira et al. (2014). Overall, the mass density of the spicule is decreasing with height, which is qualitatively consistent with the observed mass densities (Beckers 1968). However, the top of the spicule shows slightly higher densities. The high temperature near the top-part of the spicule significantly ionizes the neutrals, which were taken into account in the present scenario. Recently, Pereira et al. (2014) reported that spicules undergo thermal evolution using high-resolution observations. Spicules produce more emission near their bases compared to their apexes at chromospheric temperature (i.e., Ca II H & K and Mg II h & k lines). However, bases of spicules become dark and the top parts of spicules lead to more emissions at the TR temperature (i.e., Si IV; $T = 80$ kK). This

observational finding predicts that ionization grows with height within the spicule, which is successfully reproduced by our two-fluid numerical simulations of spicules.

In conclusion, our numerical simulations of the spicule performed within the framework of the two-fluid approach successfully mimics the averaged properties of classical spicules. Ion and neutral spicules follow the similar dynamics in terms of rise time and peak altitude. The core of the spicule exhibits an abundance of neutrals, with growing in time rarefaction of ions.

The authors express their thanks to the referee for comments on the earlier version of the draft. This work was financially supported by the project from the National Science Centre, Poland, (NCN) Grant No. 2014/15/B/ST9/00106. The JOANNA code used in this work was developed by Mr. Darek Wójcik. These numerical simulations were performed on the LUNAR cluster at Institute of Mathematics of University of M. Curie-Skłodowska. Visualization of the simulations data was done with the use of IDL (Interactive Data Language) and VisIt software packages.

References

Avrett, E. H., & Loeser, R. 2008, ApJS, 175, 228
Beck, C., Rezaei, R., Puschmann, K. G., & Fabbian, D. 2016, SoPh, 291, 2281
Beckers, J. M. 1968, SoPh, 3, 367
Beckers, J. M. 1972, ARA&A, 10, 73
Cheng, Q.-Q. 1992, A&A, 266, 537
Courant, R., Friedrichs, K., & Lewy, H. 1928, MatAn, 100, 32
Cranmer, S. R., & Woolsey, L. N. 2015, ApJ, 812, 71
Cranmer, S. R., & Woolsey, L. N. 2016, ApJ, 822, 119
De Pontieu, B., Erdélyi, R., & James, S. P. 2004, Natur, 430, 536
De Pontieu, B., Hansteen, V. H., Rouppe van der Voort, L., van Noort, M., & Carlsson, M. 2007a, ApJ, arXiv:astro-ph/0701786
De Pontieu, B., McIntosh, S., Hansteen, V. H., et al. 2007b, PASJ, 59, S655
De Pontieu, B., McIntosh, S. W., Hansteen, V. H., & Schrijver, C. J. 2009, ApJL, 701, L1
Haerendel, G. 1992, Natur, 360, 241
Hansteen, V. H., De Pontieu, B., Rouppe van der Voort, L., van Noort, M., & Carlsson, M. 2006, ApJL, 647, L73
Heggland, L., De Pontieu, B., & Hansteen, V. H. 2007, ApJ, 666, 1277
Hirayama, T. 1992, SoPh, 137, 33
Hollweg, J. V. 1972, CosEl, 2, 423
Hollweg, J. V. 1982, ApJ, 257, 345
Hollweg, J. V., Jackson, S., & Galloway, D. 1982, SoPh, 75, 35
James, S. P., Erdélyi, R., & De Pontieu, B. 2003, A&A, 406, 715
Konkol, P., Murawski, K., & Zaqarashvili, T. V. 2012, A&A, 537, A96
Kopp, R. A., & Kuperus, M. 1968, SoPh, 4, 212
Kudoh, T., & Shibata, K. 1999, ApJ, 514, 493
Kuźma, B., Murawski, K., Zaqarashvili, T. V., Konkol, P., & Mignone, A. 2017, A&A, 597, 133
Lippincott, S. L. 1957, SCoA, 2, 15
Madjarska, M. S., Vanninathan, K., & Doyle, J. G. 2011, A&A, 532, L1
Matsuno, K., & Hirayama, T. 1988, SoPh, 117, 21
McIntosh, S. W., & De Pontieu, B. 2009, ApJ, 707, 524
McIntosh, S. W., Innes, D. E., De Pontieu, B., & Leamon, R. J. 2010, A&A, 510, L2
Moore, R. L., & Fung, P. C. W. 1972, SoPh, 23, 78
Murawski, K., & Zaqarashvili, T. V. 2010, A&A, 519, A8
Nakariakov, V. M., & Verwichte, E. 2005, LRSP, 2, 3
Nishikawa, T. 1988, PASJ, 40, 613
Pasachoff, J. M., Jacobson, W. A., & Sterling, A. C. 2009, SoPh, 260, 59
Pereira, T. M. D., De Pontieu, B., & Carlsson, M. 2012, ApJ, 759, 18
Pereira, T. M. D., De Pontieu, B., Carlsson, M., et al. 2014, ApJL, 792, L15
Pereira, T. M. D., Rouppe van der Voort, L., & Carlsson, M. 2016, ApJ, 824, 65
Roberts, B. 1979, SoPh, 61, 23
Roberts, W. O. 1945, ApJ, 101, 136
Rouppe van der Voort, L., De Pontieu, B., Pereira, T. M. D., Carlsson, M., & Hansteen, V. 2015, ApJL, 799, L3
Secchi, P. A. 1887, Le Soleil, Vol. 2 (Paris: Gauthier-Villars)
Skogsrud, H., Rouppe van der Voort, L., & De Pontieu, B. 2014, ApJL, 795, L23
Skogsrud, H., Rouppe van der Voort, L., De Pontieu, B., & Pereira, T. M. D. 2015, ApJ, 806, 170
Smith, P. D., & Sakai, J. I. 2008, A&A, 486, 569
Srivastava, A. K., Murawski, K., Kuźma, B., et al. 2017, NatAs, in press
Sterling, A. C. 2000, SoPh, 196, 79
Sterling, A. C., & Hollweg, J. V. 1984, ApJ, 285, 843
Sterling, A. C., & Mariska, J. T. 1990, ApJ, 349, 647
Sterling, A. C., & Moore, R. L. 2016, ApJL, 828, L9
Sterling, A. C., Moore, R. L., & DeForest, C. E. 2010, ApJL, 714, L1
Sterling, A. C., Shibata, K., & Mariska, J. T. 1993, ApJ, 407, 778
Suematsu, Y. 1998, in ESA Special Publication 421, Solar Jets and Coronal Plumes, ed. T.-D. Guyenne (Paris: ESA), 19
Suematsu, Y., Ichimoto, K., Katsukawa, Y., et al. 2008, in ASP Conf. Ser. 397, First Results From Hinode, ed. S. A. Matthews, J. M. Davis, & L. K. Harra (San Francisco, CA: ASP), 27
Suematsu, Y., Shibata, K., Neshikawa, T., & Kitai, R. 1982, SoPh, 75, 99
Suematsu, Y., Wang, H., & Zirin, H. 1995, ApJ, 450, 411
Tian, H., McIntosh, S. W., Habbal, S. R., & He, J. 2011, ApJ, 736, 130
Tsiropoula, G., Tziotziou, K., Kontogiannis, I., et al. 2012, SSRv, 169, 181
Zaqarashvili, T. V., & Erdélyi, R. 2009, SSRv, 149, 355
Zaqarashvili, T. V., Khodachenko, M. L., & Rucker, H. O. 2011, A&A, 529, A82

Monthly Notices
of the
ROYAL ASTRONOMICAL SOCIETY

MNRAS **481,** 262–267 (2018)
Advance Access publication 2018 August 23

doi:10.1093/mnras/sty2306

Acoustic waves in two-fluid solar atmosphere model: cut-off periods, chromospheric cavity, and wave tunnelling

D. Wójcik,[1]★ K. Murawski[1] and Z. E. Musielak[2,3]

[1]*Group of Astrophysics, University of M. Curie-Skłodowska, ul. Radziszewskiego 10, PL-20-031 Lublin, Poland*
[2]*Department of Physics, University of Texas at Arlington, Arlington, TX 76019, USA*
[3]*Kiepenheuer-Institut für Sonnenphysik, Schöneckstr. 6, D-79104 Freiburg, Germany*

Accepted 2018 August 21. Received 2018 August 21; in original form 2018 June 13

ABSTRACT

We perform numerical simulations of acoustic waves in a two-fluid model of quiet region of the solar atmosphere. The two-fluid model describes partially ionized (non-magnetized) solar plasma, whose main components are neutral atoms, protons, and electrons. The waves are excited by a monochromatic driver, which operates at the bottom of the solar photosphere. Our numerical results show that the driver excites ion and neutral acoustic waves whose propagation is affected by the gravity. As a result, the acoustic waves with periods higher than a local acoustic cut-off period are evanescent, while lower waveperiods are free to reach the solar corona. Acoustic waves, which are evanescent in the photosphere and low chromosphere, tunnel their energy into the upper chromosphere and the transition region. The wave propagation to the solar corona is affected by partial wave reflection that occurs in the transition region, and is responsible for formation of a cavity, where the waves are trapped. Fourier power analysis of temporal characteristic of plasma quantities reveals that a spectrum of various periods is generated. While oscillations traced in ion and neutral velocities look very similar, dynamics of mass densities of ions and neutrals differs a lot. The obtained results clearly show that the two-fluid model provides new insights into the acoustic wave propagation in a more realistic (partially ionized) quiet region of the solar atmosphere.

Key words: hydrodynamics – waves – Sun: atmosphere.

1 INTRODUCTION

The atmosphere of the Sun classically consists of three major layers that exhibit different physical properties. The relatively dense and cold photosphere stretches approximately from the top of the convection zone to a height of about 500 km, and its temperature of about 6×10^3 K is low enough so a majority of neutrals occupy this layer with one ion per about 10^3–10^4 neutrals (e.g. Khomenko et al. 2014). Higher up in the atmosphere lies the chromosphere, which is about 1600 km thick, and also partially ionized. The solar corona is located above the transition zone and it extends to about 2–3 solar radii (Aschwanden 2005), and it is essentially fully ionized. The mass density in the solar atmosphere decreases with height but the horizontally averaged temperature behaves intriguingly different; first it decreases with height from about 5.6×10^3 K at the solar surface, located in the photosphere, to its minimum of about 4.3×10^3 K about 100 km above the top of the photosphere (Priest 2009). Surprisingly enough, in the chromosphere temperature starts to increase, first slowly to about 3×10^4 K at the top of the chromosphere, and higher up in a narrow (about 100 km thick) transition region where it rapidly grows reaching average values of 1–2 MK in the corona (Aschwanden 2005). The described physical conditions in the solar atmosphere clearly show that in any realistic studies of the solar photosphere and chromosphere, neutrals and ions must be accounted for, and this is the main aim of this paper.

Being a highly dynamical medium, the solar atmosphere is pervaded by various types of waves. Among them the simplest conceivable oscillations are acoustic waves in quiet (magnetic-free) solar regions (Nakariakov & Verwichte 2005). However, a detailed analysis of these oscillations reveals their high level of complexity. It has been known for a long time that not all acoustic waves are free to propagate through the solar atmosphere. According to the theory developed by Lamb (1909, 1911), only waves with their wave period P smaller than $P_{\rm ac}$, which is the acoustic cut-off period, penetrate the atmosphere; otherwise the waves are evanescent and their amplitude decays with height. Lamb (1911) extended his theory to an atmosphere with linear temperature profile and subsequently his work was generalized, among others, by Moore & Spiegel (1964); Campos (1986); Deubner & Gough (1984); Fleck & Schmitz (1993). Recently Musielak, Musielak & Mobashi (2006); Fawzy & Musielak (2012), Routh & Musielak (2014) and Afanasyev & Nakariakov

★ E-mail: dwojcik@kft.umcs.lublin.pl

(2015) derived analytically different expressions for the acoustic cut-off and demonstrated that this cut-off is a sensitive function of height. These analytical approaches were supplemented by a number of numerical simulations of acoustic waves (e.g. Ulmschneider et al. 1978; Carlsson & Stein 1997; Cuntz, Ulmschneider & Musielak 1998; Fawzy et al. 2002; Murawski & Musielak 2016; Murawski et al. 2016; Kraśkiewicz, Murawski & Musielak 2018). Two-dimensional counterpart of acoustic cut-off frequency in the solar atmosphere was derived by Kuridze et al. (2009). Both the analytical and numerical studies of the propagation of acoustic waves were performed for the fully ionized solar atmosphere.

The main purpose of this paper is to consider a two-fluid (for neutrals and ions) model of the solar photosphere and chromosphere, and investigate numerically the existence of the acoustic cut-off in this model and its effect on the acoustic wave propagation. Our numerical results show how the cut-off depends on the atmospheric height, and also demonstrate the effects of wave trapping in a cavity that is formed in the upper chromosphere as a result of partial wave reflection in the solar transition region. Since the reflection is only partial, our results allow estimating the amount of acoustic wave energy that reaches the solar corona through the tunnelling effect through the transition region. Our results have important implications on the heating mechanism of the solar chromosphere and on the excitation of atmospheric oscillations.

This paper is organized as follows. The following section is devoted to presentation of basic two-fluid equations. Section 3 describes the model of the solar atmosphere and Section 4 is devoted to consideration of the acoustic cut-off. Numerical results are presented in Section 5, and our summary of the main results is given in Section 6.

2 GOVERNING EQUATIONS

We consider a quiet region of the solar atmosphere whose lower layers, as a result of low temperature, contain a vast number of neutrals (Khomenko et al. 2014; Ballester et al. 2018). As in such quiet region the magnitude of magnetic field is of the order of few Gs only, its influence on the propagation of acoustic waves is so small that it can be neglected. Because of the presence of neutrals and ions, a realistic atmospheric model must use a set of two-fluid equations that can be split into those for neutrals and ions (e.g. Zaqarashvili, Khodachenko & Rucker 2011; Oliver et al. 2016). This set of equations can be written for neutrals as follows:

$$\frac{\partial \varrho_{\rm n}}{\partial t} + \nabla \cdot (\varrho_{\rm n} \boldsymbol{V}_{\rm n}) = S_1 \,, \tag{1}$$

$$\frac{\partial (\varrho_{\rm n} \boldsymbol{V}_{\rm n})}{\partial {\rm t}} + \nabla \cdot (\varrho_{\rm n} \boldsymbol{V}_{\rm n} \boldsymbol{V}_{\rm n} + p_{\rm n} \boldsymbol{I}) = S_2 + S_1 \boldsymbol{V}_{\rm n} + \varrho_{\rm n} \boldsymbol{g} \,, \tag{2}$$

$$\frac{\partial E_{\rm n}}{\partial {\rm t}} + \nabla \cdot [(E_{\rm n} + p_{\rm n}) \boldsymbol{V}_{\rm n}] = S_3^{\rm n} + S_1 \frac{|\boldsymbol{V}_{\rm n}|^2}{2} + \varrho_{\rm n} \boldsymbol{g} \cdot \boldsymbol{V}_{\rm n} \,, \tag{3}$$

$$E_{\rm n} = \frac{p_{\rm n}}{\gamma - 1} + \frac{\varrho_{\rm n} |\boldsymbol{V}_{\rm n}|^2}{2}. \tag{4}$$

Ions (i) with electrons (e) are treated as a separate single fluid, which evolution is governed by the following equations:

$$\frac{\partial \varrho_{\rm i}}{\partial t} + \nabla \cdot (\varrho_{\rm i} \boldsymbol{V}_{\rm i}) = -S_1 \,, \tag{5}$$

$$\frac{\partial (\varrho_{\rm i} \boldsymbol{V}_{\rm i})}{\partial t} + \nabla \cdot (\varrho_{\rm i} \boldsymbol{V}_{\rm i} \boldsymbol{V}_i + p_{\rm ie} \boldsymbol{I}) = -S_2 - S_1 \boldsymbol{V}_{\rm i} + \varrho_{\rm i} \boldsymbol{g} \,, \tag{6}$$

$$\frac{\partial E_{\rm ie}}{\partial t} + \nabla \cdot [(E_{\rm ie} + p_{\rm ie}) \boldsymbol{V}_{\rm i}] = S_3^{\rm i} - S_1 \frac{|\boldsymbol{V}_{\rm i}|^2}{2} + \varrho_{\rm i} \boldsymbol{g} \cdot \boldsymbol{V}_{\rm i} \,, \tag{7}$$

$$E_{\rm ie} = \frac{p_{\rm ie}}{\gamma - 1} + \frac{\varrho_{\rm i} |\boldsymbol{V}_{\rm i}|^2}{2}. \tag{8}$$

Here $\boldsymbol{V}_{\rm i}$ ($\boldsymbol{V}_{\rm n}$) is a velocity of ions (neutrals), $\varrho_i(\varrho_{\rm n})$ mass density, $p_{\rm ie}$ ($p_{\rm n}$) gas pressure, $E_{\rm ie}(E_{\rm n})$ total energy density, and $\boldsymbol{g} = [0, -g, 0]$ is a gravity vector. Other plasma quantities have their standard notation with subscripts $_{\rm i}$ and $_{\rm n}$ corresponding to ions and neutrals, respectively. We set and hold fixed the specific heats ratio $\gamma = 1.4$ and $g = 274.96\,{\rm m\,s^{-2}}$. The additional source terms that couple these two sets of equations are (Oliver et al. 2016)

$$S_1 = \varrho_{\rm i}(\alpha_{\rm r} \varrho_{\rm i} - \alpha_{\rm i} \varrho_{\rm n}), \tag{9}$$

$$S_2 = \alpha_{\rm c}(\boldsymbol{V}_{\rm i} - \boldsymbol{V}_{\rm n}), \tag{10}$$

$$S_3^{\rm i} = \alpha_c \left[\frac{1}{2} |\boldsymbol{V}_{\rm i} - \boldsymbol{V}_{\rm n}|^2 + \frac{3 k_{\rm B}}{m_{\rm H}(\mu_{\rm i} + \mu_{\rm n})} (T_{\rm n} - T_{\rm i}) \right], \tag{11}$$

$$S_3^{\rm n} = \alpha_c \left[\frac{1}{2} |\boldsymbol{V}_{\rm i} - \boldsymbol{V}_{\rm n}|^2 + \frac{3 k_{\rm B}}{m_{\rm H}(\mu_{\rm i} + \mu_{\rm n})} (T_{\rm i} - T_{\rm n}) \right]. \tag{12}$$

Here, $k_{\rm B}$ is the Boltzmann constant, $m_{\rm H}$ hydrogen mass, $\mu_{\rm i}$ and $\mu_{\rm n}$ are mean masses of ions and neutrals, respectively. The first term in $S_3^{\rm i,n}$ corresponds to plasma heating due to the elastic collisions, while the additional terms proportional to temperature are associated with heating/cooling of plasma, resulting from heat exchange between the fluids. The symbols for $\alpha_{\rm r}$, $\alpha_{\rm i}$, and $\alpha_{\rm c}$ stand for recombination, ionization, and collision, respectively, between ions and neutrals.

3 HYDROSTATIC EQUILIBRIUM

We assume that there is the hydrostatic equilibrium of all plasma species (ions, neutrals, and electrons) and that their temperature is the same ($T_{\rm i} = T_{\rm n} = T_{\rm e} = T$), which is adopted from the semi-empirical atmospheric model developed by Avrett & Loeser (2008). However, we note that this assumption of the fixed temperature is implemented at $t = 0$ only, and at the later moments of time this assumption is released and ions and neutrals are allowed to have different temperatures.

With the use of ideal gas law for neutrals ($p_{\rm n} = n_{\rm n} k_{\rm B} T$) and ion–electron mixture ($p_{\rm ie} = 2 n_{\rm i} k_{\rm B} T$) as well as the hydrostatic equations for both fluids, from the momentum equations one can find the following expressions:

$$\frac{{\rm d} p_{\rm ie}}{{\rm d} y} = -g \varrho_{\rm i} \,, \tag{13}$$

$$\frac{{\rm d} p_{\rm n}}{{\rm d} y} = -g \varrho_{\rm n} \,. \tag{14}$$

The solutions to the above given equations are (e.g. Murawski et al. 2015)

$$p_{\rm ie} = p_{\rm ie}^0 \exp \left[\int_{y_r}^{y} \frac{{\rm d} y'}{\Lambda_{\rm ie}(y')} \right], \tag{15}$$

$$p_{\rm n} = p_{\rm n}^0 \exp \left[\int_{y_r}^{y} \frac{{\rm d} y'}{\Lambda_{\rm n}(y')} \right], \tag{16}$$

where

$$\Lambda_{\rm ie}(y) = \frac{2 k_{\rm B} T(y)}{g \mu_{\rm i} m_{\rm H}} \,, \quad \Lambda_{\rm n}(y) = \frac{k_{\rm B} T(y)}{g \mu_{\rm n} m_{\rm H}} \,, \tag{17}$$

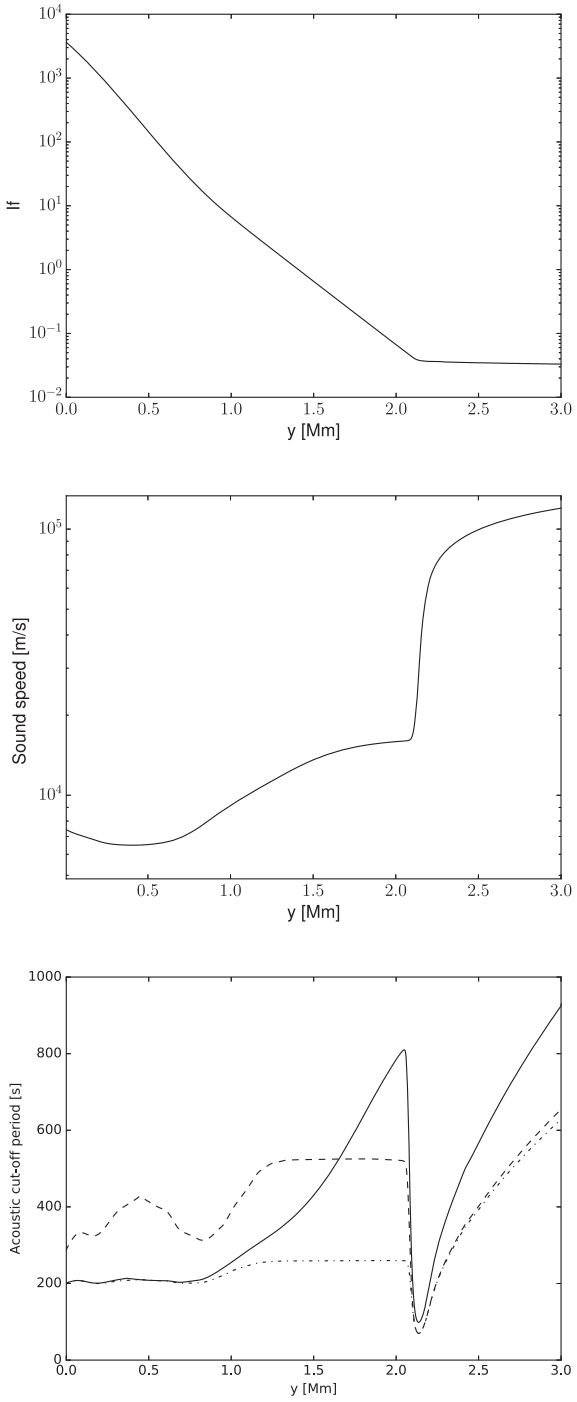

Figure 1. The ionization fraction ϱ_n/ϱ_i (top), the sound speed (middle), and the acoustic cut-off period P_{ac} (bottom) for combined ion–electron–neutral fluid (solid line), ionized fluid (dashed line), and neutrals (dot dashed line), for two-fluid solar atmosphere versus height.

are pressure scale heights for ions–electrons and neutrals, respectively. The symbols p_{ie}^0 and p_n^0 denote pressures evaluated at the reference level $y = y_r = 10$ Mm. The mean masses for ions ($\mu_i \approx 0.58$) and neutrals ($\mu_n \approx 1.21$) are calculated from the OPAL solar abundance model (Vögler et al. 2004), and they are altered by the presence of electrons in ionized fluid. As a result, the ionization fraction $I_f = \varrho_n/\varrho_i$ attains a value of about 3655 at $y = 0$ (Fig. 1, top) and higher up it declines to coronal value of 3×10^{-2}.

The single fluid pressure scale height is defined as

$$\Lambda \equiv \left| \frac{p}{\frac{dp}{dy}} \right|, \tag{18}$$

where $p = p_{ie} + p_n$, is the total (ion–electron plus neutrals) gas pressure. The sound speed for the two-fluid system is specified as

$$c_s = \sqrt{\gamma \frac{p}{\varrho}} = \sqrt{\gamma \frac{\left(2\frac{\varrho_i}{\mu_i} + \frac{\varrho_n}{\mu_n}\right)\frac{k_B T}{m_H}}{\varrho_i + \varrho_n}}, \tag{19}$$

and its plot with atmospheric height is given in Fig. 1.

4 ACOUSTIC CUT-OFF PERIOD

The acoustic cut-off period for the two-fluid atmospheric model considered here has not yet been determined analytically, and finding it out is the scope of this paper, which is mainly concerned with numerical studies. Nevertheless, it is our intention to use a formula obtained analytically for fully ionized plasma to find an approximate range of periods corresponding to the propagating and evanescent acoustic waves, and compare this range to that determined by our numerical simulations. Obviously, the validity of such formula for our two-fluid model may be questioned, however, its results are used for comparison only.

There are several formulas for the acoustic cut-offs in the solar atmosphere and these formulas are presented and described by Wiśniewska et al. (2016); Fawzy & Musielak (2012). Among the previously obtained formulas for the cut-offs, those obtained originally by Lamb (1909) and later by Deubner & Gough (1984); Fleck & Schmitz (1993); Musielak et al. (2006); Roberts (2006); Routh & Musielak (2014) are the most commonly used. With the formula given by Deubner & Gough (1984) being very often adopted in helioseismology, we decided to use this formula for our comparison between analytical and numerical predictions. The formula is typically written as

$$P_{ac} = \frac{4\pi\Lambda}{c_s\sqrt{1 + 2\frac{d\Lambda}{dy}}}, \tag{20}$$

where Λ is a pressure scale height. We computed the cut-off resulting from this formula for combined ion–neutral–electron fluid and also for ion–electron and neutral fluids. For neutrals and combined fluid approach we obtained that P_{ac} is close to 200 s for $0 < y < 1$ Mm (see Fig. 1, bottom). For ionized plasma, its value is close to 300 s and it varies with height reaching its maximum value around 525 s for $1.35 < y < 2.0$ Mm. The cut-off periods are in general much lower for neutrals than for ions. The maximum value for neutrals below the transition region is around 260 s. For combined fluid, P_{ac} grows with height up to a value of about 10^3 s at $y \approx 2$ Mm. At the transition region, which is located at $y \approx 2.1$ Mm, P_{ac} drops abruptly to its local minimum of about 100 s and it grows fast in the corona. According to the linear theory of Lamb (1909), only waves of their period lower than P_{ac} are free to propagate. However, some waves that would be evanescent based on the formula, are still able to tunnel through the narrow forbidden zone such as that one which occurs at the transition region.

5 NUMERICAL RESULTS

In this part of the paper, we present results of numerical simulations we performed with the use of the JOANNA code (Wójcik & Murawski 2018). The code uses third-order accurate WENO scheme (Liu,

Osher & Chan 1994) for the spatial reconstruction and Runge–Kutta method for integration in time (Gottlieb & Shu 1998). We used a one-dimensional uniform grid of its finest size of $\Delta y = 5$ km between $y = 0$ and $y = 5.12$ Mm. Higher up the grid stretches up with height until the top boundary which is located at $y = 40$ Mm. At the bottom and top boundaries, we set and hold fixed in time all plasma quantities to their equilibrium values. Acoustic waves are excited by a monochromatic driver in a vertical component of velocity, which is given by

$$V_{\rm y}(y=0,t) = A_{\rm v}\ \sin\left(\frac{2\pi}{P_{\rm d}}t\right)\ . \tag{21}$$

Here, $A_{\rm v}$ is the amplitude of the driver which we set equal to 0.01 km s^{-1}, but allow its period $P_{\rm d}$ to vary. Results of the numerical simulations clearly show that acoustic waves of their period P below the cut-off period, $P_{\rm ac}$, are free to propagate through the whole solar atmosphere and arrive to the corona (Fig. 2), while waves of $P > P_{\rm ac}$ are evanescent (Fig. 3). We have run several cases of different driving periods but illustrate here only the cases of $P_{\rm d} = 50$ s and $P_{\rm d} = 300$ s. The former is much lower than $P_{\rm ac}(y = 0) \approx 200$ s, while the latter is higher than 200 s.

Apparent standing waves, which result from the interference between incoming and reflecting from the transition region signals, are well seen in Fig. 2. Note that nodes of the apparent standing waves are shifted for oscillations in mass densities (top and middle panels) and ion velocity (bottom panels). These apparent standing waves were also reported by Fleck & Schmitz (1991) for the case of the isothermal atmosphere. Time-distance plot of $V_{\rm yi}$ may also show that there is no propagation of long period waves as the wavelength seems to be infinite; the plasma is periodically going up and down without propagation. Similar results were obtained by Zaqarashvili, Khodachenko & Soler (2013) for long period Alfvén waves (see top panel of their fig. 6). We should also note that due to the sharp decrease in both mass density of ions and neutrals the acoustic waves steepen as they travel through the atmosphere. This is more visible for shorter waveperiods which are not a subject of this paper. As a result of large collision frequency between ions and neutrals, oscillations in neutral velocity (not shown) are very similar to oscillations in ion velocity (bottom panels) in the photosphere and low chromosphere; ions and neutrals are strongly coupled in these regions. Some small departures between ion and neutral velocities occur at higher altitudes at which the collision frequency is not that strong as they are in the bottom atmospheric layers (not shown).

From Fig. 2 we infer that ions and neutrals oscillate in a different manner. It is particularly emphasized in the case of $P_{\rm d} = 300$ s (Fig. 3). It follows from the linearized mass conservation equations for mass density perturbations $\delta\varrho_{\rm i,n}$ that

$$\frac{\partial\delta\varrho_{\rm i,n}}{\partial t} + V_{\rm y\,i,n}\frac{\partial\varrho_{\rm i,n}}{\partial y} \approx -\varrho_{\rm i,n}\frac{\partial V_{\rm y\,i,n}}{\partial y}\ .$$

The term on the right-hand side works as a source or sink which either enhances or reduces the amplitude of a signal. The second term on the left-hand side advects the signal and it results in reflection of ion and neutral acoustic waves. Although magnitudes of $\partial V_{\rm y\,i}/\partial y$ and $\partial V_{\rm y\,n}/\partial y$ are similar, the equilibrium mass densities, $\varrho_{\rm i,n}(y)$, differ a lot (not shown). This explains the dispatches between oscillations in perturbed mass densities of ions and neutrals (Figs 2 and 3, middle panels).

From Fig. 1 (middle panel) it follows that acoustic waves of their period P higher than $P_{\rm ac}(y = 0) \approx 220$ s are evanescent up to $y \approx 1$ Mm but they are allowed to propagate from the altitude of about 1 Mm up to the transition region. These large waveperiod

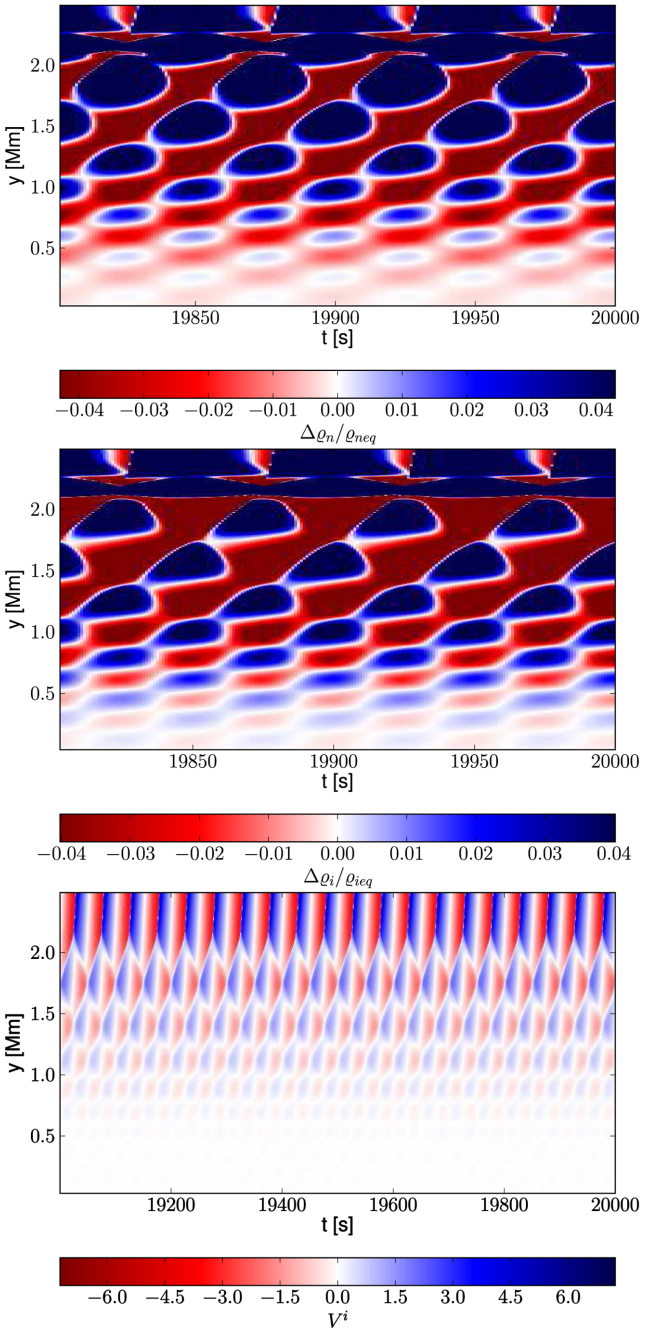

Figure 2. Time-distance plots of the perturbed mass density of neutrals (top panel) and ions (middle panel) as well as the ion velocity (bottom panel) for the driving period $P_{\rm d} = 50$ s. The perturbed mass densities are normalized by their hydrostatic counterparts, while ion velocity is expressed in units of km s^{-1}.

waves, being originated from the level of $y = 0$ Mm, transfer much of their energy into 227 s waveperiod waves. This process is illustrated by downwardly pointing dashed arrows in Fig. 4. The waves of $P = P_{\rm ac}(y = 0) = 227$ s are propagating through the region of $y > 1$ Mm (Fig. 4, green zone) and they tunnel through the transition region, which is shown by the horizontal solid arrows drawn at $y = 2.1$ Mm (Fig. 4).

As a result of wave reflection, which takes place on inhomogeneity centres in local sound speed (Fig. 1, bottom), acoustic waves excite oscillations of different periods than the driving period. This

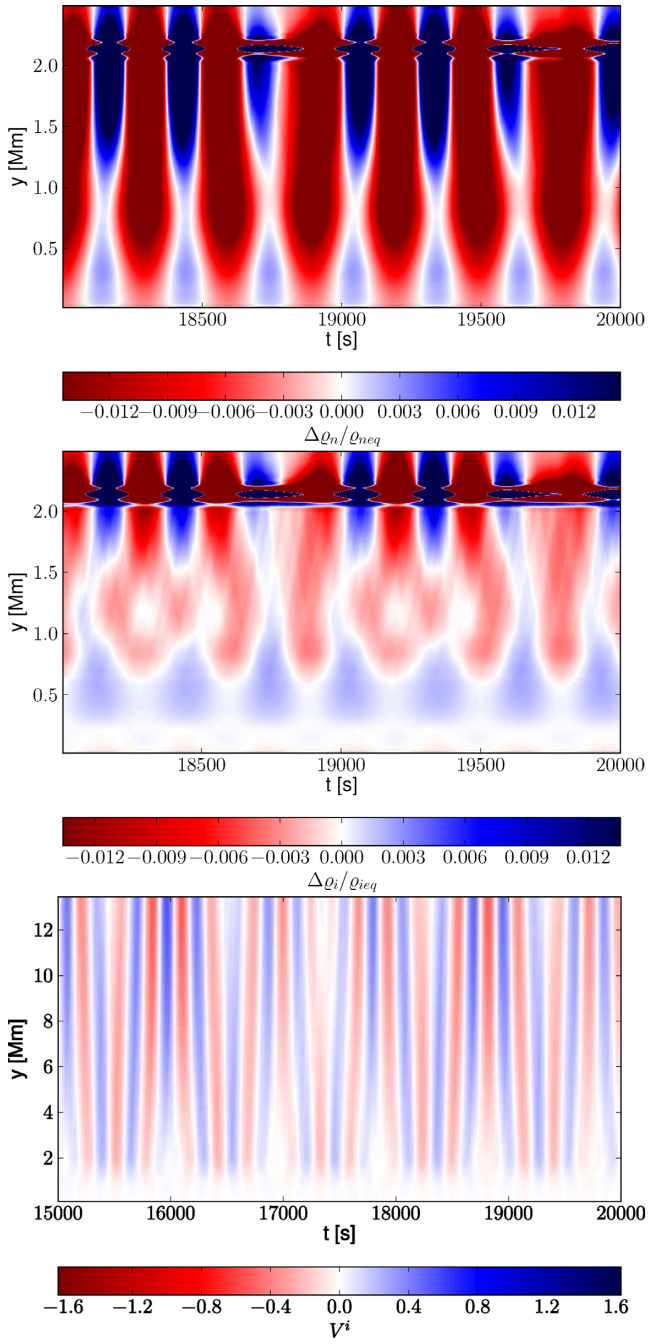

Figure 3. The same as in Fig. 2 but for the driving period $P_d = 300$ s.

process is most pronounced for $P_d > P_{ac}$. Fig. 3 illustrates the case of $P_d = 300$ s. The corresponding waveperiod spectra are displayed on Fig. 5. Note that much energy is transferred to the period of 227 s. The latter fits to a value of $P_{ac}(y = 0)$ and for such value of P acoustic waves propagate into higher atmospheric layers. A similar period was observed for acoustic waves (Fleck & Schmitz 1991) being driven in the isothermal solar atmosphere and for magnetoacoustic waves propagating in the non-isothermal atmosphere (Kraśkiewicz et al. 2018). The difference between the work done here and the cited above is that we can track the evolution of ions and neutrals separately, while Fleck & Schmitz (1991) and Kraśkiewicz et al. (2018) considered a fully ionized plasma.

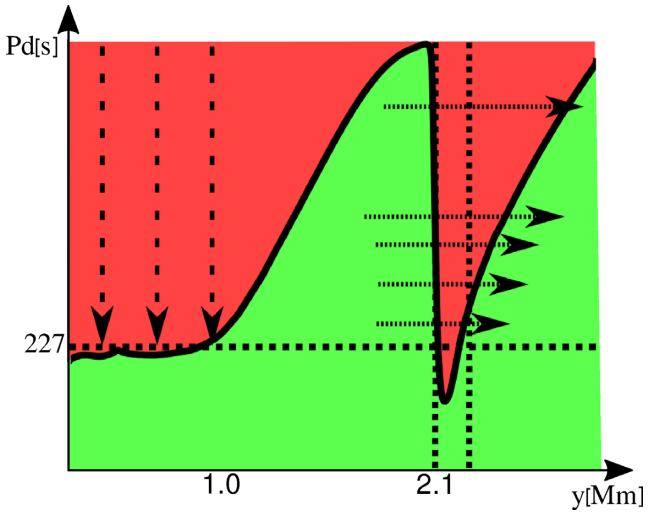

Figure 4. Graphical representation of the obtained results.

Note that in the case of the driving period smaller than the acoustic cut-off in the photosphere, the excited acoustic waves would oscillate with their waveperiod equal to the driving period, and essentially no other waveperiod oscillations are generated (not shown). This is understandable as such driver excites acoustic waves which are propagating throughout all altitudes of the solar atmosphere (e.g. Lamb 1909).

It is clearly visible that oscillations generated in neutral and ionized fluid exhibit different spectra of waveperiods; at a given height y the two-fluid plasma reveals periods which are not that well visible in perturbed mass density of neutrals nor in velocities of ions and neutrals (Fig. 5). In the perturbed mass density of ions the extra generated period of 175 s is dominant in two regions, mainly around $y \approx 0.25$ Mm and within the region of $y = 1.2$–1.55Mm, while it is seen at different heights for the other two studied plasma quantities. Additionally, in the case of ion perturbed mass density, the 227 s period vanishes at the altitudes of $y = 1.5$–1.75Mm, while it is seen only at high altitudes for perturbed neutral mass density and ion velocity. This fact has important observational consequences as essentially only the ionized fluid can be detected.

To verify our results, we ran the code without interaction between ions and neutrals. The obtained results exhibit no extra periods generated beside that one that results from the local cut-off frequency at $y = 0$ for each fluid (not shown).

6 SUMMARY

In this paper, we have performed numerical simulations of ion and neutral acoustic waves, paying particular attention to their evolution with height. These waves are excited by a monochromatic driver of its period P_d, which operates at the bottom of the photosphere. Our findings can be summarized as follows:

(1) The monochromatic driver of its period P_d, lower than the acoustic cut-off period P_{ac} leads to excitation of acoustic waves which propagate freely through the solar atmosphere;

(2) In the case of $P_d > P_{ac}(y = 0)$, the generated acoustic waves transfer to waves of their waveperiod P smaller than P_d and $P = P_{ac}(y = 0) = 227$ s (Fig. 4, downwardly pointing dashed arrows). The waves of $P = 227$ s are propagating through the region of $y > 1$ Mm (green zone) and they tunnel through the transition region, at $y = 2.1$ Mm (Fig. 4, horizontal solid arrows). The oscilla-

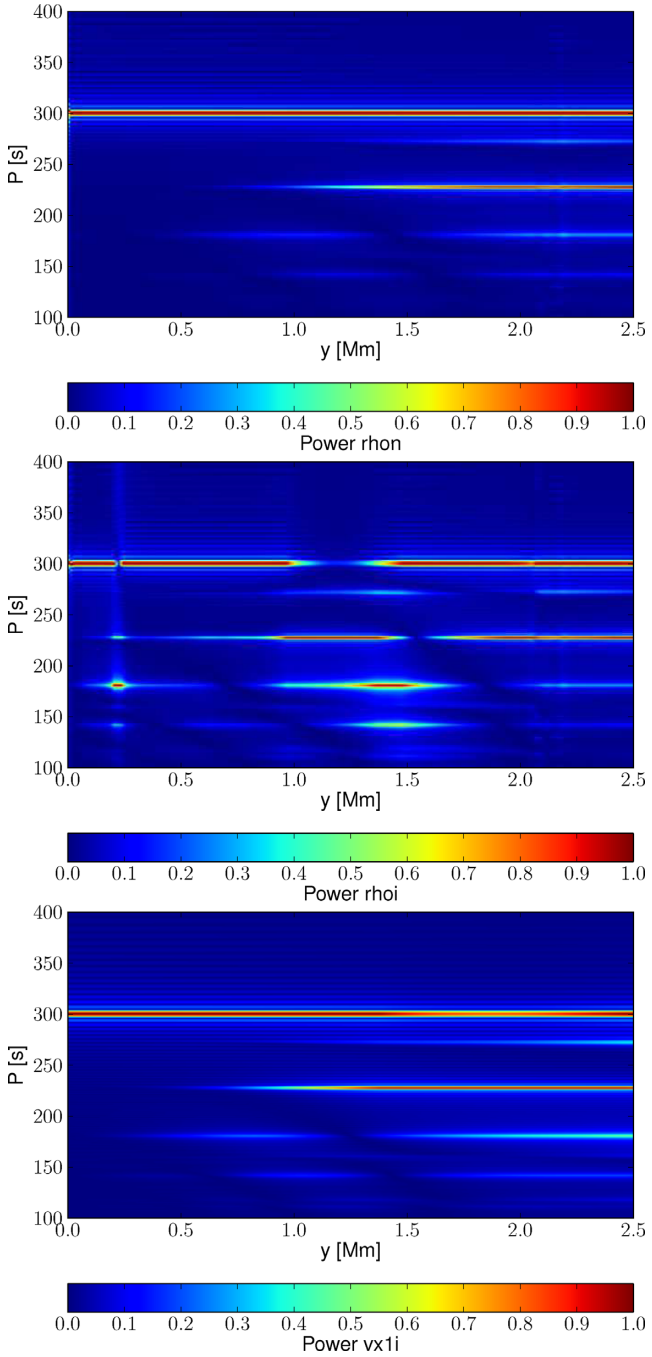

Figure 5. Period versus height calculated from the mass density perturbations of neutrals (top) and ions (middle) as well as the velocity of ions (bottom) in the case of $P_{\rm d} = 300$ s.

tions of 227 s period are visible at different heights both in ions and neutrals velocities and their mass densities in the chromosphere;

(3) The Fourier power spectrum reveals that few extra periods are generated which were also spotted but not discussed in the case of fully ionized plasma (Kraśkiewicz et al. 2018);

(4) Oscillations in mass densities of ions and neutrals differ significantly. In the ion mass density, the two-fluids effects of the system are clearly visible; without the presence of ion–neutral collisions ions and neutrals would oscillate independently and the spectrum of excited waves would be much simpler than in the considered cases.

In conclusion, our findings show that the two-fluid model provides new insights for the propagation of acoustic waves in the solar atmosphere.

ACKNOWLEDGEMENTS

This work was supported by the projects from the National Science Centre (NCN), Poland, Grant nos. 2014/15/B/ST9/00106, 2017/25/B/ST9/00506 and 2017/27/N/ST9/01798. ZEM acknowledges a partial support of this work by the Alexander von Humboldt Foundation.

REFERENCES

Afanasyev A. N., Nakariakov V. M., 2015, A&A, 582, A57
Aschwanden M., 2005, Physics of the Solar Corona, Springer, Berlin Heidelberg
Avrett E. H., Loeser R., 2008, ApJS, 175, 229
Ballester J. L. et al., 2018, Space Sci. Rev., 214, 58
Campos L. M. B. C., 1986, Rev. Mod. Phys., 58, 117
Carlsson M., Stein R. F., 1997, ApJ, 481, 500
Cuntz M., Ulmschneider P., Musielak Z. E., 1998, ApJ, 493, L117
Deubner F. L., Gough D., 1984, ARA&A, 22, 593
Fawzy D. E., Musielak Z. E., 2012, MNRAS, 421, 159
Fawzy D., Rammacher W., Ulmschneider P., Musielak Z. E., Stepień K., 2002, A&A, 386, 971
Fleck B., Schmitz F., 1991, A&A, 250, 235
Fleck B., Schmitz F., 1993, A&A, 273, 671
Gottlieb S., Shu C.-W., 1998, Math. Comput., 67, 73
Khomenko E., Collados M., Díaz A., Vitas N., 2014, Phys. Plasmas, 21, 092901
Kraśkiewicz J., Murawski K., Musielak Z., 2018, A&A, submitted
Kuridze D., Zaqarashvili T. V., Shergelashvili B. M., Poedts S., 2009, A&A, 505, 763
Lamb H., 1909, Proc. R. Soc., s2-7, 122
Lamb H., 1911, Proc. R. Soc., 84, 551
Liu X.-D., Osher S., Chan T., 1994, J. Comput. Phys., 115, 200
Moore D. W., Spiegel E. A., 1964, ApJ, 139, 48
Murawski K., Musielak Z. E., 2016, MNRAS, 463, 4433
Murawski K., Srivastava A. K., Musielak Z. E., Dwivedi B. N., 2015, ApJ, 808, 5
Murawski K., Musielak Z. E., Konkol P., Wiśniewska A., 2016, ApJ, 827, 37
Musielak Z. E., Musielak D. E., Mobashi H., 2006, Phys. Rev. E, 73, 036612
Nakariakov V. M., Verwichte E., 2005, Living Rev. Sol. Phys., 2, 3
Oliver R., Soler R., Terradas J., Zaqarashvili T. V., 2016, ApJ, 818, 128
Priest E., 2009, Magnetohydrodynamics of the Sun, Cambridge University Press, Cambridge
Roberts B., 2006, R. Soc. Trans. Ser., 364 447
Routh S., Musielak Z. E., 2014, Astron. Nachr., 335, 1043
Ulmschneider R., Schmitz F., Kalkofen W., Bohn H. U., 1978, A&A, 70, 487
Vögler A., Shelyag S., Schüssler M., Cattaneo F., Emonet T., Linde T., 2004, A&A, 429, 335
Wiśniewska A., Musielak Z. E., Staiger J., Roth M., 2016, ApJ, 819, L23
Wójcik D., Murawski K., 2018, in preparation
Zaqarashvili T. V., Khodachenko M. L., Rucker H. O., 2011, A&A, 529, A82
Zaqarashvili T. V., Khodachenko M. L., Soler R., 2013, A&A, 549, A113

This paper has been typeset from a TEX/LATEX file prepared by the author.

nature astronomy

LETTERS

https://doi.org/10.1038/s41550-018-0590-1

Confined pseudo-shocks as an energy source for the active solar corona

Abhishek Kumar Srivastava[1]*, Krzysztof Murawski[2], Blażej Kuźma[2], Dariusz Patryk Wójcik[2], Teimuraz V. Zaqarashvili[3,4], Marco Stangalini[5], Zdzislaw E. Musielak[6,7], John Gerard Doyle[8], Pradeep Kayshap[2,9] and Bhola N. Dwivedi[1]

The Sun's active corona requires an energy flux of ~10^3 W m^{-2} to compensate for radiative losses and to maintain its high temperature[1]. Plasma moves in the corona through magnetic loops[2,3], which may be connected with the flows in and around sunspots[4–6]. Global energizing processes (for example, reconnection) play an important part in heating the corona[7–9]; however, energy and mass transport may also occur via shocks, waves or flows[5,10,11]. A full picture and the influence of such localized events, which significantly couple with various layers of the solar upper atmosphere, is still not clear. Using the Interface Region Imaging Spectrograph temporal image data of C II 1,330 Å, we observed the presence of pseudo-shocks around a sunspot. Unlike shocks[12], pseudo-shocks exhibit discontinuities only in the mass density. A two-fluid numerical simulation reproduces such confined pseudo-shocks with rarefied plasma regions lagging behind them. We find that these pseudo-shocks carry an energy of ~10^3 W m^{-2}, which is enough to locally power the inner corona and also generate bulk flows (~10^{-5} kg m^{-2} s^{-1}), contributing to the localized mass transport. If they are ubiquitous, such energized and bulky pseudo-shocks above active regions could provide an important contribution to the heating and mass transport in the overlying solar corona.

Pseudo-shocks were first noticed in supersonic duct flows decelerated to subsonic velocities, and were ascribed to a possible adjustment of the velocity distribution itself[13]. On the Sun, they can be observed in difference maps obtained from high-resolution observations. Here, we analyse the Interface Region Imaging Spectrograph (IRIS) difference maps taken in the line of C II at 1330Å around a sunspot on 8 October 2014 with a spatial resolution of 0.4″ per pixel (where 1″ = 725 km), equivalent to 290 km on the Sun[14]. We obtained a time sequence of running-difference maps at a cadence of 19 s for various observed pseudo-shock sources, covering a period of 2 h (see Figs. 1a,b and 2, and Supplementary Table 1). The running difference maps have been made by taking each particular image and subtracting its previous image in the time sequence. This sunspot is anchored by the diffused loop magnetoplasma threads that extend to the overlying active corona (Fig. 1a). Since these pseudo-shocks are formed locally on the top of the ejected plasma, they are termed confined pseudo-shocks. We detect a number of pseudo-shocks in the present observational baseline (see Supplementary Table 1 and Supplementary Videos 1–8). The pseudo-shocks are visible in the C II 1330Å line but not in the cooler Mg II 2796Å line maps, indicating that they are formed in the transition region/inner corona after the evolution of plasma perturbations somewhere at the top of the chromosphere. The representative context event (tadpole-shaped plasma ejecta) presents the evolution of a pseudo-shock source (Figs. 1b,c and 2), which elongates up to a height of ~5 Mm (Figs. 1c and 2). This bulky and localized feature is evolved at 14:22:08 UT (see top left panel of Fig. 2). The mass within it sweeps towards the head during its evolution to create its bulky head and rarefied tail (Figs. 1c and 2 and Supplementary Video 9).

The velocity of this pseudo-shock in the plane of sky is estimated as ~30 km s^{-1}. This is a lower bound projected value, which may be slightly higher than the sound speed estimated at the C II formation temperature (log[T] = 4.5)[15]. The characteristic reference sound speed at the C II formation temperature is estimated as 26 km s^{-1}. Since the pseudo-shock speed is marginally higher than the characteristic sound speed, this may indicate evolution of a weak shock system. As the pixel size of the IRIS slit-jaw images is 290 km and the cadence of the images is 19 s, the intrinsic motion of the feature in consecutive images is about 2 pixels. This is confirmed in the first two running-difference maps (Fig. 2). The sweeping of mass is evident along the confined magneto-plasma system, which constitutes the pseudo-shock (Figs. 1c and 2). Thereafter, the impulsively evolved pseudo-shock, along with its rarefied tail, further propels upwards before fading in the later part of its total lifetime of ~150 s (Fig. 2). In the present observational baseline, we observe only the evolution of one pseudo-shock. A weak, slow shock with a Mach number (M) slightly greater than one may also be present in the system. However, such weak and faint slow shock may not be evident against the bright and dynamical chromosphere.

We developed a physical model of such localized pseudo-shocks for a weakly diverging, current-free equilibrium magnetic field embedded in a hydrostatic two-fluid atmosphere with an appropriate temperature profile[16–18]. We used a two-fluid (ions: protons and electrons; and neutrals: hydrogen atoms) code, known as the joint analytical and numerical approach (JOANNA), developed by D. Wójcik[16,19] (Fig. 3; see the Methods for details; http://kft.umcs.lublin.pl/dwojcik/) to simulate

[1]Department of Physics, Indian Institute of Technology (BHU), Varanasi, India. [2]Group of Astrophysics, Institute of Physics, UMCS, Lublin, Poland. [3]Space Research Institute, Austrian Academy of Sciences, Graz, Austria. [4]Abastumani Astrophysical Observatory at Ilia State University, Tbilisi, Georgia. [5]INAF-OAR National Institute for Astrophysics, Rome, Italy. [6]Department of Physics, University of Texas at Arlington, Arlington, TX, USA. [7]Kiepenheuer-Institut für Sonnenphysik, Freiburg, Germany. [8]Armagh Observatory and Planetarium, Armagh, UK. [9]Institute of Physics and Biophysics, Faculty of Science, University of South Bohemia, Ceské Budejovice, Czech Republic. *e-mail: asrivastava.app@iitbhu.ac.in

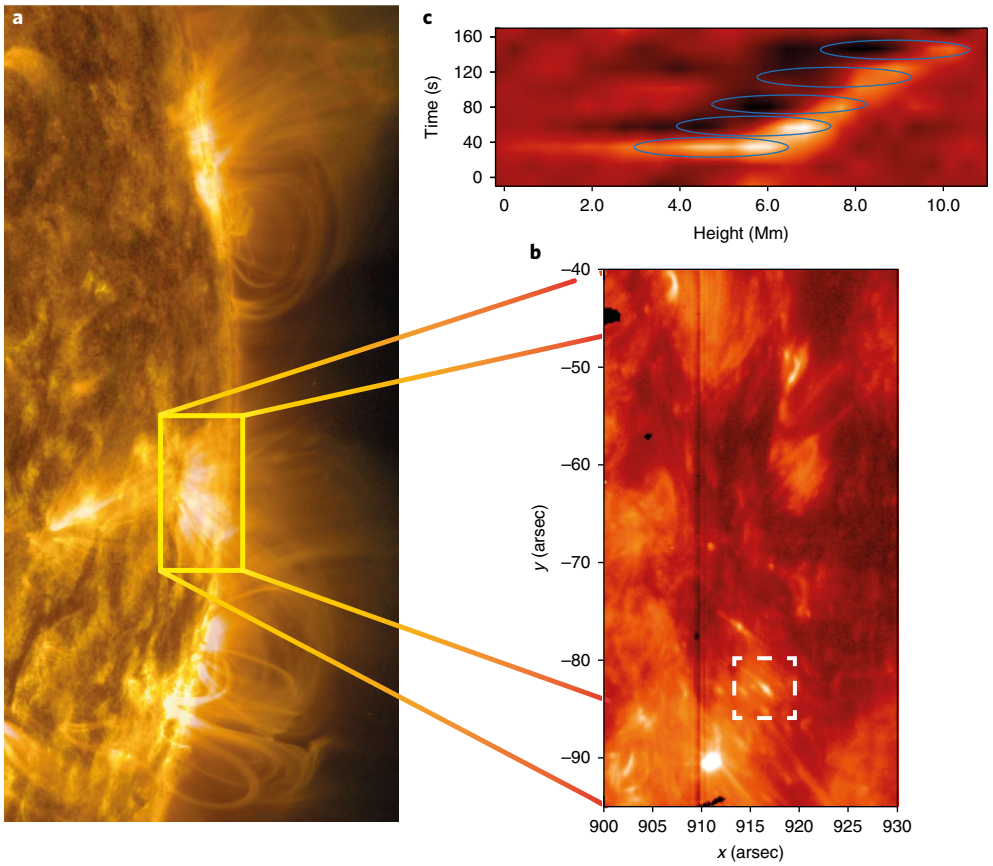

Fig. 1 | Direct imaging of the confined pseudo-shocks around a sunspot. a, Composite image of 171, 304 and 1600Å emissions taken by the Solar Dynamics Observatory/Atmospheric Imaging Assembly, showing diffused loop threads anchored into the sunspot, enabling propulsion of mass and energy to the overlying magnetic domain of the corona through pseudo-shocks that are injected from the lower solar atmosphere at their footpoints. Such pseudo-shock sources are abundant in and around the observed sunspot. **b**, The evolution of a representative pseudo-shock is shown in C II 1,330 Å emission using IRIS slit-jaw imaging on 8 October 2014 at 14:22 UT (Supplementary Table 1 and Supplementary Video 11). **c**, A time–distance map along the representative pseudo-shock (a tadpole-shaped jet) indicated by a white dashed box in **b** exhibits the evolution of its bulky, bright head and rarefied tail as shown within blue ovals.

the observed pseudo-shocks. The hydrostatic plasma equilibrium is perturbed by localized drivers in ion and neutral gas pressure as:

$$[p_i, p_n](x,y,t) = [p_{i0}, p_{n0}]\left(1 + A_{p[i,n]}\ \exp\left(-\frac{(x-x_0)^2}{w^2} - \frac{(y-y_0)^2}{w^2}\right) f(t)\right) \quad (1)$$

$$f(t) = \begin{cases} 1-\exp(-t/\tau), & t \le \tau_{max} \\ \exp(-(t-\tau_{max})/\tau), & t > \tau_{max} \end{cases}$$

Here, x_0 and y_0 are, respectively, the horizontal and vertical position of the drivers, w is their widths, and $A_{p,i}$ and $A_{p,n}$ are their relative amplitudes. The time-dependence of the driver is described by τ (growth/decay time) and τ_{max}, the time at which $f(t)$ reaches a maximum value. We set $w = 0.05$ Mm, $x_0 = 0.7$ Mm, $y_0 = 1.75$ Mm, $A_{p,i} = A_{p,n} = 6$, $\tau = 50$ s and $\tau_{max} = 30$ s. The analytical form of the drivers used here mimics the response of impulsive heating in the localized lower solar atmosphere, which perturbs the gas pressure and generates pseudo-shocks. The perturbations rise with a certain growth rate, while they decay at later times, making their nature episodic and impulsive.

The position of the drivers corresponds to a plasma region of $\beta < 1$, where plasma β is the ratio of gas pressure to the magnetic pressure. The drivers are set at the top of the chromosphere, where the plasma is partially ionized and dominated by a magnetic field over the neutral gas pressure. Therefore, the slow and fast magnetoacoustic waves are weakly coupled there. The drivers essentially excite slow magnetoacoustic waves, which propagate along the magnetic field lines. The waves evolve into a faint and weak slow shock when they cross the solar transition region at $y = 2.1$ Mm, the where density falls rapidly. The plasma behind the shock is swept ahead to create a rarefied tail and a bright and dense pseudo-shock (Fig. 3, middle panel, and Supplementary Video 10) resembling the observations (Figs. 1 and 2, and Supplementary Table 1). The faint, slow shock leaves the domain as a detached leading front ahead of the pseudo-shock. The ongoing magnetic reconnection between penumbral filaments and pre-existing ambient open field lines at the outer periphery of the sunspot may result in such localized perturbations, which move in the overlying stratified atmosphere and create moving shocks/pseudo-shocks (Fig. 1b)[6,20].

The spatiotemporal evolution of the faint slow shock and pseudo-shock (Fig. 4a,c) indicate that the faint slow shock leaves the magnetoplasma domain in the early phase of its evolution, while the pseudo-shock remains associated with it during its total lifespan of ~150 s. Therefore, the energy and mass transport are basically governed by the pseudo-shock source. The energy flux associated

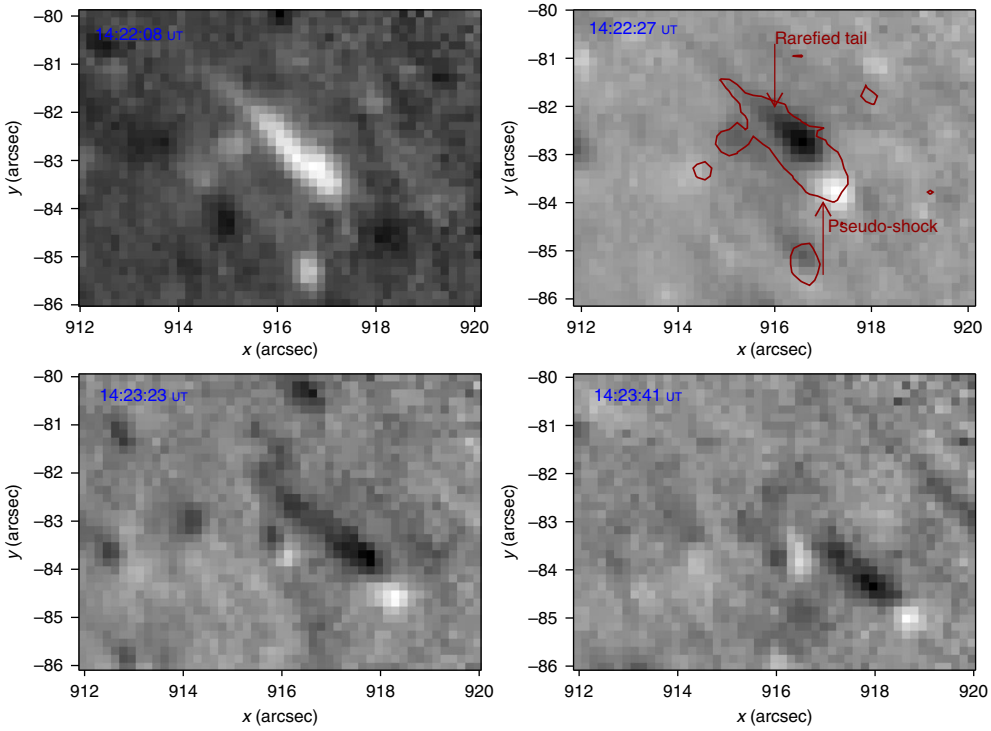

Fig. 2 | Evolution of a pseudo-shock. A running-difference image sequence shows that the plasma is swept along the magnetic field lines, resulting in the formation of a confined pseudo-shock on 8 October 2014 at 14:22 UT. It is elongated up to a height of ~5 Mm and propagates through the solar atmosphere with continuous evolution of rarefied plasma lagging behind. This bright magnetoplasma structure originates impulsively, and an associated pseudo-shock evolves for a finite time. The red contour in the top right image represents the intensity feature of the pseudo-shock when it appeared.

with the pseudo-shock (dashed blue line in Fig. 4a) is greater than the faint, slow shock (dashed red line in Fig. 4a). The pseudo-shock consists of one order of magnitude higher energy (~8×10^3 W m^{-2}) in the upper chromosphere and transition region compared with the slow shock. Therefore, the energy flux of the pseudo-shock is sufficient to energize the lower solar atmosphere locally. Comparison of energy fluxes carried by the pseudo-shock (blue squares in Fig. 4b) and slow shock (red diamonds) exhibits the significance of the pseudo-shock in the inner corona as it carries a substantial amount of energy (~10^3 W m^{-2}) that may be sufficient to compensate for its radiative losses if they dissipate there[1]. Also, the mass flux carried by the pseudo-shock (blue squares in Fig. 4d) is larger than the slow shock front (red diamonds). The value of the mass transport (~10^{-5} kg m^{-2} s^{-1}) due to the pseudo-shocks as computed by the model indicates that the pseudo-shocks may contribute to feeding the plasma into the inner corona above active regions.

Most of the mass and energy fluxes are transported to the transition region and inner corona by neutral particles, while only a fraction of it is due to ions (see Supplementary Text). The transported neutrals impulsively expand in the inner corona and frictional heating may be produced across the pseudo-shock due to strong ion-neutral collisions, which thermalize its kinetic energy to heat the plasma locally[21]. Thus, the pseudo-shock sources may fade gradually after reaching the inner corona, where its energy is dissipated. The study of dissipation of these new energy sources is beyond the scope of this Letter, and will be considered in future study.

This work demonstrates the role of pseudo-shocks in carrying sufficient amounts of energy that may balance the localized coronal losses above solar active regions. These pseudo-shocks are recurrent on the Sun, and present an abundant measure in and around the sunspot (see Supplementary Video 11). Therefore, they may play a crucial role in locally compensating the radiative losses in the overlying corona. We also show that these pseudo-shocks can transport substantial amounts of mass above an active region. However, further studies are required to determine whether they are directly linked to the formation of the slow solar wind[22]. The quiet-Sun heating mechanism has been explored in the form of a variety of competing plasma processes; for example, magnetohydrodynamic waves[23–25] and braiding of magnetic field lines[26], while heating of active regions has typically been associated with nanoflares and reconnection[7]. Pseudo-shocks can potentially provide the required energy and mass transport above solar active regions to balance the coronal losses.

Pseudo-shocks may also be associated with penumbral jets[6], light bridge peacock jets[27] and penumbral dots[28,29], which occur in abundant measures in and around sunspots. These sunspot jets sometimes show the evolution of bright, bulky heads and comparatively rarefied tails, which may suggest the presence of pseudo-shocks within them. If pseudo-shocks evolve in these active-region plasma jets, they may contribute significantly to their energetics and formation. Future observations by the next generation of ultra-high-resolution telescopes (for example, the Daniel K. Inouye Solar Telescope, European Solar Telescope, National Large Solar Telescope, and so on), as well as future theoretical investigations, such as dissipation of these high-energy pseudo-shocks, will be able to constrain the global role of pseudo-shocks in the solar energy budget.

Methods

In this section, we describe the two-fluid equations, initial set-up of the numerical simulation, and solar model atmosphere with realistic temperature and magnetic fields. We have used this two-fluid model and described basic set-up (initial and boundary conditions) to simulate the evolution of pseudo-shocks mimicking the physical properties of the observed pseudo-shocks in the solar chromosphere.

Two-fluid equations. To model the evolution of pseudo-shocks, we consider a gravitationally stratified and magnetically confined plasma made up of two species (that is, ionized (ions + electrons) and neutral fluids). This plasma is governed by a

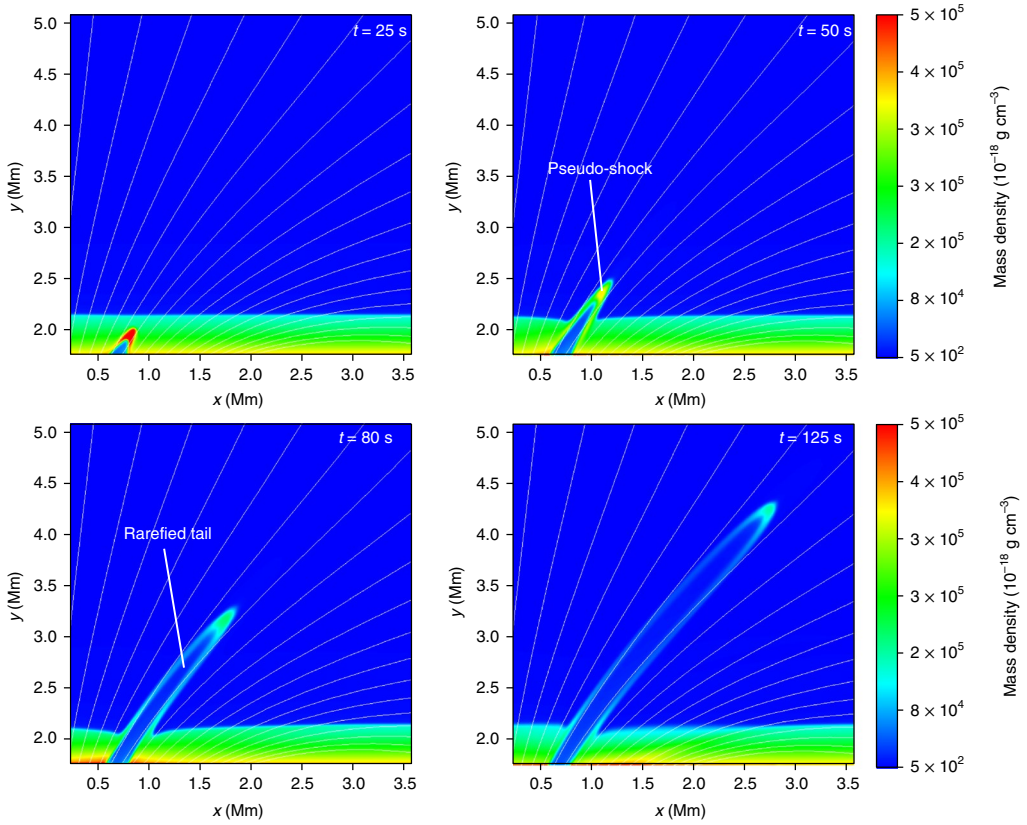

Fig. 3 | Two-fluid simulations of a pseudo-shock using newly developed JOANNA code[15]. The pseudo-shock evolves in the gravitationally stratified and magnetized solar atmosphere. The leading slow shock (weak and invisible), pronounced pseudo-shock (or entropy mode) in the form of a dense and bright contact surface and rarefied tail evolve in the solar atmosphere. Thereafter, they fade and subside gradually. *x* and *y* are the horizontal and vertical spatial extent of the localized model solar atmosphere, respectively.

set of two-fluid equations[19,20]. The resulting equations describing neutral fluids are written as follows:

$$\frac{\partial \varrho_n}{\partial t} + \nabla \cdot (\varrho_n \mathbf{V}_n) = 0 \tag{2}$$

$$\frac{\partial \varrho_n \mathbf{V}_n}{\partial t} + \nabla \cdot (\varrho_n \mathbf{V}_n \mathbf{V}_n + p_n \mathbf{I}) = \alpha_c (\mathbf{V}_i - \mathbf{V}_n) + \varrho_n \mathbf{g} \tag{3}$$

$$\frac{\partial E_n}{\partial t} + \nabla \cdot [(E_n + p_n)\mathbf{V}_n] = \alpha_c \left[\frac{1}{2} |\mathbf{V}_i - \mathbf{V}_n|^2 + \frac{3}{2} \frac{k_B}{m_H} \left(\frac{T_n}{\mu_n} - \frac{T_i}{\mu_i} \right) \right] + \varrho_n \mathbf{g} \cdot \mathbf{V}_n \tag{4}$$

$$E_n = \frac{p_n}{\gamma - 1} + \frac{\varrho_n |\mathbf{V}_n|^2}{2} \tag{5}$$

while ions + electrons are described by:

$$\frac{\partial \varrho_i}{\partial t} + \nabla \cdot (\varrho_i \mathbf{V}_i) = 0 \tag{6}$$

$$\frac{\partial \varrho_i \mathbf{V}_i}{\partial t} + \nabla \cdot (\varrho_i \mathbf{V}_i \mathbf{V}_i + p_i \mathbf{I}) + \mathbf{J} \times \mathbf{B} = -\alpha_c (\mathbf{V}_i - \mathbf{V}_n) + \varrho_i \mathbf{g} \tag{7}$$

$$\frac{\partial \mathbf{B}}{\partial t} - \nabla \times (\mathbf{V}_i \times \mathbf{B}) = 0 \tag{8}$$

$$\nabla \cdot \mathbf{B} = 0 \tag{9}$$

$$\frac{\partial E_i}{\partial t} + \nabla \cdot [(E_i + p_i)\mathbf{V}_i - \mathbf{B}(\mathbf{V} \cdot \mathbf{B})] = \alpha_c \left[\frac{1}{2} |\mathbf{V}_i - \mathbf{V}_n|^2 + \frac{3}{2} \frac{k_B}{m_H} \left(\frac{T_i}{\mu_i} - \frac{T_n}{\mu_n} \right) \right] + \varrho_i \mathbf{g} \cdot \mathbf{V}_i \tag{10}$$

$$E_i = \frac{p_i}{\gamma - 1} + \frac{\varrho_i |\mathbf{V}_i|^2}{2} + \frac{\mathbf{B}^2}{2\mu_0} \tag{11}$$

where $\varrho_{i,n}$, $p_{i,n}$, $\mathbf{V}_{i,n}$, T, $\mathbf{B}$ and α_c are, respectively, the mass density, gas pressure, plasma velocity, plasma temperature, magnetic field and coefficient of collisions between particles. Subscripts *i* and *n* correspond respectively to ions and neutrals, $\mathbf{J} = \nabla \times \mathbf{B}/\mu_0$ is the current density, m_H is the hydrogen mass, k_B is Boltzmann's constant, $\gamma = 5/3$ is an adiabatic index and $\mathbf{g} = (0, -g, 0)$ is the gravitational acceleration. The value of the gravitational acceleration (g) is taken as 274 m s^{-2}. For the sake of simplicity, we limit ourselves to the two-dimensional case with the system being invariant along the *z* direction, and neglect the effect of ionization and recombination (due to the small mass of electrons compared with the ions and neutrals), as well as all electron components.

Numerical simulations using two-fluid equations. To solve the two-fluid equations numerically in the presented simulations, we use JOANNA code[16,19]. We set the Courant–Friedrichs–Lewy (CFL) number equal to 0.3 and specify the simulation box in (x, y) as $(-2.56, 2.56) \times (1.75, 15.0)$ Mm^2, where $y = 0$ denotes the bottom of the photosphere. In the numerical simulations, we adopt the uniform grid within the region $(-2.56 \le x \le 2.56) \times (1.75 \le y \le 6.87)$ Mm^2, which is covered by $1{,}024 \times 1{,}024$ grid points, leading to a resolution of 5 km there. Above this region, we implement a stretched grid of 64 cells along the *y* direction whose size grows with *y*. Such a stretched grid plays the role of a sponge to absorb the incoming signals and it minimizes reflections from the top boundary of the simulation box. We impose open boundary conditions for the outflowing signal at the side boundaries. At the top and bottom of the numerical simulation box, we fix all plasma quantities to their initial equilibrium values, and solve two-fluid equations with the use of a mixed HLLC/HLLD Riemann solver.

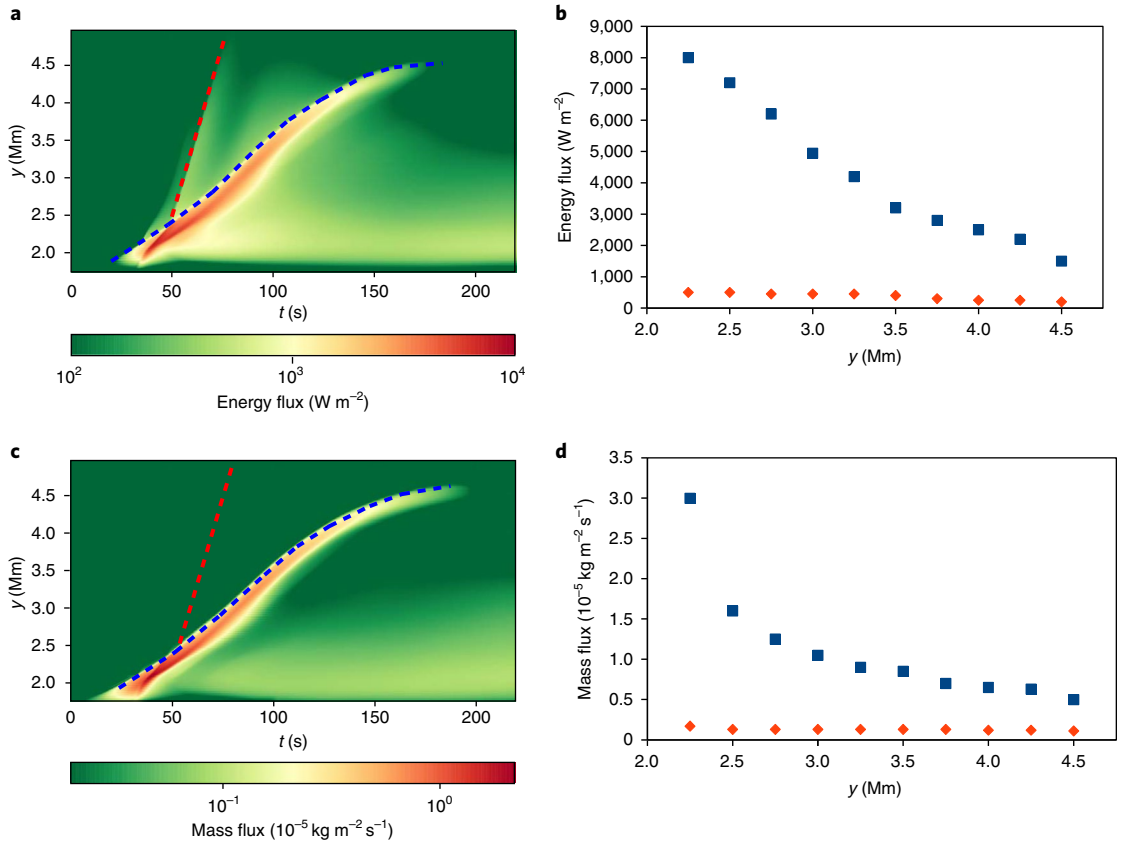

Fig. 4 | Total energy and mass fluxes (for protons + electrons and hydrogen atoms) in a pseudo-shock. a,**c**, Spatiotemporal maps of energy (**a**) and mass fluxes (**c**) are displayed along the moving magnetoplasma system consisting of a faint, slow shock and bright pseudo-shock (Fig. 2). Dashed red and blue curves display the evolution of the slow and pseudo-shock, respectively. **b**,**d**, Comparison of the energy (**b**) and mass fluxes (**d**) carried by the pseudo-shock (blue rectangles) and slow shock (red diamonds) exhibits the significance of the pseudo-shock as it carries high energy (~10^3 W m^{-2}) and mass fluxes (~10^{-5} kg m^{-2} s^{-1}), which may be sufficient to compensate for some part of the radiative (~10^3 W m^{-2}) and mass losses (~10^{-10} kg m^{-2} s^{-1}) in the inner solar corona up to 5.0 Mm height above an active region.

Force-free magnetic field and realistic temperature conditions. The hydrostatic atmosphere for the ions corresponds to a force-free ($\mathbf{J}\times\mathbf{B}=0$) magnetic field with the solenoidal condition ($\nabla\times\mathbf{B}=0$), which is being satisfied. We also assume a current-free ($\mathbf{J}=0$) magnetic field whose horizontal B_x, vertical B_y and transversal B_z components are given as[19]:

$$\begin{aligned} B_x(x,y) &= \frac{-2Sx(y-a)}{(x^2+(y-a)^2)^2} \\ B_y(x,y) &= \frac{S(x^2-(y-a)^2)}{(x^2+(y-a)^2)^2} + B_v \\ B_z(x,y) &= 0 \end{aligned} \tag{12}$$

where B_v is a straight vertical magnetic field component, and a and S are free parameters corresponding to the vertical location of the singularity in the magnetic field and its strength, respectively. We set $B_v=8$ G, $a=-7.5$ Mm and S in such a manner that at the reference point ($x_r=0$, $y_r=6$) Mm, the magnitude of the magnetic field is $B=4$ G. We have examined that the energetics, mass flux and evolution of the pseudo-shocks are almost the same for 1–2 kG magnetic field strength. Therefore, we have taken a 1 kG average magnetic field at the photosphere to prepare our numerical simulations as we notice that these pseudo-shocks are prevalent in the outer part of the sunspot penumbra, as well as nearby regions. The magnetic field lines are displayed in Supplementary Fig. 3.

The realistic temperature profile for ion and neutrals in the solar atmosphere, along with the height, is shown in Supplementary Fig. 4. This temperature is taken from the model[18]. In the photosphere, which is localized at $0\le y\le 0.5$ Mm, $T(y)$ decreases with y until close to the bottom of the chromosphere. Specifically for $y\sim 0.5$ Mm, $T(y)$ reaches a local minimum of about 4.5×10^3 K. Higher up in the atmosphere, $T(y)$ grows with height until the transition region is reached. Thereafter, it rises abruptly to the coronal heights about the values of 1 MK.

Perturbations at the upper chromosphere and generation of pseudo-shocks. We perturb the equilibrium model of the structured solar atmosphere by implementing simultaneously the drivers in ion and neutral gas pressures. These drivers are expressed by equation (1). These drivers are operated at the top of the chromosphere, and as a result slow and fast magnetoacoustic ion waves are weakly coupled there. Therefore, these drivers execute slow magnetoacoustic ion waves, which propagate essentially along the magnetic field lines. As neutrals do not directly feel magnetic field, the drivers generate ion-neutral entropy mode (pseudo-shock) and neutral acoustic waves that propagate quasi-isotropically in the medium. Neutrals are affected there by ion-neutral collisions, which are significant in the low atmospheric region of the Sun. The modelled pseudo-shock resembles the cases observed by IRIS on 8 October 2014, and demonstrates their physical significance.

Data availability

The data that support the plots within this paper and other findings of this study are available from the corresponding author upon reasonable request.

Received: 3 August 2017; Accepted: 5 September 2018;
Published online: 08 October 2018

References

1. Withbroe, G. L. & Noyes, R. W. Mass and energy flow in the solar chromosphere and corona. *Annu. Rev. Astron. Astrophys.* **15**, 363–387 (1977).
2. Feldman, U., Landi, E. & Schwadron, N. A. On the sources of fast and slow solar wind. *J. Geophys. Res.* **110**, A07109 (2005).
3. Harra, L. K. et al. Outflows at the edges of active regions: contribution to solar wind formation? *Astrophys. J.* **676**, L147–L150 (2008).
4. Katsukawa, Y. et al. Small-scale jetlike features in penumbral chromospheres. *Science* **318**, 1594–1597 (2007).

5. Vissers, G. J. M., Rouppe van der Voort, L. H. M. & Carlsson, M. Evidence for a transition region response to penumbral microjets in sunspots. *Astrophys. J.* **811**, 33–38 (2015).
6. Tiwari, S. K., Moore, R. L., Winebarger, A. R. & Alpert, S. E. Transition-region/coronal signatures and magnetic setting of sunspot penumbral jets: Hinode (SOT/FG), Hi-C, and SDO/AIA observations. *Astrophys. J.* **816**, 92 (2016).
7. Cargill, P. J. & Klimchuk, J. A. Nanoflare heating of the corona revisited. *Astrophys. J.* **605**, 911–920 (2004).
8. Aschwanden, M. J., Winebarger, A., Tsiklauri, D. & Peter, H. The coronal heating paradox. *Astrophys. J.* **659**, 1673–1681 (2007).
9. Klimchuk, J. A. Key aspects of coronal heating. *Phil. Trans. R. Soc. A* **373**, 20140256 (2015).
10. Ryutova, M., Berger, T., Frank, Z. & Title, A. On the penumbral jetlike features and chromospheric bow shocks. *Astrophys. J.* **686**, 1404–1419 (2008).
11. Bharti, L., Solanki, S. K. & Hirzberger, J. Lambda-shaped jets from a penumbral intrusion into a sunspot umbra: a possibility for magnetic reconnection. *Astron. Astrophys.* **597**, A127 (2017).
12. Priest, E. R. *Magnetohydrodynamics of the Sun* (Cambridge Univ. Press, Cambridge, 2014).
13. Crocco, L. in *High Speed Aerodynamics and Jet Propulsion: Fundamentals of Gas Dynamics* Vol III (ed. Emmons, H. W.) 110–130 (Princeton Univ. Press, Princeton, 1958).
14. De Pontieu, B. et al. The interface region imaging spectrograph (IRIS). *Sol. Phys.* **289**, 2733–2779 (2014).
15. De Pontieu, B. et al. On the prevalence of small-scale twist in the solar chromosphere and transition region. *Science* **346**, 1255732 (2014).
16. Wójcik, D. P. *Numerical Model of Magnetohydrodynamic Waves in the Solar Atmosphere.* MSc thesis, Maria Curie-Skłodowska Univ. (2016).
17. Konkol, P., Murawski, K. & Zaqarashvili, T. V. Numerical simulations of magnetoacoustic oscillations in a gravitationally stratified solar corona. *Astron. Astrophys.* **537**, A96 (2012).
18. Avrett, E. H. & Loeser, R. Models of the solar chromosphere and transition region from SUMER and HRTS observations: formation of the extreme-ultraviolet spectrum of hydrogen, carbon, and oxygen. *Astrophys. J. Suppl.* **175**, 229–276 (2008).
19. Kuźma, B. et al. 2-fluid numerical simulations of solar spicules. *Astrophys. J.* **849**, 78 (2017).
20. Oliver, R., Soler, R., Terradas, J. & Zaqarashvili, T. V. Dynamics of coronal rain and descending plasma blobs in solar prominences. II. Partially ionized case. *Astrophys. J.* **818**, 128 (2016).
21. Khomenko, E. On the effects of ion-neutral interactions in solar plasmas. *Plasma Phys. Contr. Fusion* **59**, 014038 (2017).
22. Edwards, S. J., Parnell, C. E., Harra, L. K., Culhane, J. L. & Brooks, D. H. A comparison of global magnetic field skeletons and active-region upflows. *Sol. Phys.* **291**, 117–142 (2016).
23. Jess, D. et al. Alfvén waves in the lower solar atmosphere. *Science* **323**, 1582–1585 (2009).
24. McIntosh, S. et al. Alfvénic waves with sufficient energy to power the quiet solar corona and fast solar wind. *Nature* **475**, 477–480 (2011).
25. Srivastava, A. K. et al. High-frequency torsional Alfvén waves as an energy source for coronal heating. *Sci. Rep.* **7**, 43147 (2017).
26. Cirtain, J. W. et al. Energy release in the solar corona from spatially resolved magnetic braids. *Nature* **493**, 501–503 (2013).
27. Yang, S., Zhang, J., Jiang, F. & Xiang, Y. Oscillating light wall above a sunspot light bridge. *Astrophys. J.* **804**, L27 (2015).
28. Tian, H. et al. Observations of subarcsecond bright dots in the transition region above sunspots with the interface region imaging spectrograph. *Astrophys. J.* **790**, L29 (2014).
29. Alpert, S. E., Tiwari, S. K., Moore, R. L., Winebarger, A. R. & Savage, S. L. Hi-C observations of sunspot penumbral bright dots. *Astrophys. J.* **822**, 35 (2016).

Acknowledgements

A.K.S. and B.N.D. acknowledge the RESPOND-ISRO (DOS/PAOGIA205-16/130/602) project. A.K.S. acknowledges the SERB-DST project (YSS/2015/000621) grant, and the Advanced Solar Computational and Analyses Laboratory (ASCAL). Armagh Observatory and Planetarium is grant-aided by the Northern Ireland Department for Communities. J.G.D. acknowledges the DJEI/DES/SFI/HEA Irish Centre for High-End Computing for provision of computing facilities and support. J.G.D. also thanks the STFC for PATT travel and subsistence and the SOLARNET project, which is supported by the European Commission's FP7 Capacities Programme under grant agreement number 312495, for travel and subsistence. M.S. acknowledges support from 'Progetti di ricerca INAF di Rilevante Interesse Nazionale' (PRIN-INAF 2014) and project 2012P2HRCR 'Il sole attivo ed i suoi effetti sul clima dello spazio e della terra' (PRIN MIUR 2012) grants, funded by the Italian National Institute for Astrophysics (INAF) and Ministry of Education, Universities and Research (MIUR), respectively. Work by K.M., B.K. and D.P.W. was supported financially by projects at the National Science Centre, Poland (grant numbers 2014/15/B/ST9/00106 and 2017/25/B/ST9/00506). T.V.Z. was supported by the Austrian Science Fund 'FWF' project P30695-N27 and Georgian Shota Rustaveli National Science Foundation project DI-2016-17. Z.E.M. acknowledges support from the Alexander von Humboldt Foundation. The authors express thanks to A. Kaczmarczyk for assistance with creating the Adobe illustrations. They also acknowledge the use of IRIS and Solar Dynamics Observatory/Atmospheric Imaging Assembly observations in this work.

Author contributions

A.K.S. led the project by defining the novel science case, analysing and making the IRIS observations, and writing the paper. K.M., B.K. and D.P.W. constructed the numerical model based on the two-fluid JOANNA code, which was developed by D.P.W. All co-authors (A.K.S., K.M., B.N.D., J.G.D., T.V.Z., M.S., Z.E.M., B.K., D.P.W. and P.K.) participated in studying the science and editing the draft.

Competing interests

The authors declare no competing interests.

Additional information

Supplementary information is available for this paper at https://doi.org/10.1038/s41550-018-0590-1.

Reprints and permissions information is available at www.nature.com/reprints.

Correspondence and requests for materials should be addressed to A.K.S.

Publisher's note: Springer Nature remains neutral with regard to jurisdictional claims in published maps and institutional affiliations.

Draft version June 4, 2019
Typeset using LaTeX **twocolumn** style in AASTeX62

Two-fluid, numerical simulations of the origin of the fast solar wind

D. Wójcik,[1] B. Kuźma,[1] K. Murawski,[1] and A.K. Srivastava[2]

[1] *Group of Astrophysics, Institute of Physics, University of M. Curie-Skłodowska, ul. Radziszewskiego 10, 20-031 Lublin, Poland*
[2] *Department of Physics, Indian Institute of Technology (Banaras Hindu University), Varanasi-221005, India*

(Received June 4, 2019)

Submitted to ApJ

ABSTRACT

With the use of our JOANNA code, which solves radiative equations for ion + electron and neutral fluids, we perform realistic 2.5D numerical simulations of plasma outflows associated with the solar granulation. These outflows exhibit physical quantities consistent to the order of magnitude with the observational findings for mass and energy losses in the upper chromosphere, transition region and inner corona, and they may originate the fast solar wind.

Keywords: Sun: activity - Sun: corona - Sun: solar wind - magnetohydrodynamics (MHD) - methods: numerical

1. INTRODUCTION

The solar wind is a stream of energized, charged particles, primarily electrons and protons from hydrogen, along with atomic nuclei like helium, alpha particles, flowing outward from the Sun (Parker 1965; Bierman 1951). There is a fast, widely uniform wind, emanating from polar coronal holes and at the distance of 1 AU from the Sun traveling at about 750 km s^{-1}, and a slow, sporadic one, pouring from active equatorial regions and moving with about half smaller speed. The magnetic field lines stretch out radially in coronal holes, and do not loop directly back to the Sun, providing an open path for the fast plasma to escape the gravity grasp. As the corona expands, these winds must be replaced by plasma moving up from below to feed them.

In the modern era of high resolution space-born and ground-based observations, special attention has been paid for studying the origin of plasma outflows which form the solar wind. The early models of the wind assumed the inner corona as its origin (e.g. Tu 1987). Recently, Tu (2005) detected such outflows in coronal funnels at altitudes between 5 Mm and 20 Mm above the photosphere, and found that they reach the speed of up to 10 km s^{-1} at the height of 20 Mm. The emphasis was also given on searching for the outflows in the chromosphere/transition region (e.g. Marsch et al. 2008; McIntosh 2012; Yang et al. 2013; Kayshap et al. 2015). It was found that these outflows can be generated by variety of jets (Wedemeyer-Böhm et al. 2012; Kayshap et al. 2013; Tian et al. 2014; Martínez-Sykora et al. 2017), and injection of often twisted magnetic field and its subsequent reconnection may also contribute to the bulk plasma outflows in coronal holes (e.g. Krieger et al. 1973; Zirker 1977; Yang et al. 2013; Kayshap et al. 2013).

It was showed theoretically that magnetohydrodynamic waves may be responsible for providing the momentum to the upwardly moving plasma (e.g. Ofman 2005; Suzuki & Inutsuka 2005; Srivastava & Dwivedi 2006; Marsch 2006; Arber et al. 2016). Among others, Hollweg (1986), Kudoh & Shibata (1999), Matsumoto & Suzuki (2012) concluded that Alfvén waves possess a potential to drive plasma outflows. He et al. (2008) developed a model of plasma outflows in the coronal funnels, which includes Alfvén waves (Ofman et al. 1995). Along this line of investigation, Yang et al. (2016) found that Alfvén waves are able to form fast plasma outflows. See also Ofman et al. (1995) and Shestov et al. (2017) for a similar analysis. However, Alfvén waves are difficult for

Corresponding author: D. Wójcik
dwojcik@kft.umcs.lublin.pl

detection, particularly when high-frequency waves are concerned (Srivastava et al. 2017); in an inhomogeneous and structured medium, these waves can experience reflection, mode coupling, phase-mixing and resonant absorption (Ofman et al. 1995; Nakariakov et al. 1997; Zaqarashvili & Roberts 2006; Goossens et al. 2012).

Despite the above mentioned achievements, the origin of the solar wind still remains one of the central issues of heliophysics. We investigate here the role of granulation in generation of chromospheric ejecta and associated plasma outflows in coronal holes. We are motivated by the fact that a base of the corona is filled with dynamic jets propelled from below the transition region upwards at speeds of about 25 km s^{-1} into higher layers, and carry a significant amount of momentum (e.g. Sterling 2000; Zaqarashvili & Erdélyi 2009).

This paper is organized as follows. A physical model is presented in Sect. 2 and the corresponding numerical results are shown in Sect. 3. Our paper is concluded by discussion and summary of the numerical results in Sect. 4.

2. TWO-FLUID MODEL OF A PARTIALLY-IONIZED CORONAL HOLE

We consider a solar coronal hole that is magnetically structured and gravitationally stratified, and its dynamics is described by 2-fluid equations for ions + electrons treated as one fluid and neutrals regarded as second fluid. These equations can be written as follows:

$$\frac{\partial \varrho_{\rm n}}{\partial t} + \nabla \cdot (\varrho_{\rm n} \mathbf{V}_{\rm n}) = 0\,, \tag{1}$$

$$\frac{\partial \varrho_{\rm i}}{\partial t} + \nabla \cdot (\varrho_{\rm i} \mathbf{V}_{\rm i}) = 0\,, \tag{2}$$

$$\frac{\partial (\varrho_{\rm n} \mathbf{V}_{\rm n})}{\partial t} + \nabla \cdot (\varrho_{\rm n} \mathbf{V}_{\rm n} \mathbf{V}_{\rm n} + p_{\rm n} \mathbf{I}) = \alpha_c (\mathbf{V}_{\rm i} - \mathbf{V}_{\rm n}) + \varrho_{\rm n} \mathbf{g}\,, \tag{3}$$

$$\frac{\partial (\varrho_{\rm i} \mathbf{V}_{\rm i})}{\partial t} + \nabla \cdot (\varrho_{\rm i} \mathbf{V}_{\rm i} \mathbf{V}_{\rm i} + p_{\rm ie} \mathbf{I}) = \frac{1}{\mu} (\nabla \times \mathbf{B}) \times \mathbf{B} + \alpha_c (\mathbf{V}_{\rm n} - \mathbf{V}_{\rm i}) + \varrho_{\rm i} \mathbf{g}\,, \tag{4}$$

$$\frac{\partial \mathbf{B}}{\partial t} = \nabla \times (\mathbf{V}_{\rm i} \times \mathbf{B})\,, \quad \nabla \cdot \mathbf{B} = 0\,, \tag{5}$$

$$\frac{\partial E_{\rm n}}{\partial t} + \nabla \cdot [(E_{\rm n} + p_{\rm n}) \mathbf{V}_{\rm n}] = \alpha_c \mathbf{V}_{\rm n} (\mathbf{V}_{\rm i} - \mathbf{V}_{\rm n}) + Q_{\rm n}^{\rm in} + q_{\rm n} + \varrho_{\rm n} \mathbf{g} \cdot \mathbf{V}_{\rm n}\,, \tag{6}$$

$$\frac{\partial E_{\rm i}}{\partial t} + \nabla \cdot \left[\left(E_{\rm i} + p_{\rm ie} + \frac{\mathbf{B}^2}{2\mu} \right) \mathbf{V}_{\rm i} - \mathbf{B} (\mathbf{V} \cdot \mathbf{B}) \right] = \alpha_c \mathbf{V}_{\rm i} (\mathbf{V}_{\rm n} - \mathbf{V}_{\rm i}) + Q_{\rm i}^{\rm in} + Q_R^i + q_{\rm i} + \varrho_{\rm i} \mathbf{g} \cdot \mathbf{V}_{\rm i}\,, \tag{7}$$

where the heat production terms are

$$Q_{\rm n}^{\rm in} = \alpha_c (\Delta \tilde{V} + \Delta \tilde{T})\,, \tag{8}$$

$$Q_{\rm i}^{\rm in} = \alpha_c (\Delta \tilde{V} - \Delta \tilde{T}) \tag{9}$$

with

$$\Delta \tilde{V} = \frac{1}{2} |\mathbf{V}_{\rm i} - \mathbf{V}_{\rm n}|^2\,, \tag{10}$$

$$\Delta \tilde{T} = \frac{3 k_{\rm B}}{m_{\rm H} (\mu_{\rm i} + \mu_{\rm n})} (T_{\rm i} - T_{\rm n})\,, \tag{11}$$

and the energy densities are given by

$$E_{\rm n} = \frac{p_{\rm n}}{\gamma - 1} + \frac{\varrho_{\rm n} \mathbf{V}_{\rm n}^2}{2}\,, \tag{12}$$

$$E_{\rm i} = \frac{p_{\rm ie}}{\gamma - 1} + \frac{\varrho_{\rm i} \mathbf{V}_{\rm i}^2}{2} + \frac{\mathbf{B}^2}{2\mu}\,. \tag{13}$$

Here subscripts $_{\rm i}$, $_{\rm n}$ and $_{\rm e}$ correspond to ions, neutrals and electrons, respectively. The symbols $\varrho_{\rm i,n}$ denote mass densities, $\mathbf{V}_{\rm i,n}$ velocities, $p_{\rm ie,n}$ ion+electron and neutral gas pressures, $\mathbf{B}$ is magnetic field and $T_{\rm i,n}$ are temperatures specified by ideal gas laws,

$$p_{\rm n} = \frac{k_{\rm B}}{m_{\rm H} \mu_{\rm n}} \varrho_{\rm n} T_{\rm n}\,, \qquad p_{\rm ie} = \frac{2 k_{\rm B}}{m_{\rm H} \mu_{\rm i}} \varrho_{\rm i} T_{\rm i}\,. \tag{14}$$

A gravity vector is $\mathbf{g} = [0, -g, 0]$ with its magnitude $g = 274.78$ m s^{-2}, $\alpha_{\rm c}$ is the coefficient of collisions between ion and neutral particles (e.g. Oliver et al. 2016; Ballester et al. 2018, and references cited therein), $Q_R^{\rm i}$ radiative losses term which is implemented here in the framework of Abbett & Fisher (2012) in the low atmospheric regions and of thin radiation (Moore & Fung 1972) in the top atmospheric layers, $q_{\rm i,n}$ are thermal conduction terms (Spitzer 1962), $\mu_{\rm i} = 0.29$ and $\mu_{\rm n} = 1.21$ are the mean masses of respectively ions and neutrals, which are taken from the OPAL solar abundance model (e.g. Vögler et al. 2004), $m_{\rm H}$ is the hydrogen mass, $k_{\rm B}$ is the Boltzmann constant, $\gamma = 1.4$ is the specific heats ratio, and μ is magnetic permeability of the medium. The other symbols have their standard meaning.

We consider the case of $z-$invariant system and start our simulations at $t = 0$ s with the hydrostatic equilibrium being supplemented by transversal and vertical magnetic field given as $\mathbf{B} = [B_x, B_y, B_z] = [0, B_0, B_0]$, where $B_0 = 5/\sqrt{2}$ Gs. The transversal component, B_z

results in Alfvén waves being linearly coupled to magnetoacoustic waves. The presence of Alfvén waves is essential in the model, as in the nonlinear regime they are capable of driving vertical flow (e.g. Hollweg 1986; Murawski 1992; Shestov et al. 2017).

In the framework of the implemented magnetic field model we set at $t = 0$ s identical hydrostatic temperature for ions and neutrals, $T_{\rm i}(y) = T_{\rm n}(y) = T(y)$ (Oliver et al. 2016; Martínez-Gómez et al. 2016, 2017; Soler et al. 2017; Srivastava et al. 2018). This temperature is determined by the semi-empirical model of Avrett & Loeser (2008) that is extrapolated into the corona.

The hydrostatic equilibrium is restructured in time by the solar granulation. This granulation appears naturally in the convection zone which is convectively unstable. First signs of granulation are seen already after about 5 min from the start of the simulations with a fully developed state occurring after about 3000 s of the solar time.

3. NUMERICAL SIMULATIONS OF 2-FLUID PLASMA OUTFLOWS

To solve 2-fluid equations numerically, we use JOANNA code (Wójcik et al. 2018). We set in our numerical experiments the Courant-Friedrichs-Lewy number equal to 0.9 and choose a second-order accuracy in space and a four stage, third-order strong stability preserving Runge-Kutta method (Durran 2010) for integration in time, supplemented by adopting the Harten-Lax-van Leer Discontinuities (HLLD) approximate Riemann solver (Miyoshi & Kusano 2005) and Global Lagrange Multiplier (GLM) method of Dedner et al. (2002). The simulation box extends from the convection zone (2.56 Mm below the bottom of the photosphere) to the corona (up to 30 Mm above the photosphere) in $y-$direction and horizontally from $x = -2.56$ Mm to $x = 2.56$ Mm. This box is divided into several patches. The bottom region, specified by -2.56 Mm $\leq y \leq 7.68$ Mm, is covered by the 1024×1024 identical cells, leading to the spatial resolution of 10 km. Within the layer of 7.68 Mm $\leq y \leq 30$ Mm, we implement several patches of progressively larger cells along $y-$direction. At the left- and right- sides of the simulation box we set periodic boundary conditions, while the top and bottom ghost cells are filled by plasma quantities equal to their equilibrium values. The layer for the optical depth greater than 10 is additionally heated by implementing extra source term in the energy equation of ions that balances the energy losses there.

Figure 1 (colormap) shows typical spatial profiles of $\log \varrho_{\rm i}$ (top) and vertical component of ion velocity (bottom). The granulation excites a wide range of waves

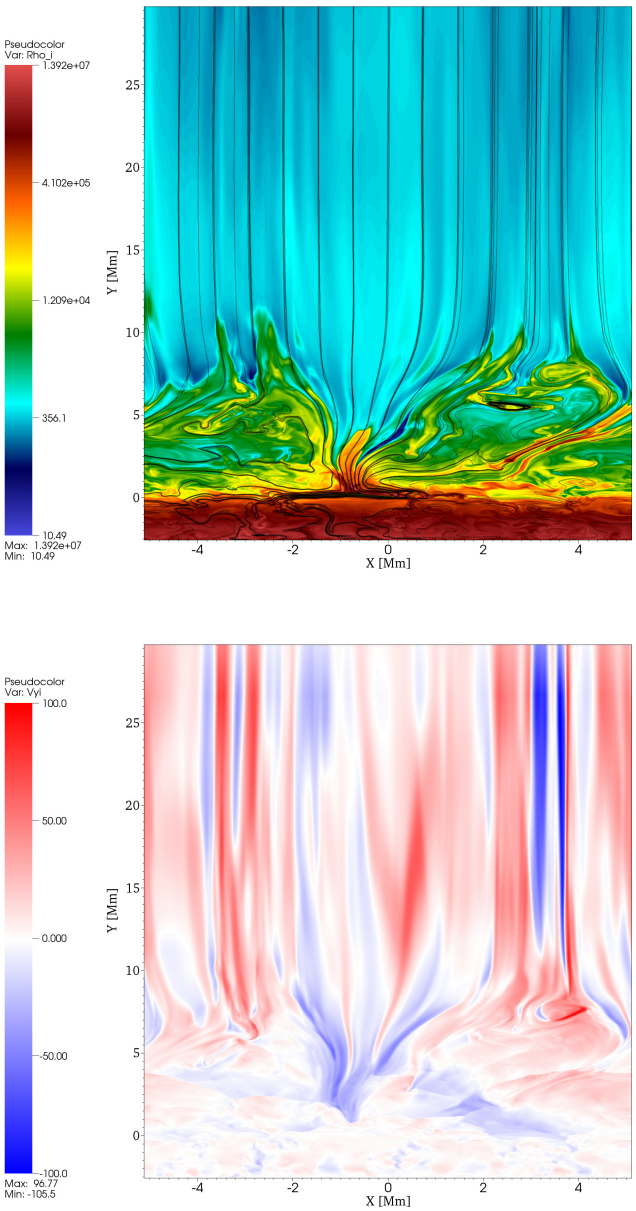

Figure 1. Typical spatial profiles of $\log \varrho_{\rm i}$ overlayed by magnetic field lines (solid lines) (top) and vertical component of velocity $V_{{\rm i}\,y}(x, y)$ (bottom). Ion mass density is given in units of 10^{-18} g cm^{-3} and $V_{{\rm i}\,y}$ is expressed in units of 1 km s^{-1}.

deep in the photosphere. Some of these waves steepen into shocks while propagating upwards. This steepening results from wave amplitude growth with height, and chromospheric jets are excited (top). The plasma above the apices of these jets moves upwards reaching its maximum speed of around 100 km s^{-1} (bottom). The out-

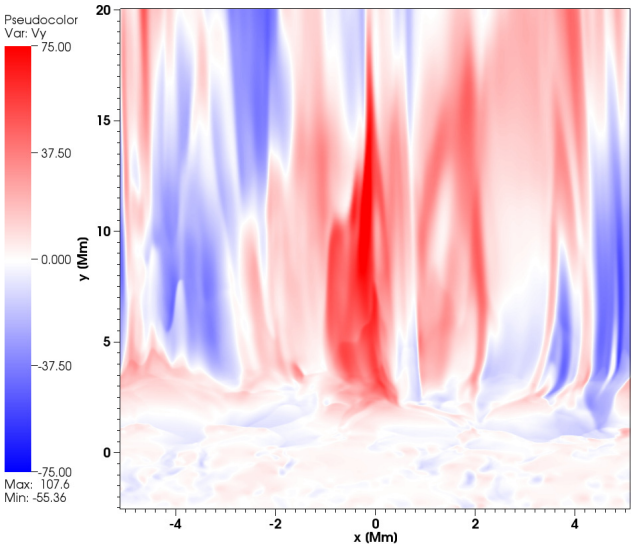

Figure 2. Spatial profile of vertical component $V_{i\,y}(x, y)$, expressed in units of 1 km s^{-1} for the spatial resolution of 20 km x 20 km.

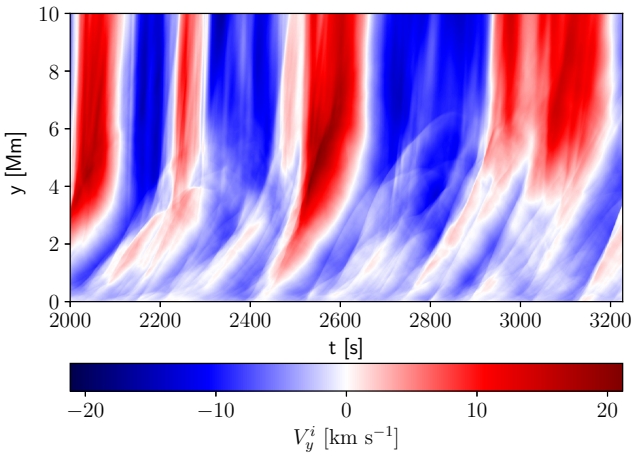

Figure 3. Time-distance plot of horizontally averaged vertical component of ion velocity, $< V_{i\,y}(y, t) >$.

flowing plasma essentially follows open magnetic field lines (black lines) of magnetic funnels that are formed by the granulation. The footpoints of these funnels are rooted deep in the photosphere between granules, while higher up, above the transition region, the magnetic field lines remain essentially vertical. The plasma outflows form strand-like structures along magnetic field lines in the corona, with subsiding plasma taking place at lower altitudes.

We have run the code with extra non-adiabatic terms such as thermal conduction and magnetic diffusion included along with radiation. However, due to the computational effort we have not yet obtained satisfactory results. We have also run the code with the spatial resolution of 20 km x 20 km and the results are showed in Fig. 2. It follows from them that the results are close to these shown in Fig. 1 (bottom), which confirms that the chosen spatial resolution of 10 km x 10 km is sufficient to resolve plasma outflows.

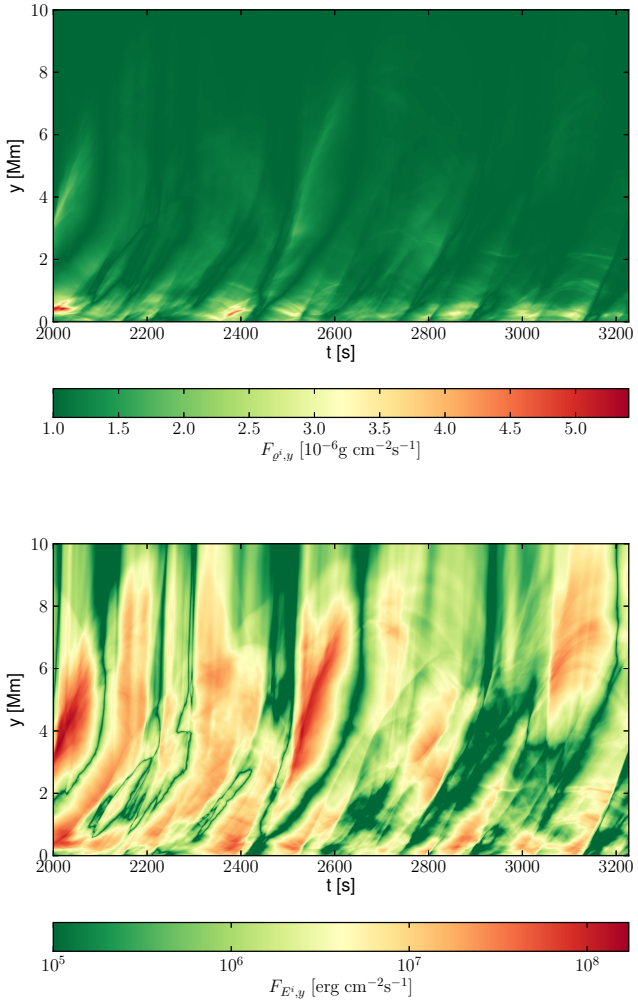

Figure 4. Time-distance plots of the horizontally averaged total vertical mass, $< F_m(y, t) >$, (top) and energy, $< F_E(y, t) >$, (bottom) fluxes.

Figure 3 displays time-distance plot of vertical component of ion velocity that is averaged over the whole horizontal distance, $< V_{i\,y} >$. The plasma jets emerge from the chromospheric background and move into the corona. Some of the injected plasma subsides rapidly after reaching its maximum phase (e.g. Kuźma et al. 2017; Srivastava et al. 2018). This entire process is driven by ongoing granulation in the photosphere. Analyzing the $< V_{i\,y}(y, t) >$ we find that the solar corona experiences

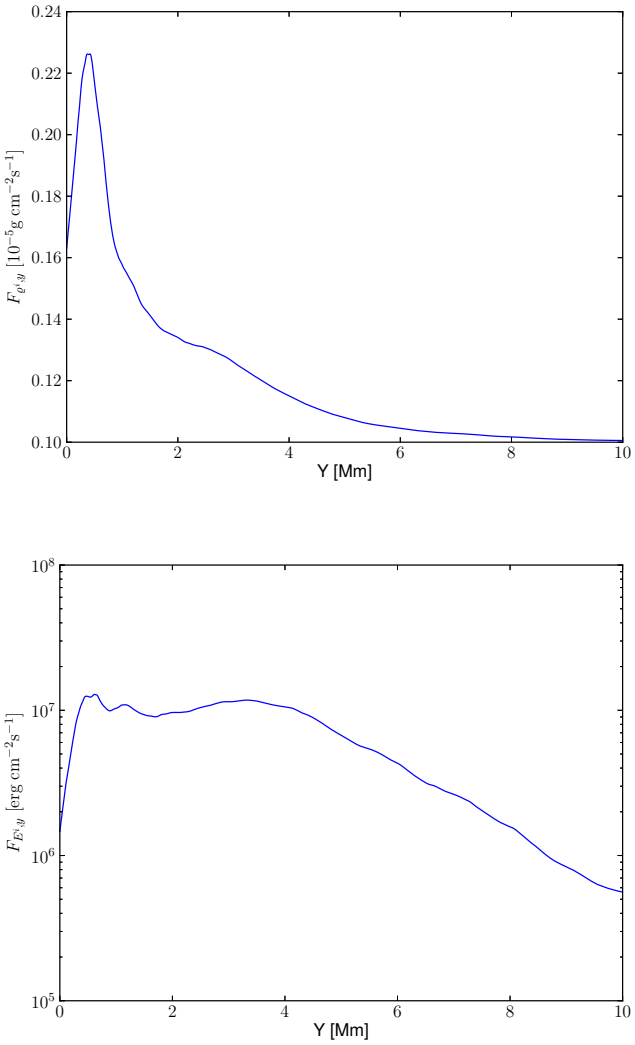

Figure 5. Vertical variation of the temporarily and horizontally averaged mass, $< F_m(y) >$, (top) and energy, $< F_E(y) >$, (bottom) fluxes.

about $1-3$ minute periods oscillations and $< V_{\mathrm{i}\,y} >$ reaches a magnitude of $10-20$ km s^{-1} at $y = 8$ Mm and it grows with height. The physical properties of these outflows are aikin to the flow characteristics reported by Tu (2005).

Figure 4 (top) illustrates time-distance plot of the horizontally averaged total vertical ion mass flux, $F_m(y,t) =< \varrho_{\mathrm{i}} V_{\mathrm{i}\,y} >$, which attains its maximum in the photosphere and lower chromosphere and falls off with height due to rapidly decreasing ion mass density. However, even above the transition region the estimated magnitude of this mass flux lays within the range of 10^{-6} and 10^{-5} g cm^{-2} s^{-1} and it matches the prediction for solar mass losses in the low corona (Withbroe & Noyes 1977).

Vertical component of ion energy flux transported through the medium can be calculated as $F_{\mathrm{E}}(x,y,t) = \varrho_{\mathrm{i}} \mathbf{V}_{\mathrm{i}}^2 V_{\mathrm{iy}}/2$. The time-distance plot of horizontally averaged vertical energy flux, $< F_{\mathrm{E}}(y,t) >$, is shown in Fig. 4 (bottom). We see that plasma escaping into the corona above the transition region carries a significant amount of energy (orange and yellow patches). By comparison with time-distance plots of $< V_{\mathrm{i}\,y} >$ (Fig. 3) we infer that the energy flux associated with the upflowing plasma is higher than for the descending plasma. Note that the obtained values lay within the range of theoretical findings for energy losses in the upper chromosphere, transition region and low corona (Withbroe & Noyes 1977).

Figure 5 shows vertical variation of the temporarily and horizontally averaged mass, $< F_{\mathrm{m}} >$, (top) and energy, $< F_{\mathrm{E}}(y) >$, (bottom) fluxes. Note that $< F_{\mathrm{E}}(y) >$ grows abruptly within the region of $0 < y < 0.5$ Mm, where the dense photospheric plasma experiences a push from the below operating granulation. Higher up, that is for $y > 0.5$ Mm, $< F_{\mathrm{m}}(y) >$ declines with height attaining a value of 10^{-6} g cm^{-2} s^{-1} at $y = 10$ Mm. On the other hand, $< F_{\mathrm{E}}(y) >$ remains close to 10^7 erg cm^{-2} s^{-1} in the entire chromosphere and transition region, attaining its local maxima at $y = 0.25$ Mm and $y = 3.5$ Mm. Higher up, it slowly falls off with height, reaching its value of $5 \cdot 10^5$ erg cm^{-2} s^{-1} at $y = 10$ Mm.

4. DISCUSSION AND SUMMARY

Within the framework of 2-fluid equations for ion-neutral plasma, we performed numerical simulations of the origin of the solar wind which results from plasma outflows. These outflows are associated with jets excited by the solar granulation which develops in the medium with initially straight magnetic field overlaying a hydrostatic equilibrium. This configuration well mimics the expanding open magnetic field region in a polar coronal hole. Our simulations show that this configuration is later on restructured by granulation which operates in the photosphere. The whole scenario is associated with the energy and mass leakage into higher atmospheric layers in the form of plasma outflows. Our results successfully match the expected values of mass and energy losses in the upper chromosphere, transition region and low corona (Withbroe & Noyes 1977).

It is noteworthy here that Tu (2005) obtained a correlation of the Doppler-velocity and radiance maps of spectral lines emitted by various ions (Ne VIII, C IV, Si II) with the force-free magnetic field that was extrapolated from the photospheric magnetogram (SOHO/MDI) in a polar coronal hole. Tu found that Ne VIII ions mostly radiate around the height of 20 Mm above the photo-

sphere, where they reveal the outflow speed of about 10 km s^{-1}, while C IV ions with no average flow speed form essentially around the altitude of 5 Mm. Hence, Tu inferred that the plasma outflows start in the coronal funnels at altitudes in between 5-20 Mm. Yang et al. (2013) proposed that magnetic reconnection, which took place in the open and closed magnetic field region, triggers the plasma outflows observed by Tu (2005). The results of our simulations performed with a novel 2-fluid model of a partially-ionized solar atmospheric plasma confirm these observational findings.

Ten years before the plasma outflows were announced by Tu (2005), there was essentially no report on finely-structured jets. The exceptions were spicules/macrospicules diversely filling the chromosphere and contributing to the mass cycle of the corona (e.g. Tian et al. 2014; Wedemeyer-Böhm et al. 2012). In the limit of current observational resolution, it is established that the overlaying plasma outflows in the corona must be originated due to the contribution from various plasma ejecta. Therefore, without emphasizing on a particular type of a jet, we simulated the solar granulation which resulted in jets and studied their contribution to formation of the solar wind.

In summary, we investigated formation of plasma outflows between 5 to 10 Mm above the photosphere in the open magnetic field region in a coronal hole as observed by Tu (2005). The outflows in such regions consist of continuous streaming of plasma particles from the lower solar atmosphere outward. We point out its linkage to the granulation and associated with them the ubiquitous chromospheric jets which lead to mass and energy leakage into the inner corona. Our model is based on gravitationally stratified and partially-ionized bottom layers of the solar atmosphere with adequate temperature and magnetic field conditions to mimic the ion-neutral plasma outflows. Our studies determine that multiple jets excited by operating in the photosphere granulation are able to stimulate continuous plasma outflows in the solar atmosphere which may result in the fast solar wind at higher altitudes in the solar corona.

The authors express their thanks to Drs. Ramon Oliver, Roberto Soler and David Martinéz-Gómez for their comment on the hydrostatic model of the solar atmosphere. We would like to thank the reviewer for their time and valuable remarks. The JOANNA code has been developed by Darek Wójcik. This work was done within the framework of the projects from the Polish National Foundation (NCN) Grant nos. 2017/25/B/ST9/00506 and 2017/27/N/ST9/01798. Numerical simulations were performed on the LUNAR cluster at Institute of Mathematics of University of M. Curie-Skłodowska, Lublin, Poland.

REFERENCES

Abbett, W. P., & Fisher, G. H. 2012, SoPh, 277, 3, doi: 10.1007/s11207-011-9817-3

Arber, T. D., Brady, C. S., & Shelyag, S. 2016, The Astrophysical Journal, 817, 94, doi: 10.3847/0004-637x/817/2/94

Avrett, E., & Loeser, R. 2008, The Astrophysical Journal Supplement Series, 175, 229, doi: 10.1086/523671

Ballester, J. L., Alexeev, I., Collados, M., et al. 2018, Space Science Reviews, 214, doi: 10.1007/s11214-018-0485-6

Bierman, L. 1951, Zeitschrift für Astrophysik, 29, 274

Dedner, A., Kemm, F., Kröner, D., et al. 2002, Journal of Computational Physics, 175, 645, doi: 10.1006/jcph.2001.6961

Goossens, M., Andries, J., Soler, R., et al. 2012, The Astrophysical Journal, 753, 111, doi: 10.1088/0004-637x/753/2/111

He, J.-S., Tu, C.-Y., & Marsch, E. 2008, Solar Physics, 250, 147, doi: 10.1007/s11207-008-9214-8

Hollweg, J. V. 1986, The Astrophysical Journal, 306, 730, doi: 10.1086/164382

Kayshap, P., Banerjee, D., & Srivastava, A. K. 2015, Solar Physics, 290, 2889, doi: 10.1007/s11207-015-0763-3

Kayshap, P., Srivastava, A. K., Murawski, K., & Tripathi, D. 2013, The Astrophysical Journal, 770, L3, doi: 10.1088/2041-8205/770/1/l3

Krieger, A. S., Timothy, A. F., & Roelof, E. C. 1973, Solar Physics, 29, 505, doi: 10.1007/bf00150828

Kudoh, T., & Shibata, K. 1999, The Astrophysical Journal, 514, 493, doi: 10.1086/306930

Kuźma, B., Murawski, K., Kayshap, P., et al. 2017, ApJ, 849, 78, doi: 10.3847/1538-4357/aa8ea1

Marsch, E. 2006, Living Reviews in Solar Physics, 3, doi: 10.12942/lrsp-2006-1

Marsch, E., Tian, H., Sun, J., Curdt, W., & Wiegelmann, T. 2008, The Astrophysical Journal, 685, 1262, doi: 10.1086/591038

Martínez-Gómez, D., Soler, R., & Terradas, J. 2016, The Astrophysical Journal, 832, 101, doi: 10.3847/0004-637x/832/2/101

—. 2017, The Astrophysical Journal, 837, 80, doi: 10.3847/1538-4357/aa5eab

Martínez-Sykora, J., Pontieu, B. D., Hansteen, V. H., et al. 2017, Science, 356, 1269, doi: 10.1126/science.aah5412
Matsumoto, T., & Suzuki, T. K. 2012, The Astrophysical Journal, 749, 8, doi: 10.1088/0004-637x/749/1/8
McIntosh, S. W. 2012, Space Science Reviews, 172, 69, doi: 10.1007/s11214-012-9889-x
Miyoshi, T., & Kusano, K. 2005, Journal of Computational Physics, 208, 315, doi: 10.1016/j.jcp.2005.02.017
Moore, R. L., & Fung, P. C. W. 1972, SoPh, 23, 78, doi: 10.1007/BF00153893
Murawski, K. 1992, Solar Physics, 139, 279, doi: 10.1007/bf00159155
Nakariakov, V. M., Roberts, B., & Murawski, K. 1997, Solar Physics, 175, 93, doi: 10.1023/a:1004965725929
Ofman, L. 2005, Space Science Reviews, 120, 67, doi: 10.1007/s11214-005-5098-1
Ofman, L., Davila, J. M., & Steinolfson, R. S. 1995, The Astrophysical Journal, 444, 471, doi: 10.1086/175621
Oliver, R., Soler, R., Terradas, J., & Zaqarashvili, T. V. 2016, The Astrophysical Journal, 818, 128, doi: 10.3847/0004-637x/818/2/128
Parker, E. 1965, Space Science Reviews, 4, doi: 10.1007/bf00216273
Shestov, S. V., Nakariakov, V. M., Ulyanov, A. S., Reva, A. A., & Kuzin, S. V. 2017, The Astrophysical Journal, 840, 64, doi: 10.3847/1538-4357/aa6c65
Soler, R., Terradas, J., Oliver, R., & Ballester, J. L. 2017, The Astrophysical Journal, 840, 20, doi: 10.3847/1538-4357/aa6d7f
Spitzer, L. 1962, Physics of Fully Ionized Gases
Srivastava, A. K., & Dwivedi, B. N. 2006, Journal of Astrophysics and Astronomy, 27, 353, doi: 10.1007/bf02702541
Srivastava, A. K., Shetye, J., Murawski, K., et al. 2017, Scientific Reports, 7, doi: 10.1038/srep43147
Srivastava, A. K., Murawski, K., Kuźma, B., et al. 2018, Nature Astronomy, doi: 10.1038/s41550-018-0590-1
Sterling, A. C. 2000, Solar Physics, 196, 79, doi: 10.1023/a:1005213923962
Suzuki, T. K., & Inutsuka, S. 2005, The Astrophysical Journal, 632, L49, doi: 10.1086/497536
Tian, H., Li, G., Reeves, K. K., et al. 2014, The Astrophysical Journal, 797, L14, doi: 10.1088/2041-8205/797/2/l14
Tu, C.-Y. 1987, Solar Physics, 109, 149, doi: 10.1007/bf00167405
—. 2005, Science, 308, 519, doi: 10.1126/science.1109447
Vögler, A., Shelyag, S., Schüssler, M., et al. 2004, Astronomy & Astrophysics, 429, 335, doi: 10.1051/0004-6361:20041507
Wedemeyer-Böhm, S., Scullion, E., Steiner, O., et al. 2012, Nature, 486, 505, doi: 10.1038/nature11202
Withbroe, G. L., & Noyes, R. W. 1977, Annual Review of Astronomy and Astrophysics, 15, 363, doi: 10.1146/annurev.aa.15.090177.002051
Wójcik, D., Murawski, K., & Musielak, Z. E. 2018, MNRAS, 481, 262, doi: 10.1093/mnras/sty2306
Yang, L., He, J., Peter, H., et al. 2013, The Astrophysical Journal, 777, 16, doi: 10.1088/0004-637x/777/1/16
Yang, L., Lee, L. C., Chao, J. K., et al. 2016, The Astrophysical Journal, 817, 178, doi: 10.3847/0004-637x/817/2/178
Zaqarashvili, T. V., & Erdélyi, R. 2009, Space Science Reviews, 149, 355, doi: 10.1007/s11214-009-9549-y
Zaqarashvili, T. V., & Roberts, B. 2006, Astronomy & Astrophysics, 452, 1053, doi: 10.1051/0004-6361:20053565
Zirker, J. B. 1977, Reviews of Geophysics, 15, 257, doi: 10.1029/rg015i003p00257
Durran, D. R. 2010, Springer New York, doi: 10.1007/978-1-4419-6412-0

Bibliografia

[1] W. P. Abbett and G. H. Fisher. Radiative cooling in MHD models of the quiet sun convection zone and corona. *Solar Physics*, 277(1):3–20, July 2011.

[2] J. L. Ballester, I. Alexeev, M. Collados, T. Downes, R. F. Pfaff, H. Gilbert, M. Khodachenko, E. Khomenko, I. F. Shaikhislamov, R. Soler, E. Vázquez-Semadeni, and T. Zaqarashvili. Partially ionized plasmas in astrophysics. *Space Science Reviews*, 214(2), mar 2018.

[3] A. Dedner, F. Kemm, D. Kröner, C.-D. Munz, T. Schnitzer, and M. Wesenberg. Hyperbolic divergence cleaning for the MHD equations. *Journal of Computational Physics*, 175(2):645–673, jan 2002.

[4] B. T. Draine. Multicomponent, reacting MHD flows. *Monthly Notices of the Royal Astronomical Society*, 220(1):133–148, may 1986.

[5] J. A. Eddy. A new sun: The solar results from skylab. *George C. Marshall Space Flight Center*, 1979.

[6] B. Fryxell, K. Olson, P. Ricker, F. X. Timmes, M. Zingale, D. Q. Lamb, P. MacNeice, R. Rosner, J. W. Truran, and H. Tufo. FLASH: An adaptive mesh hydrodynamics code for modeling astrophysical thermonuclear flashes. *The Astrophysical Journal Supplement Series*, 131(1):273–334, Nov. 2000.

[7] B. Kuźma, K. Murawski, P. Kayshap, D. Wójcik, A. K. Srivastava, and B. N. Dwivedi. Two-fluid numerical simulations of solar spicules. *The Astrophysical Journal*, 849(2):78, Nov. 2017.

[8] J. E. Leake, C. R. DeVore, J. P. Thayer, A. G. Burns, G. Crowley, H. R. Gilbert, J. D. Huba, J. Krall, M. G. Linton, V. S. Lukin, and W. Wang. Ionized plasma and neutral gas coupling in the sun's chromosphere and earth's ionosphere/thermosphere. *Space Science Reviews*, 184(1-4):107–172, oct 2014.

[9] P. S. Li, A. Myers, and C. F. McKee. AMBIPOLAR DIFFUSION HEATING IN TURBULENT SYSTEMS. *The Astrophysical Journal*, 760(1):33, oct 2012.

[10] B. C. Low. Three-dimensional structures of magnetostatic atmospheres. i - theory. *The Astrophysical Journal*, 293:31, June 1985.

[11] E. T. Meier and U. Shumlak. A general nonlinear fluid model for reacting plasma-neutral mixtures. *Physics of Plasmas*, 19(7):072508, jul 2012.

[12] A. Mignone, G. Bodo, S. Massaglia, T. Matsakos, O. Tesileanu, C. Zanni, and A. Ferrari. PLUTO: A numerical code for computational astrophysics. *The Astrophysical Journal Supplement Series*, 170(1):228–242, may 2007.

[13] L. Ofman. MHD waves and heating in coronal holes. *Space Science Reviews*, 120(1-2):67–94, Sept. 2005.

[14] R. Oliver, R. Soler, J. Terradas, and T. V. Zaqarashvili. Dynamics of coronal rain and descending plasma blobs in solar prominences. ii. partially ionized case. *The Astrophysical Journal*, 818(2):128, 2016.

[15] E. Parker. Dynamical theory of the solar wind. *Space Science Reviews*, 4(5-6), Sept. 1965.

[16] E. R. Priest. *Solar Magnetohydrodynamics*. Springer Netherlands, 1982.

[17] P. D. Smith and J. I. Sakai. Chromospheric magnetic reconnection: two-fluid simulations of coalescing current loops. *Astronomy & Astrophysics*, 486(2):569–575, May 2008.

[18] A. K. Srivastava and B. N. Dwivedi. Magnetosonic waveguide model of solar wind flow tubes. *Journal of Astrophysics and Astronomy*, 27(2-3):353–359, June 2006.

[19] A. K. Srivastava, K. Murawski, B. Kuźma, D. P. Wójcik, T. V. Zaqarashvili, M. Stangalini, Z. E. Musielak, J. G. Doyle, P. Kayshap, and B. N. Dwivedi. Confined pseudo-shocks as an energy source for the active solar corona. *Nature Astronomy*, 2(12):951–956, Oct. 2018.

[20] A. K. Srivastava, J. Shetye, K. Murawski, J. G. Doyle, M. Stangalini, E. Scullion, T. Ray, D. P. Wójcik, and B. N. Dwivedi. High-frequency torsional alfvén waves as an energy source for coronal heating. *Scientific Reports*, 7(1), mar 2017.

[21] T. K. Suzuki and S. ichiro Inutsuka. Making the corona and the fast solar wind: A self-consistent simulation for the low-frequency alfvén waves from the photosphere to 0.3 AU. *The Astrophysical Journal*, 632(1):L49–L52, Sept. 2005.

[22] C.-Y. Tu. A solar wind model with the power spectrum of alfvénic fluctuations. *Solar Physics*, 109(1):149–186, Feb. 1987.

[23] C.-Y. Tu. Solar wind origin in coronal funnels. *Science*, 308(5721):519–523, Apr. 2005.

[24] A. A. Vlasov. THE VIBRATIONAL PROPERTIES OF AN ELECTRON GAS. *Soviet Physics Uspekhi*, 10(6):721–733, June 1968.

[25] D. Wójcik, B. Kuźma, K. Murawski, and A. K. Srivastava. Two-fluid, realistic numerical simulations of the origin of the fast solar wind. *The Astrophysical Journal - przyjęty do druku*, 2019.

[26] D. Wójcik, K. Murawski, and Z. E. Musielak. Acoustic waves in two-fluid solar atmosphere model: cutoff periods, chromospheric cavity and wave tunneling. *Monthly Notices of the Royal Astronomical Society*, aug 2018.

[27] D. Wójcik, K. Murawski, Z. E. Musielak, P. Konkol, and A. Mignone. Numerical simulations of torsional alfvén waves in axisymmetric solar magnetic flux tubes. *Solar Physics*, 292(2), Jan. 2017.

[28] M. V. Zombeck. *Handbook of Space Astronomy and Astrophysics*. Cambridge University Press, 2006.